

**The $^{26}\text{Al}(p,\gamma)^{27}\text{Si}$ Reaction:
Stellar Origins of Galactic ^{26}Al**

Thesis by
Robert Bruce Vogelaar

In Partial Fulfillment of the Requirements
for the Degree of
Doctor of Philosophy

California Institute of Technology
Pasadena, California
1989

(Submitted April 4, 1989)

Acknowledgements

This work has relied on the encouragement, guidance, and generosity of many people. Dr. Jim Thomas introduced me to both this project and to Prof. Ralph Kavanagh, who had already requested the ^{26}Al sample from LANL which Dr. Hal O'Brien generously loaned to us. Dr. Leon Mitchell had inspirational motivation which was crucial in the early stages. The collaboration with Dr. Art Champagne at Princeton was both enjoyable and fruitful. The RBS facilities of the Electrical Engineering department were made available to us through Dr. David Jamieson, who took an active interest in our progress. His fitting and graphics program, NUFIT, was used to generate most of the figures. Through the entirety of this project, my advisor, Prof. Ralph Kavanagh, has given me tremendous support and encouragement. His vast experience, and active interest in stellar nucleosynthesis, guided my explorations into this field.

I would like to thank also several individuals who have contributed their time and resources: Will Schick, for his swift and precise machining; Bob Carr, for helping to improve the accelerator's performance; Al Massey, for patiently fixing my electronics; Pat Huber, for giving me system privileges; Kimberley Thomas, for her advice in chemistry; Prof. Dick Azuma, for the deuterium depleted hydrogen; and Drs. Steve Kellogg and T. R. Wang, for enjoyable collaborations and discussions.

While living in Pasadena, several people have welcomed me into their homes. I would like to thank the Merchants, Kavanaghs, Weavers, and others for their hospitality. Many friendships were also developed, in particular with Dave James and Dawn Meredith. Most important, though, was my meeting Nancy, who had the courage and love to marry me. Her commitment to our mutual welfare and intellectual honesty has been vital to the completion of this work.

This thesis is dedicated to my parents, who have
always encouraged and supported my academic pursuits.

Abstract

To explain the ^{26}Mg isotopic anomaly seen in meteorites (^{26}Al daughter) as well as the observation of 1809-keV γ rays in the interstellar medium (live decay of ^{26}Al) one must know, among other things, the destruction rate of ^{26}Al . Properties of states in ^{27}Si just above the $^{26}\text{Al} + p$ mass were investigated to determine the destruction rate of ^{26}Al via the $^{26}\text{Al}(p, \gamma)^{27}\text{Si}$ reaction at astrophysical temperatures.

Twenty micrograms of ^{26}Al were used to produce two types of Al_2O_3 targets by evaporation of the oxide. One was onto a thick platinum backing suitable for (p, γ) work, and the other onto a thin carbon foil for the $(^3\text{He}, d)$ reaction.

The $^{26}\text{Al}(p, \gamma)^{27}\text{Si}$ excitation function, obtained using a germanium detector and voltage-ramped target, confirmed known resonances and revealed new ones at 770, 847, 876, 917, and 928 keV. Possible resonances below the lowest observed one at $E_p = 286$ keV were investigated using the $^{26}\text{Al}(^3\text{He}, d)^{27}\text{Si}$ proton-transfer reaction. States in ^{27}Si corresponding to 196- and 286-keV proton resonances were observed. A possible resonance at 130 keV (postulated in prior work) was shown to have a strength of $\omega\gamma < 0.02 \mu\text{eV}$.

By arranging four large NaI detector as a 4π calorimeter, the 196-keV proton resonance, and one at 247 keV, were observed directly, having $\omega\gamma = 55 \pm 9$ and $10 \pm 5 \mu\text{eV}$, respectively.

Large uncertainties in the reaction rate have been reduced. At novae temperatures, the rate is about 100 times faster than that used in recent model calculations, casting some doubt on novae production of galactic ^{26}Al .

Contents

Acknowledgements	ii
Dedication	iii
Abstract	iv
Contents	v
List of Figures	vii
List of Tables	ix
1. Introduction	1
1.1 meteorite chronology	1
1.2 γ -ray astronomy	3
1.3 stellar production sites	4
1.4 reaction rate in a stellar environment	6
1.5 $^{26}\text{Al}(p, \gamma)^{27}\text{Si}$	9
1.6 previous direct measurements	10
1.7 previous indirect measurements	11
1.8 scope of current work	13
2. Target Production	25
2.1 preparation of sample	25
2.2 molecular plating (targets 1–4)	26
2.3 evaporation of oxide (targets 5–6)	28
2.4 transmission target (targets 7–9)	30
3. $^{26}\text{Al}(p, \gamma)$ with a Germanium Detector	42
3.1 target considerations	42
3.2 experimental setup	43
3.3 excitation function	45
4. $^{26}\text{Al}(^3\text{He}, d)$ using a Q-3D Spectrometer	67
4.1 target considerations	68
4.2 experimental setup	68
4.3 analysis	69
5. $^{26}\text{Al}(p, \gamma)$ with a NaI Detector	82
5.1 experimental setup	82

5.2 preliminary runs	84
5.3 efficiency	85
5.4 data runs	85
5.5 analysis	86
5.6 resonance strengths	89
6. Conclusions and Future Directions	103
6.1 comparison to statistical-model calculation	103
6.2 consequences for specific production sites	104
6.3 destruction timescales	106
6.4 galactic distributions	107
6.5 general constraints and other reactions	109
6.6 summary	110
Appendix	120
References	150

List of Figures

1.1 Isotope Correlation in the Allende Meteorite	14
1.2 HEAO3 Detection of the 1809 keV γ -ray Line	15
1.3 SMM Detection of the 1809 keV γ -ray Line	16
1.4 The Mg-Al Cycle	17
1.5 Example Stellar Reaction Rates	18
1.6 The Proton Destruction Rate of ^{26}Al	19
1.7 Energy Levels in ^{27}Si	20
1.8 States in ^{27}Si near the $^{26}\text{Al} + \text{p}$ Mass	21
1.9 Coulomb-Barrier Penetration for $^{26}\text{Al} + \text{p}$	23
2.1 Molecular Plating Equipment	32
2.2 Evaporation Equipment	32
2.3 Foil Evaporation Equipment	32
2.4 Profiles of Test ^{27}Al Targets	33
2.5 Changes in Target Profiles after Bombardment	34
2.6 Surface Profile of ^{26}Al Target #6	36
2.7 Transmission Target Production	37
2.8 Rutherford Backscattering on Target #8	39
3.1 Germanium Detector Geometry	51
3.2 HPGe Efficiency	52
3.3 Typical Germanium Spectrum	53
3.4 Target Deterioration	55
3.5 Background Excitation Function	56
3.6 2164-keV Excitation Function	58
3.7 New Resonances	60
3.8 Branching Ratios	63
4.1 Princeton AVF Cyclotron Facility	73
4.2 Particle Identification	74
4.3 Deuteron Spectrum at $\theta_{lab} = 5^\circ$	75
4.4 Subtraction and Fitting Analysis	76
4.5 Kinematic Identification	78
4.6 Angular Distributions and DWBA Fits	79
5.1 NaI Detector Geometry	90
5.2 Front-End Electronics	92

5.3 Separating Reactions by E_x	93
5.4 Detector Efficiency	94
5.5 196-keV Resonance	96
5.6 Efficiency Curves for ^{26}Al Resonances	98
5.7 Delayed $^{27}\text{Si}(\beta^+)^{27}\text{Al}$ Decay	99
5.8 γ rays from the 7653-keV State in ^{27}Si	100
5.9 Determining Branching Ratios for the 7653-keV State	101
5.10 247-keV Resonance	102
6.1 $N_A\langle\sigma v\rangle$ for $^{26}\text{Al}(p, \gamma)^{27}\text{Si}$	111
6.2 Dominant Destruction Mechanisms	113
6.3 Mean Life of ^{26}Al	114
6.4 Galactic Distribution of 1809-keV γ -rays (BAL87)	115
6.5 Model Distributions	116
6.6 Comparison to Other Important Rates	117
A.1 Pulse-Height Spectra at Each Resonance	124
A.2 γ -ray Yields at Each Resonance	137

List of Tables

1.1 Previously Known $^{26}\text{Al}(p, \gamma)^{27}\text{Si}$ Resonances	24
2.1 Analyzed Impurities in the ^{26}Al Solution from LANL	40
2.2 Initial Properties of ^{26}Al Targets	41
3.1 Observed Elemental Composition of ^{26}Al Target #6	66
4.1 DWBA Parameters	81
4.2 DWBA Fits	81
6.1 $^{26}\text{Al}(p, \gamma)^{27}\text{Si}$ Resonance Parameters	118

CHAPTER 1

Introduction

Curiosity about the origin of the elements and their evolution into the material we observe today sired the field of nuclear astrophysics. As a result, a qualitative understanding of stellar nucleosynthesis has evolved, wherein primordial hydrogen and helium are converted through nuclear reactions into heavier elements in the interiors of stars. The stellar models which have been developed provide a framework for taking measured nuclear cross sections and making quantitative predictions of isotope abundances and distributions. Conversely, these models can use observed abundance and distribution data to determine which reaction rates are important. Frequently though, the combination of measured rates and field observations forces the revision of a stellar model in order to maintain a self-consistent picture.

The story behind the discovery of ^{26}Al , through its daughter ^{26}Mg in the Al-lende meteorite and the observation of its 1809-keV decay radiation in the interstellar medium (ISM), demonstrates this interplay between experiment, theory, and observation.

1.1: meteorite chronology

The composition of many meteorites indicates that the parent asteroids underwent intense heating within the first $10^6 - 10^8$ years of the solar system (whose age is about 4.6 Ga), reaching temperatures of about 2000 °C. Radioactivity is the most likely heat source (URE55, FIS60), since gravitational energy is insufficient and chemical heating occurs mainly on the surface as the asteroid collects new material. Such surface heat would quickly radiate away.

The size of parent asteroids is also limited. Those less than a few kilometers in radius conduct internal heat too quickly to the surface, where it radiates away, while asteroids larger than a few hundred kilometers could not have cooled enough

since the collapse of the solar nebula to explain their argon retention from the decay of ^{40}K .

Using these size constraints, one finds that, of the possible radioisotopes, those with lifetimes greater than about 10^8 years deposit energy too slowly, while those with lifetimes less than about 10^5 years require an unacceptably quick condensation of newly synthesized material. The energy yield of the remaining candidates was then deduced from estimates of their abundance and decay energy, leaving ^{26}Al as the most likely candidate with $t_{1/2} = 7.2 \times 10^5$ years, and $Q_{\text{EC}} = 4.0$ MeV.

If ^{26}Al were the heat source, some meteorite inclusions could have solidified before all the ^{26}Al decayed. If these inclusions also had a sufficiently high Al/Mg ratio (≈ 10), an increase in the $^{26}\text{Mg}/^{24}\text{Mg}$ ratio correlating with the amount of ^{27}Al present might be observable. Although the extensive heating and recycling during meteoritic evolution—perhaps due to the ^{26}Al itself—would tend to erase this signature, the strength of these arguments resulted in many searches.

The first striking correlation was seen in an inclusion of the Allende meteorite; the results of this study by Lee, Papanastassiou and Wasserburg (LEE77) are indicated in Figure 1.1. They concluded that an initial $^{26}\text{Al}/^{27}\text{Al}$ ratio of $(5.1 \pm 0.6) \times 10^{-5}$ must have existed and argued that *in situ* decay had occurred. (However, there were also some Al-rich inclusions having an initial $^{26}\text{Al}/^{27}\text{Al}$ ratio of less than 2×10^{-7} (LEE79).)

Although excess ^{26}Mg had been observed, conclusions about the role of its parent ^{26}Al in asteroid heating remain disputed. Despite evidence presented by Lee et al. (LEE77) favoring a molten history for the Allende inclusion, Clayton, in a review article (CLA87), maintains that “The known ^{26}Mg excesses are found in small Al-rich inclusions within unequilibrated and microscopically heterogeneous meteorites that were never hot.” Clayton has even suggested geochemical processes as alternatives to *in situ* decay for explaining the observed ^{26}Mg -Al correlation (CLA75, CLA84).

1.2: γ -ray astronomy

Meanwhile, ^{26}Al had become a key element on another front. Astronomers had been trying to observe current nucleosynthesis by detecting live radioactivities which, without constant replenishment, should have decayed away. Discovery of atomic lines from the unstable element Tc on the surface of some stars by Merrill (MER56) was the first direct evidence of this nature. In 1965 Clayton and Craddock predicted that γ -ray emissions following β decay of some nuclei should also be observable in the ISM (CLA65, 69, 73, 74) and the subsequent discovery of the 511-keV annihilation line (JOH72) *might* be attributable to such sources. Supernovae calculations (RAM77, ARN77, WOO80) predicted that ^{26}Al , ^{60}Fe and ^{22}Na should have a sufficient equilibrium abundance in the ISM to permit detection of the γ rays emitted following their decay. The shorter-lived activities, which are produced in much larger quantities by supernovae, typically decay to undetectable levels before the ejecta diffuse enough to allow their decay radiation to escape.

While looking for these lines with the *HEAO3* satellite, Mahoney et al. discovered the first unique γ line from the ISM (MAH82, MAH84). Results of their *HEAO3* experiment are presented in Figure 1.2, showing a residual peak at 1809 keV after background subtraction. The detected flux of $(4.8 \pm 1.0) \times 10^{-4} \text{ cm}^{-2}\text{s}^{-1}\text{rad}^{-1}$ is attributed to $\approx 3 M_{\odot}$ of ^{26}Al , assuming a source distribution similar to that of high-energy galactic γ rays ($\geq 70 \text{ MeV}$) which is believed to reflect the distribution of supernovae in the galaxy. This observation prompted re-analysis of accumulated data from the *Solar Maximum Mission* (SMM). Each time the galactic center had passed through the detector's field of view there was an increased yield in a broad window about 1809 keV indicating a 10σ detection (SHA85). The results, presented in Figure 1.3, correspond to a flux of $(4.0 \pm 0.4) \times 10^{-4} \text{ cm}^{-2}\text{s}^{-1}\text{rad}^{-1}$ and suggest a narrower source distribution than assumed in the *HEAO3* work. There have been two subsequent detections, using balloon experiments (BAL87, MAC87). One of these

(BAL87), finds a distribution consistent with a point source at the galactic center. The actual distribution should prove useful in ultimately determining the stellar origin of ^{26}Al , as will be discussed later.

1.3: stellar production sites

Having verified recent production of ^{26}Al , we are led to ponder its source, especially because the constraints imposed by its short half-life might reveal some interesting stellar dynamics. The major burning stages in stellar evolution bypass ^{26}Al , requiring operation of the so-called p and/or rp processes for substantial ^{26}Al production. In addition, the large $^{26}\text{Al}(n,p)^{26}\text{Mg}$ and $^{26}\text{Al}(n,\alpha)^{23}\text{Na}$ rates which destroy ^{26}Al suggest a neutron-free environment. A possible “Mg-Al cycle” operating in a hydrogen-rich region, is presented in Figure 1.4. Four stellar hosts providing this environment have been considered: supernovae, novae, red giants, and Wolf-Rayet stars.

Prior to observation of the 1809-keV radiation, theoretical calculations involving supernovae as a source were investigated with great enthusiasm (ARN78, TRU78, WOO80). Using Hauser-Feshbach calculations for many of the unknown nuclear-reaction rates, supernova models having peak temperatures of a few billion degrees ($T_9 \sim \text{few}$) could give an $^{26}\text{Al}/^{27}\text{Al}$ ratio of $(0.4 \rightarrow 2.0) \times 10^{-3}$. Such yields could account for the isotope effects seen in Allende, if there were no dilution and less than four million years passed between production and incorporation into the inclusions. Such short timescales had led Cameron and Truran, among others, to postulate a supernova trigger for the formation of the solar system (CAM77). The proximity of such a recent event kindled the imagination of many, and helped satisfy our innate curiosity about earth’s origins.

Subsequent discovery of the 1809-keV radiation in the galaxy implies an *equilibrium* $^{26}\text{Al}/^{27}\text{Al}$ ratio of about 10^{-5} , exceeding by about a factor of 50 that which can be accounted for by supernova production (CLA87). However, this equilibrium

amount is insufficient to explain the Allende findings on its own. Clayton postulated that a supernova event *could* explain all the observations if it occurred 10^5 years ago and 10 pc away in the direction of the galactic center (CLA84), but the probability of such an occurrence seems low enough to discount it. Another problem with supernova production is the absence of an 1157-keV γ -ray line following the decay of ^{44}Ti whose averaged intensity is expected to be 15 times that of the 1809-keV line (CLA87).

Calculations of explosive hydrogen burning in novae ($T_9 \approx .05 - 0.5$) give an $^{26}\text{Al}/^{27}\text{Al}$ ratio between 0.1 and 5 (ARN80, WAR80, HIL82, WAL81). Assuming a rate of about 40 novae per year in our galaxy with $10^{-4} M_\odot$ ejected per event, Clayton estimated an equilibrium $1.2 M_\odot$ of ^{26}Al could be maintained this way (CLA84). More recent calculations by Wiescher et al. (WIE86), using updated reaction rates, indicate only about $0.2 M_\odot$ could be maintained in the galaxy.

Nørgaard (NOR80) considered ^{26}Al production in thermally pulsing red giants. At the bottom of the convective hydrogen envelope an $^{26}\text{Al}/^{27}\text{Al}$ ratio of 0.5 to 1 could be obtained at temperatures of $T_9 \approx 0.07 - 0.09$. Nørgaard argued that due to mass loss, these red giants *might* have contributed to the ^{26}Al anomalies seen in the Allende meteorite. Truran has subsequently investigated red giants as possible sources for the equilibrium amount of ^{26}Al seen in our galaxy. However, the dynamics of convection and dredge-up are not at all certain and the applicable nuclear rates even less so.

Wolf-Rayet (WR) stars are another candidate for ^{26}Al production. These massive stars ($\approx 100 M_\odot$), having prodigious stellar winds, were suggested as possible sources of ^{26}Al by Dearborn and Blake (DEA85), and the idea was subsequently pursued by Prantzos and Cassé (PRA86). The ^{26}Al production zones typically had $T_9 \leq 0.07$. Prantzos and Cassé found that, integrated over the WR star's lifetime of $(3 - 5) \times 10^5$ years, a $50 M_\odot$ star could eject $2.2 \times 10^{-5} M_\odot$ of ^{26}Al , while a

100 M_{\odot} star could eject $13 \times 10^{-5} M_{\odot}$. Whether this can account for the observed amount depends on the frequency and distribution of such stars, parameters still largely unknown. Various plausible assumptions found in (PRA86) can give from 0.2 to 2.2 M_{\odot} of ^{26}Al .

The predicted yields of ^{26}Al from any of the above sources typically have a common difficulty: the lack of an estimated uncertainty. At lower temperatures several key reaction rates are still unknown by orders of magnitude and could substantially alter the above arguments.

At peak temperatures used in supernova calculations ($T_9 \approx 3$), statistical models for the reaction rates are usually reliable due to the large number of states involved. However, at the lower temperature sites, experimental knowledge of the reaction rates becomes crucial. Fortunately, as the temperature decreases, so does the number of rates involved, since nuclear-burning timescales become long compared to β^+ decay. This effectively eliminates the need to know many of the rates involving unstable targets.

1.4: reaction rate in a stellar environment

In an astrophysical environment having energies characterized by a Maxwell-Boltzmann distribution, the nuclear reaction rate is given by

$$\langle \sigma v \rangle = \left(\frac{8}{\pi \mu} \right)^{1/2} \frac{1}{(kT)^{3/2}} \int_0^{\infty} \sigma(E) E \exp\left(-\frac{E}{kT}\right) dE.$$

Reactions between nuclei involved in the Mg-Al cycle can be characterized as compound-nuclear processes, with cross sections dominated by narrow resonances having a Breit-Wigner form

$$\sigma(E) = \pi \lambda^2 \frac{2J + 1}{(2J_1 + 1)(2J_2 + 1)} \frac{\Gamma_a \Gamma_b}{(E - E_R)^2 + (\Gamma/2)^2},$$

where Γ_a , Γ_b , and Γ refer to the partial channel widths and the total width, respectively. The compound level has spin J , while J_1 and J_2 refer to incident particle and target spin. For isolated resonances with $\Gamma \ll E_R$, one thus obtains

$$\langle \sigma v \rangle = \left(\frac{2\pi}{\mu kT} \right)^{3/2} \hbar^2 \omega \gamma \exp \left(-\frac{E_R}{kT} \right),$$

where

$$\omega = \frac{2J + 1}{(2J_1 + 1)(2J_2 + 1)}$$

$$\gamma = \frac{\Gamma_a \Gamma_b}{\Gamma},$$

and in specific units

$$\langle \sigma v \rangle = 2.557 \times 10^{-19} \frac{\omega \gamma}{(\mu_A T_9)^{3/2}} \exp \left(-11.605 \frac{E_R}{T_9} \right) \text{ cm}^3 \text{ s}^{-1}.$$

Here T_9 is the temperature in billions of degrees, E_R the center-of-mass resonance energy in MeV, $\omega \gamma$ the so-called "resonance strength" in eV, and μ_A the reduced mass in atomic-mass units. If resonances are several widths apart, one can simply add their contributions to get the total reaction rate.

Interactions of protons with nuclei in the Ne-Na and Mg-Al cycles (except for ^{23}Na and ^{27}Al) are limited to (p, γ) and (p, p') at the temperatures encountered. Thus $\Gamma = \Gamma_p + \Gamma_{p'} + \Gamma_\gamma$, with Γ_γ typically being a few eV, independent of resonance energy. However, Γ_p depends on the Coulomb-barrier penetrability and is given by

$$\Gamma_p(E, l) = \left(\frac{3\hbar^2}{2\mu r^2} \right) 2kr P_l(E) \theta^2 = \left(\frac{2E}{\mu} \right)^{1/2} \frac{3\hbar}{r} P_l(E) \theta^2,$$

where

$$P_l(E) = \frac{1}{(F_l^2 + G_l^2)}; \quad \theta^2 \leq 1,$$

or in specific units

$$\Gamma_p(E, l) = 27.46 \left(\frac{E}{\mu_A} \right)^{1/2} \frac{P_l(E) \theta_l^2}{R} \quad \text{MeV}.$$

The channel radius R is in fermis, and F_l and G_l are the regular and irregular Coulomb functions. (Here l is the relative angular momentum, although we will

frequently refer to it as the “proton l -transfer,” l_p .) The dimensionless reduced proton width is given by θ^2 . The Wigner limit is obtained by setting $\theta^2 = 1$. For an $l = 0$ proton, the partial widths in the $^{26}\text{Al}(p, \gamma)^{27}\text{Si}$ reaction become comparable when $E_R \approx 0.3$ MeV. Below this energy γ quickly approaches Γ_p while at higher energies, γ approaches Γ_γ .

Figure 1.5 shows the resulting reaction rate for $l = 0$ resonances having the full Wigner strength at low energies and $\omega\gamma = 1$ eV above $E_R = 0.3$ MeV. Clearly, at low temperatures, the exact location and strength of individual resonances dramatically affects the reaction rate. However, as the temperature rises, the Maxwell-Boltzmann distribution broadens, spreading its weight over a larger energy range, including the denser, higher-energy resonances. This reduces an individual level’s contribution, enabling statistical models, such as the Hauser-Feshbach formalism, to be employed—which predict cross sections using average level densities. At lower energies such models could not be used for an additional reason: the steep Coulomb penetration factor requires specific knowledge of level energies to determine the cross section.

There is no clear temperature above which Hauser-Feshbach calculations are reliable. The required high level density frequently depends on the reaction addressed. For example, an $l = 0$ proton having an intrinsic spin of $\frac{1}{2}$ impinging on ^{26}Al with a ground-state spin of 5 can populate either a $\frac{9}{2}$ or $\frac{11}{2}$ state in ^{27}Si with $E_x \geq 7.5$ MeV. Overall level spacing at this excitation range is about 40 keV, but states with suitable spin may have five times this spacing. In general, experimentally determined reaction rates in the Mg-Al region can begin to seriously disagree with model calculations below about $T_9 = 0.5$.

One should also realize from Figure 1.5 that an experiment which measures an excitation function between E_1 and E_2 can *only* provide a *lower* limit on $\langle\sigma v\rangle$, applicable from $T_9 = 0 \rightarrow \infty$.

Since many proposed sites of ^{26}Al production operate at low temperatures, all the low-lying resonances need to be identified. Direct measurements are usually limited by dwindling yield at the lower energies corresponding to astrophysically interesting temperatures. For example, the possible $E_p = 97$ keV resonance in $^{26}\text{Al}(p, \gamma)^{27}\text{Si}$ suggested by Wang et al. (WAN89), assuming $l = 0$ and $\theta^2 = 1$, would give only 100 reactions per Coulomb of proton bombardment of a pure ^{26}Al target.

Fortunately, the locations of low-lying resonances can often be identified by using transfer reactions to examine the level structure of the final nucleus. The properties of these states can then be used to estimate the corresponding (p, γ) strength. This work employed both methods, though the direct approach proved more fruitful due to target limitations.

1.5: $^{26}\text{Al}(p, \gamma)^{27}\text{Si}$

We have discussed the significance of ^{26}Al in meteoritic chronology, and its subsequent observation as fossil ^{26}Mg ; decay lines indicating current nucleosynthesis, and the 1809-keV γ -ray detection; possible ^{26}Al production sites, and the difficulties involved in determining the relevant reaction rates. We now narrow our focus to the $^{26}\text{Al}(p, \gamma)^{27}\text{Si}$ reaction rate and the context in which it arises.

The “Mg-Al cycle” has been mentioned as a possible hydrogen-burning scenario giving rise to ^{26}Al . If the cycle were closed, with no new material flowing in, and $\tau_{\text{cycle}} \ll \tau_{\text{burn}}$, the equilibrium $^{26}\text{Al}/^{27}\text{Al}$ ratio would be determined completely by reactions within the cycle. However, recent measurements (TIM88, CHA88) of the $^{27}\text{Al}(p, \alpha)^{24}\text{Mg}$ rate reveal it to be substantially less than the leakage reaction $^{27}\text{Al}(p, \gamma)^{28}\text{Si}$ for temperatures above $T_9 = 0.05$, contrary to Hauser-Feshbach predictions. This means that the simplifying assumptions above are grossly in error, and meaningful results must include a full network calculation, taking into account feeding, leakage, and stellar dynamics. Nevertheless, to identify the nuclei involved, we will continue to refer to the “cycle.”

At low temperatures the short half-lives of ^{25}Al and ^{27}Si lead to a truncated reaction network, with five nuclei playing dominant roles. (These nuclei are shaded in Figure 1.4.) Note that for $T_9 \geq 0.4$ the 5^+ ground state of ^{26}Al comes into thermal equilibrium with the 228-keV 0^+ isomeric state which has a 6.3-second half-life (WAR80). At lower temperatures, one must keep track of them separately with implications discussed in Chapter 6. We are interested in the final ground-state production because of its 7.2×10^5 -year half-life.

Four of these key nuclei are stable, and the availability of suitable targets has allowed substantial progress to be made in determining their reaction rates. Recently, ^{26}Al production via $^{25}\text{Mg}(p, \gamma)^{26}\text{Al}_0$ was addressed by Champagne et al. (CHA86). Direct studies on ^{26}Al however, required a man-made isotope.

To date, the ^{26}Al proton destruction rate has been measured directly by Buchmann et al. (BUC84) and indirectly (via transfer reactions) by Schmalbrock et al. (SCH86), and Wang et al. (WAN89). However, large uncertainties still remaining in the reaction rate, coupled with the availability of ^{26}Al at Los Alamos, encouraged us to begin our own investigations.

1.6: previous direct measurements

Figure 1.6 presents the proposed limits for the $^{26}\text{Al}(p, \gamma)^{27}\text{Si}$ reaction rate prior to this work. The lower limit includes resonances seen directly in (p, γ) measurements, while the upper limit includes possible lower-energy resonances identified by transfer reactions. The Hauser-Feshbach calculation of Woosley et al. (WOO78), which has been used for low-temperature modeling, is also indicated. Note that at $T_9 = 0.07$, for example, there are some eight orders of magnitude uncertainty. Note also that the natural decay of ^{26}Al or its reactions with neutrons, if present, may well dominate its destruction at these low temperatures. These possibilities will be discussed in Chapter 6.

Buchmann et al. (BUC84a, BUC84) produced an ^{26}Al target having 1.5×10^{15} atoms/cm², and mapped out the excitation function for $^{26}\text{Al}(p, \gamma)^{27}\text{Si}$ from $E_p = 170 \rightarrow 1600$ keV. Resonances below 800 keV were observed at 287, 376, 719, 727, and 790 keV. The isotope ratio of $^{26}\text{Al}/^{27}\text{Al}$ in their targets was only 0.05 and yields from known $^{27}\text{Al}(p, \gamma)^{28}\text{Si}$ resonances were down elevenfold from that of ^{27}Al blanks, indicating further dilution from impurities and subsequent loss in sensitivity. In addition, several regions of the excitation function were obscured by (p, γ) reactions on target contaminants. It was clear that a cleaner target would have significantly improved sensitivity.

1.7: previous indirect measurements

Lower-energy proton resonances, too weak to be observed experimentally using (p, γ) , were investigated by transfer reactions. Various means of populating ^{27}Si states are presented in Figure 1.7. Concurrently with our initial investigations, Schmalbrock et al. explored the excitation region in ^{27}Si just above the $^{26}\text{Al}+p$ mass ($E_x = 7465$ keV in ^{27}Si) using the $^{28}\text{Si}(^3\text{He}, \alpha)^{27}\text{Si}$ reaction (SCH86). Since the reduced proton width can not be determined in this manner, a limit of $\theta^2 = 1$ was assumed in order to assess the possible contribution of observed levels to the (p, γ) reaction rate. She identified two states between 7465 and 7628 keV ($E_p = 0$ and 170 keV) which might correspond to (p, γ) resonances with $E_p = 68$ and 136 keV (Figure 1.8). Poor resolution and background from target contaminants prevented determination of spectroscopic properties for these states by angular distributions. Since the barrier penetration in (p, γ) depends on the l -transfer, only an upper limit (for $l = 0$) on their contributions could be established. Later attempts at Princeton (CHA87) to measure $\sigma(\theta)$ suggested $^{28}\text{Si}(^3\text{He}, \alpha)^{27}\text{Si}$ does not proceed by a first-order direct reaction as indicated by the small cross section and featureless angular distribution.

In an effort to improve this situation, Wang et al. examined the $^{27}\text{Al}(^3\text{He}, t)^{27}\text{Si}$ reaction, again populating the states of interest in ^{27}Si (WAN89). Seven states corresponding to possible resonances having $E_p < 281$ keV were identified (Figure 1.8) but the angular distributions were insensitive to the angular momentum transferred. Using $(^3\text{He}, d)$ and (α, t) reactions on a ^{26}Mg target, they re-examined spins of ^{27}Al states where one would expect to find isospin analogs to ^{27}Si states. If the analog states could be identified, then knowing the spin in ^{27}Al would limit l_p in the $^{26}\text{Al}(p, \gamma)^{27}\text{Si}$ reaction. This, along with an assumed $\theta^2 = 1$ would provide more stringent limits on proton resonance strengths.

Assuming that the $E_p = 287$ - and 376 -keV resonances have $l_p = 0$, the states populated in ^{27}Si should have spin $\frac{9}{2}$ or $\frac{11}{2}$, an assumption supported by the spin assignments found in (BUC84) (based on the the γ -ray cascade schemes). The analogue states in ^{27}Al are observed at 7807 and 7935 keV. The next lowest high-spin state in ^{27}Al at 7661 was then postulated to have its analogue in ^{27}Si at 7533 or 7589 keV, corresponding to a possible $l = 0$ resonance in $^{26}\text{Al}(p, \gamma)^{27}\text{Si}$ at $E_p = 72$ or 130 keV. An upper limit on $\omega\gamma$ for these states was thus established, using $l = 0$ and $\theta^2 = 1$. The other states were presumed to have $l_p \geq 2$ and were not initially included in calculating $\langle\sigma v\rangle$ (WAN86).

Ignoring a state solely because of the proton l -transfer required can only be justified if the resulting barrier penetrability reduces its strength, assuming $\theta^2 = 1$, to the point that the resulting $\langle\sigma v\rangle$ rate is negligible for the astrophysical problem at hand. Otherwise, it is only by comparison to other resonances that one can justify ignoring a possible resonance. Since the reduced proton widths of the low-lying resonances seen in Wang's work are unknown, such a comparison is impossible. Consequently, the final work submitted by Wang et al. for publication (WAN89) includes all the states, giving each its full Wigner limit and assuming the minimum l -transfer for each.

Table 1.1 lists all the known or suspected $^{26}\text{Al}(p, \gamma)^{27}\text{Si}$ resonances below $E_p = 400$ keV and their strengths prior to the current work. Better limits for the lower states could be obtained using the $^{26}\text{Al}(^3\text{He}, d)^{27}\text{Si}$ reaction which should proceed as a first-order direct proton transfer, giving an angular distribution characteristic of the l -transfer and having a cross section proportional to the reduced proton width. We believed a suitable target could be fabricated and much of the uncertainty resolved.

1.8: scope of current work

We have argued that the $^{26}\text{Al}(p, \gamma)^{27}\text{Si}$ reaction rate is astrophysically important, and that, with improved targets, significant progress could be made in its determination, especially at lower temperatures. The remaining chapters describe these experimental investigations.

Chapter 2 details the target production methods and some of their problems. Direct (p, γ) measurements are described in Chapter 3, and indirect $(^3\text{He}, d)$ measurements are presented in Chapter 4. Chapter 5 re-visits some of the lowest (p, γ) resonances using a different detector, prompted by interesting limits obtained in the $(^3\text{He}, d)$ experiment. Chapter 6 then summarizes the new reaction rates, discusses the consequences, and points to future directions.

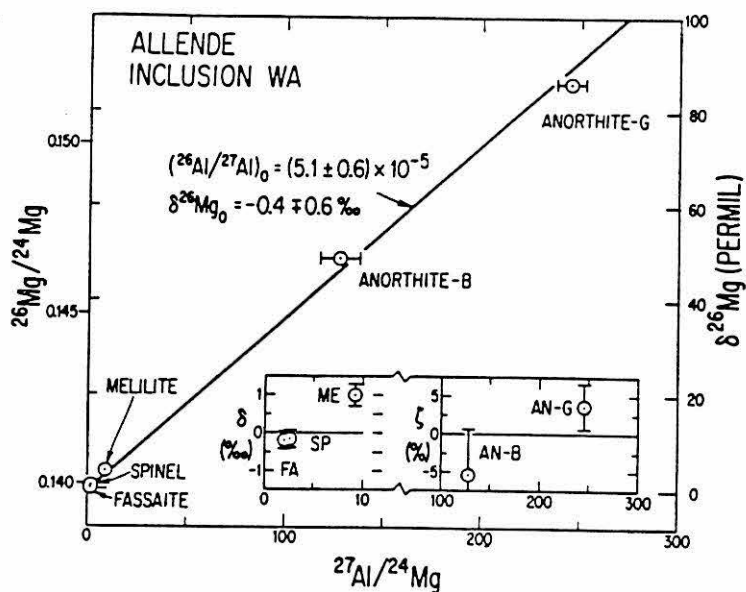


Figure 1.1. Isotope Correlation in the Allende Meteorite. This internal isochron was defined by four coexisting phases and is taken from (LEE77). No significant variations of $^{25}\text{Mg}/^{24}\text{Mg}$ were found. The inset shows deviations from the best-fit line.

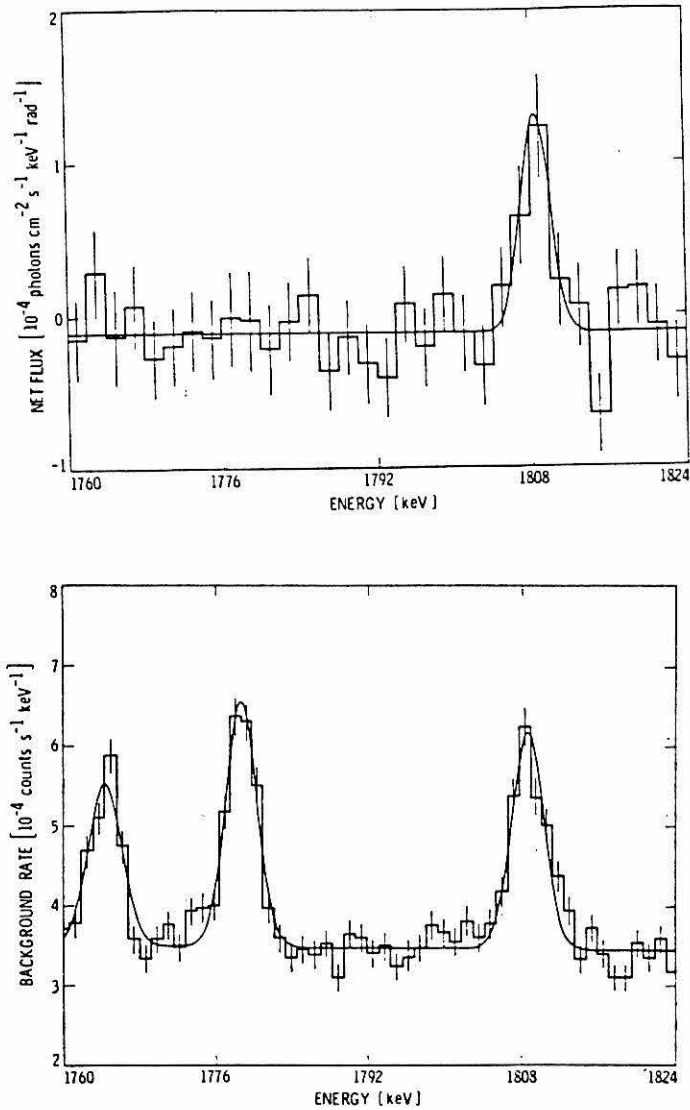


Figure 1.2. HEAO3 Detection of the 1809-keV γ -ray line. Using four high-purity germanium detectors having 3.3-keV resolution at 1809 keV and 42° FWHM effective aperture, a 5σ detection (upper figure) was made above background (lower figure). The background lines at 1779- and 1809-keV both come from neutron interactions in the spacecraft structure. An assumed galactic distribution relates the net 1809 flux of $(4.8 \pm 1.0) \times 10^{-4} \text{ cm}^{-2} \text{ s}^{-1} \text{ rad}^{-1}$ to about $3 M_{\odot}$ of ^{26}Al . This figure is taken from (MAH84).

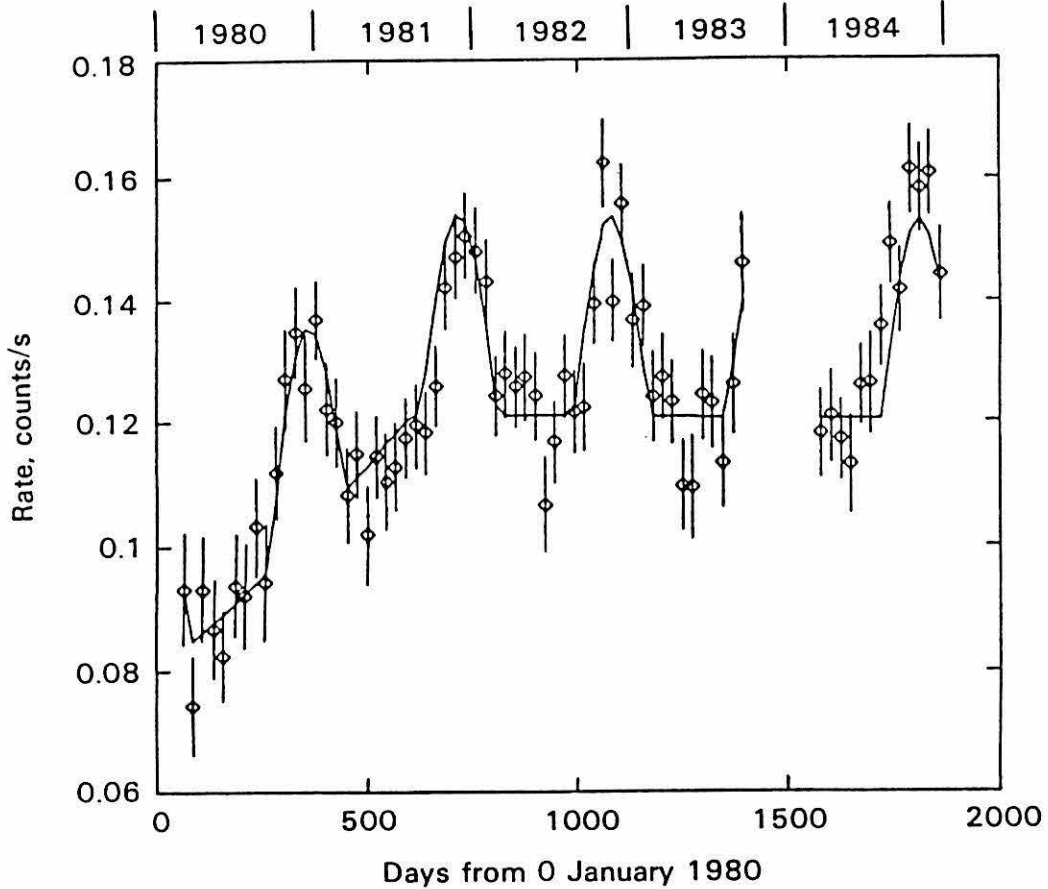


Figure 1.3. SMM Detection of 1809-keV γ -ray line. Using seven NaI detectors with a combined resolution of 95 keV at 1809 keV and 130° FWHM effective aperture, a 10σ detection was made above a rising background due to the buildup of ^{22}Na in the spacecraft. (The 1275-keV γ -ray and 511-keV annihilation quanta from $^{22}\text{Na}(\beta^+)^{22}\text{Ne}$ sum into the region of interest.) Each time the galactic center passed through the detector's field of view the fitted yield around 1809 keV increased, indicating a net flux of $(4.0 \pm 0.4) \times 10^{-4} \text{ cm}^{-2}\text{s}^{-1}\text{rad}^{-1}$ from the galactic center. This figure is taken from (SHA85).

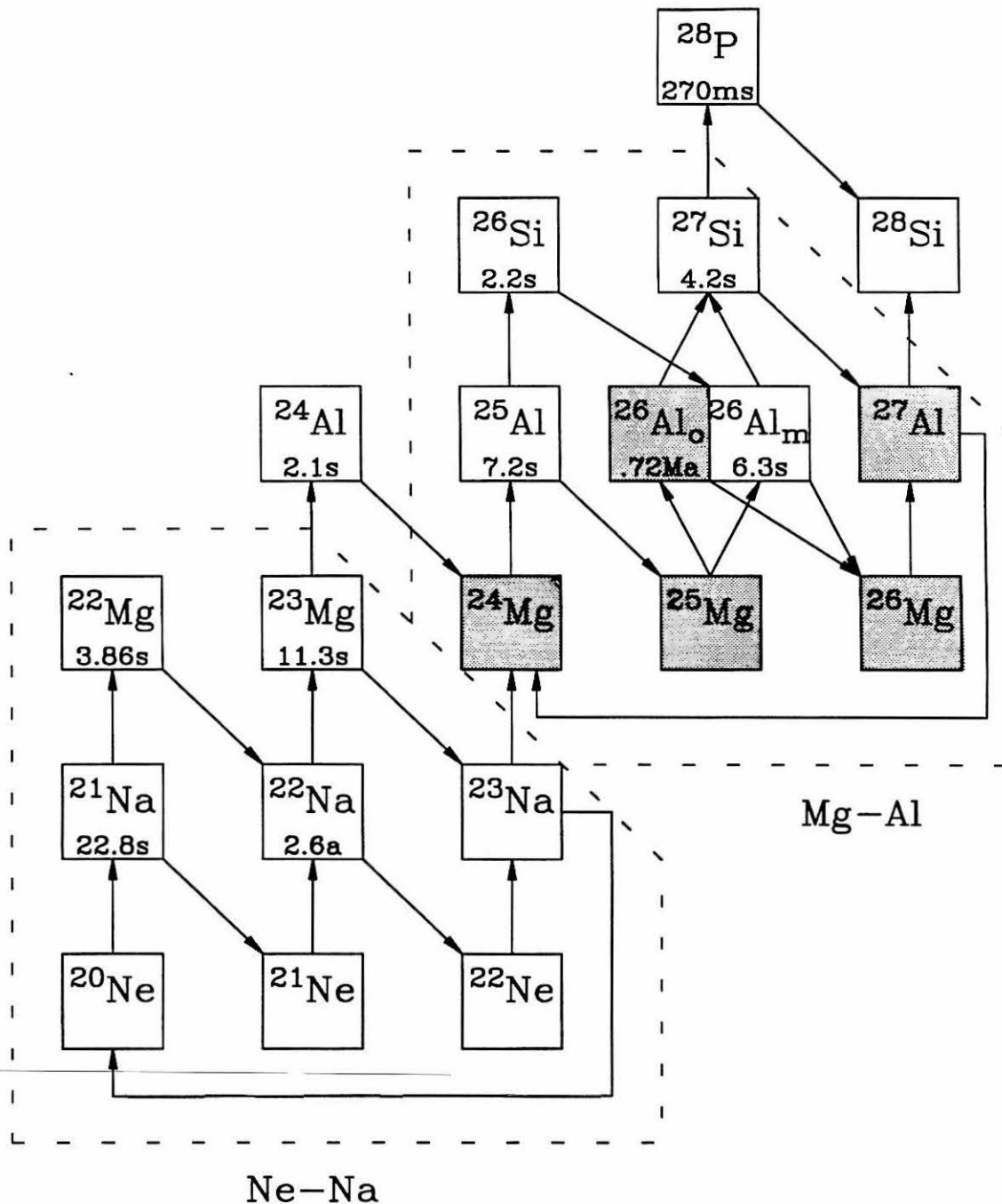


Figure 1.4. The Mg-Al Cycle. The reactions indicated are (p, γ) , (p, α) , or β^+ . The dominant nuclei at low temperatures have been shaded. For $T_9 \leq 0.4$ the ground state and the 228-keV isomeric state of ^{26}Al fall out of thermal equilibrium and must be treated as separate species (WAR80). The Ne-Na cycle is also illustrated.

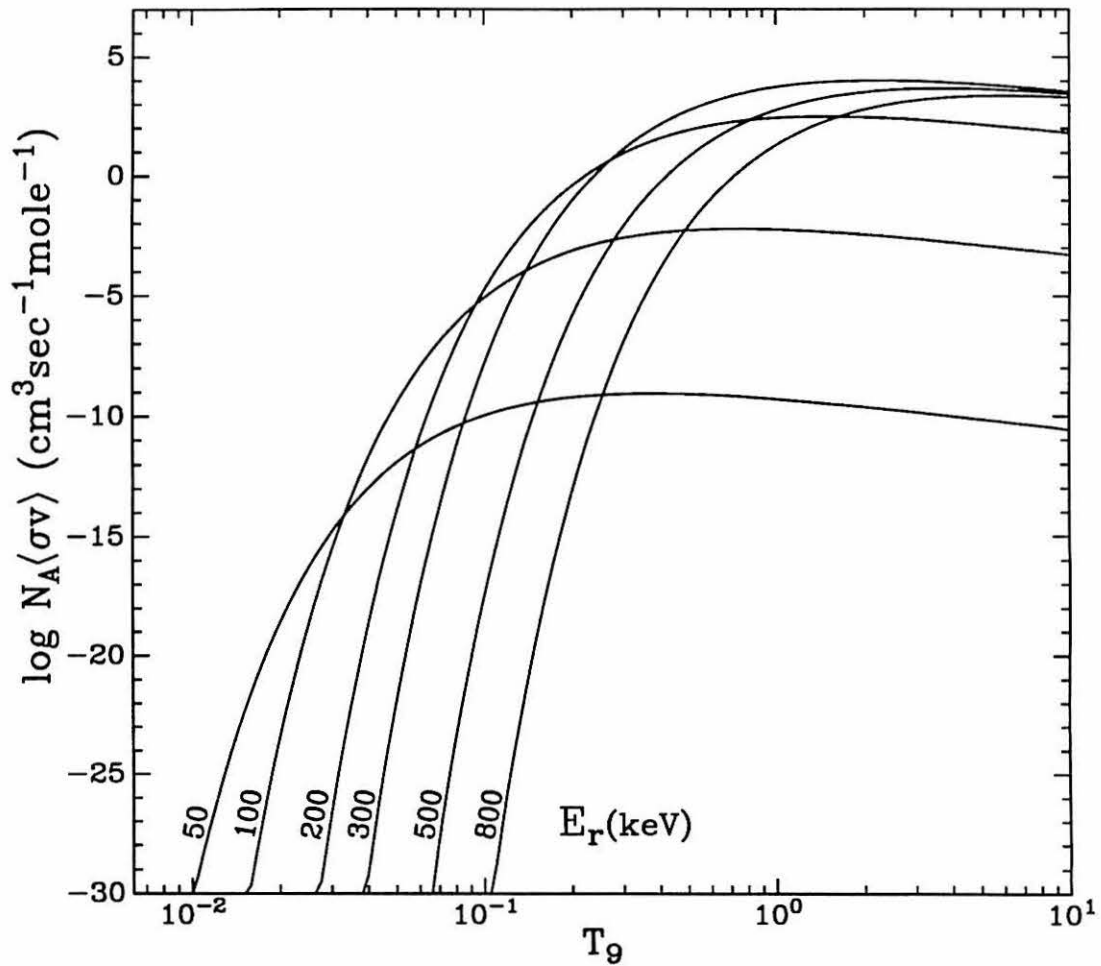


Figure 1.5. Example Stellar Reaction Rates. The stellar reaction rate due to an $^{26}\text{Al}(p, \gamma)^{27}\text{Si}$ resonance is displayed for a variety of resonant energies. Note the significance of individual resonances below $T_9 = 1$. The strength assigned each resonance was an estimated upper limit (see text). N_A is Avogadro's number.

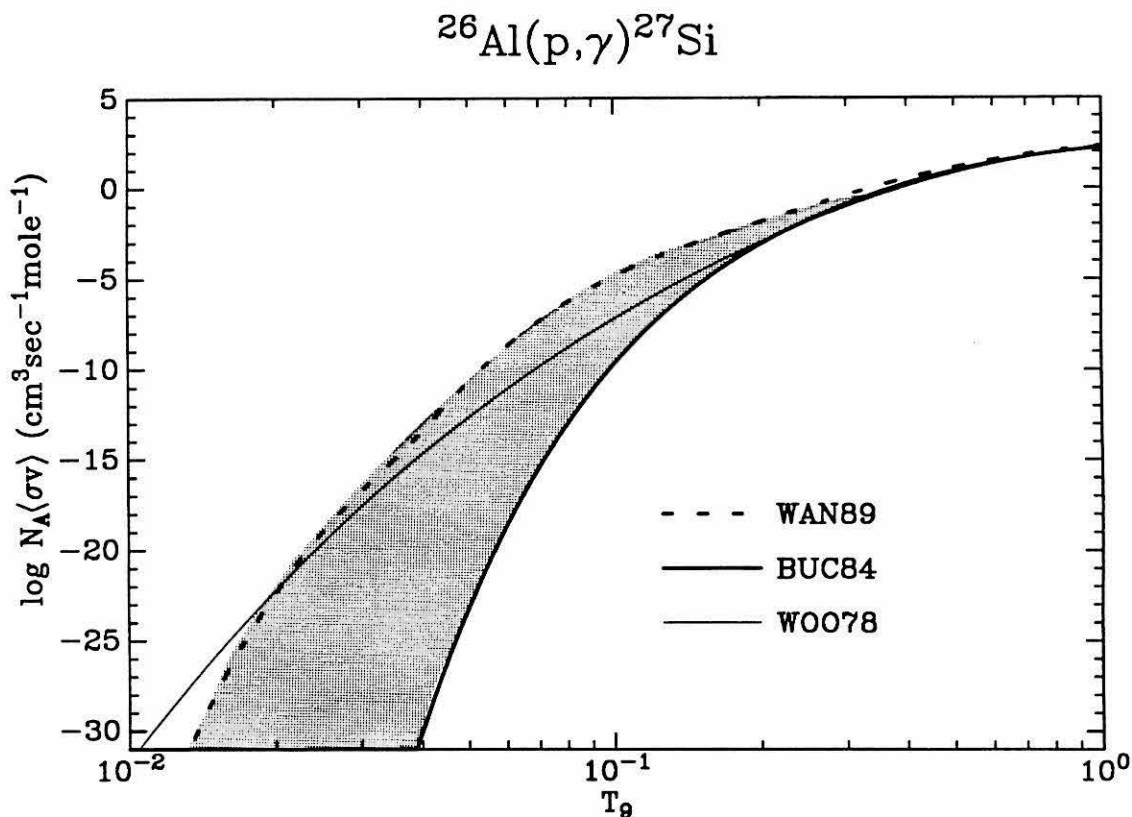


Figure 1.6. The Proton Destruction Rate of ^{26}Al . Previous limits for this rate are shown. The lower limit arises from directly observed resonances while the upper limit assumes the maximum possible contribution of other states identified through transfer reactions. The Hauser-Feshbach calculation by Woosley is also shown.

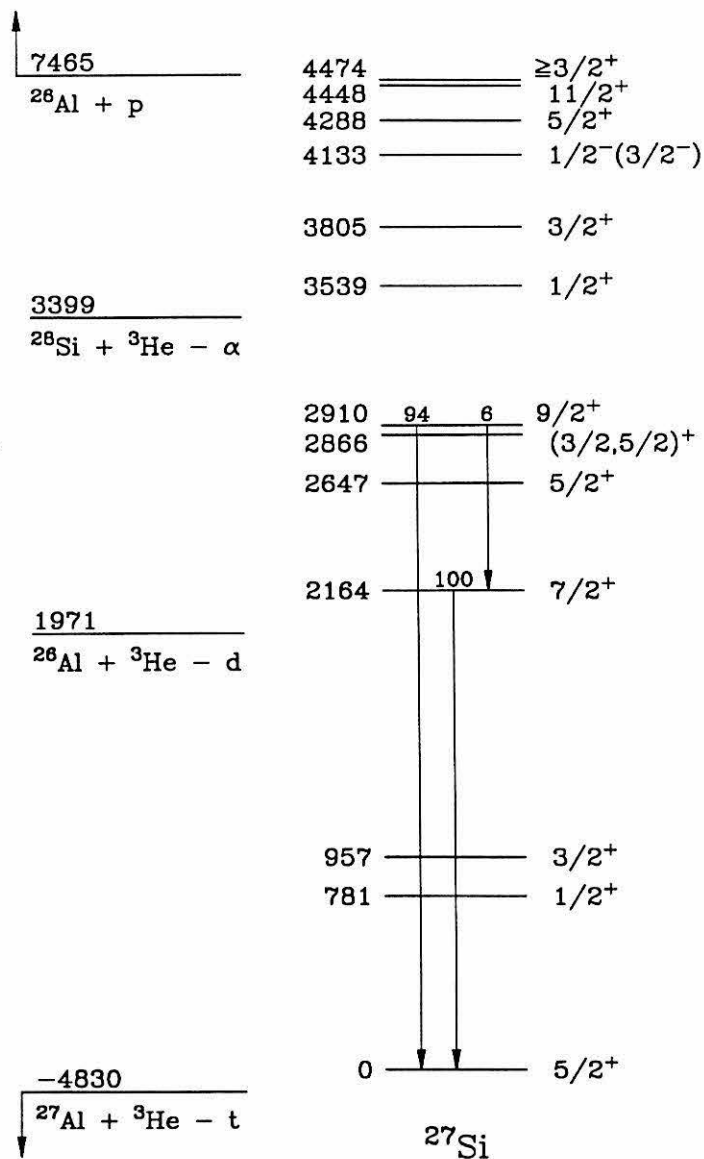


Figure 1.7. Energy Levels in ^{27}Si . The reactions displayed have been used to examine states in ^{27}Si near the proton threshold. This figure also identifies two key levels (2164, 2910) which appear in the cascade scheme of every (p, γ) resonance observed in this work. Energies are in keV.

Figure 1.8. States in ^{27}Si near the $^{26}\text{Al} + \text{p}$ Mass. Currently known ^{27}Si states relevant to the (p, γ) reaction rate are identified by the reactions in which they appear. Direct (p, γ) measurements were performed by Buchmann (BUC84), while $(^3\text{He}, \alpha)$ data are from Schmalbrock (SCH86) and $(^3\text{He}, \text{t})$ from Wang (WAN89). States in ^{27}Al were re-examined by Wang and the dashed lines indicate his isospin analog identifications. Proton energies are taken from Buchmann and Wang. Energies are in keV.

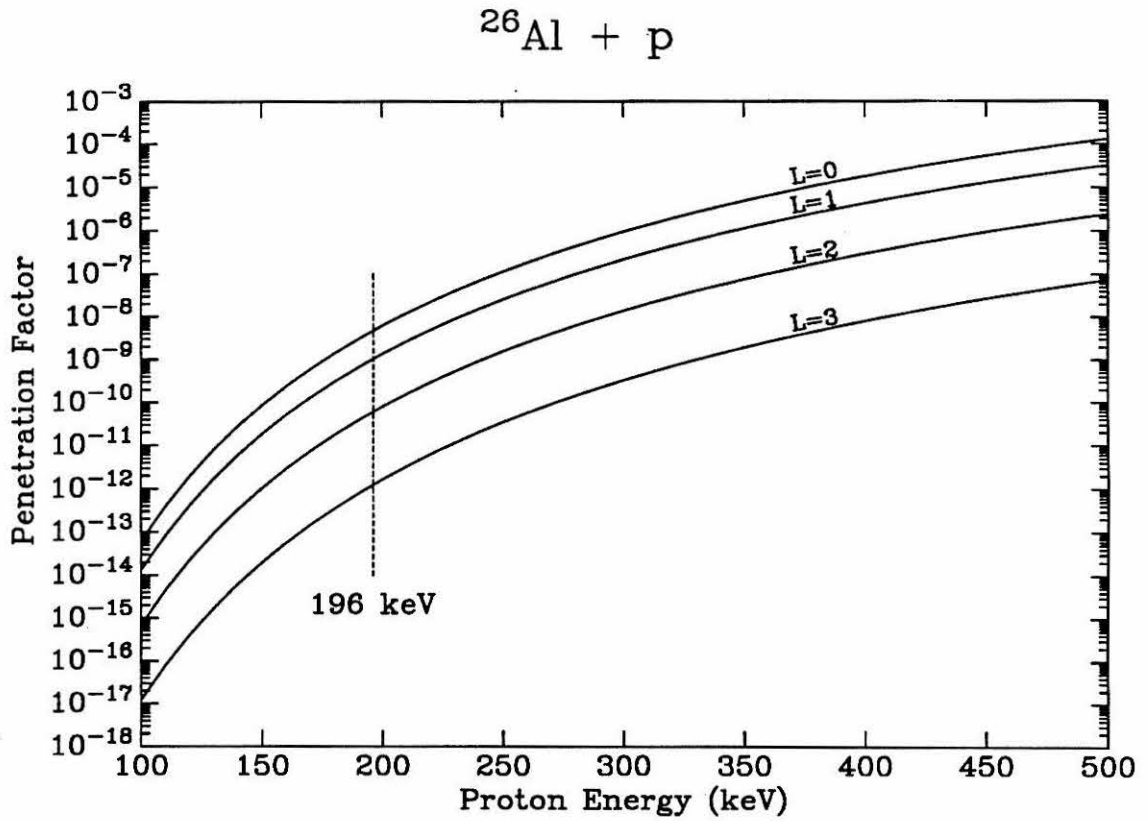


Figure 1.9. Coulomb-Barrier Penetration for $^{26}\text{Al} + \text{p}$. The penetration factors graphed here were defined in Section 1a and calculated using the formulation of Humblet, Fowler and Zimmerman (HUM87).

Table 1.1

Previously Known $^{26}\text{Al}(p, \gamma)^{27}\text{Si}$ Resonances
 $E_p \leq 400$ keV

E_p (keV)	Direct $(p, \gamma)^\dagger$ $\omega\gamma$ (meV)	Transfer Reactions ‡ $\omega\gamma$ (meV)
72	—	$< 2.3 \times 10^{-10}$
97	—	$< 1.9 \times 10^{-7}$
130	—	< 0.0057
196	—	< 0.042
235	—	< 0.62
247	—	< 1.2
287	3.8 ± 1	—
376	$65. \pm 18$	—

† (BUC84)

‡ (WAN89)

CHAPTER 2

Target Production

The ^{26}Al used was produced at LAMPF by spallation reactions of a nominally 750-MeV proton beam traversing an electronics-grade silicon crystal ("hockey puck"). The total fluence of protons over a two-year period was about 10^{23} , or 1 gram, producing $11\ \mu\text{Ci}$ of ^{26}Al . Mass-spectrometric analysis indicated an $^{26}\text{Al}/^{27}\text{Al}$ ratio of $0.062 \pm 1\%$ (THO83). We requested and received an aliquot containing $0.38\ \mu\text{Ci}$ ($20\ \mu\text{g}$) dissolved in 3.5 ml of 6.0M HCl. The analyzed impurities in this sample are listed in Table 2.1.

2.1: preparation of sample

All chemistry performed at Caltech was done with small aliquots of our total sample, sufficient only for the target under consideration. Factors determining the actual target thickness desired will be presented in Chapters 3 and 4. Typical amounts were $100\ \mu\text{l}$ containing $10\ \mu\text{g}$ of Al ($\approx 6\%$ ^{26}Al). Care was taken to avoid any unaccountable loss and the activity was followed through the chemistry using a well-type NaI detector. Argon used for taking solutions to dryness was bubbled through a slightly acidic water trap to catch any AlCl_3 which might have volatilized (none was ever detected). The chemical reagents were ultra-pure grade to avoid any further ^{27}Al contamination and the water was multiply distilled.

Our initial attempts to precipitate the Al^{3+} as $\text{Al}(\text{OH})_3$ were unsuccessful as we were unaware of the residual oxalate in the sample (from chemistry done at Los Alamos) which acted as a masking agent. To remove this oxalate, the solution was taken to dryness under an argon jet while in a $50\ ^\circ\text{C}$ water bath, re-dissolved in 70% perchloric acid, and then heated for an hour in a $142\ ^\circ\text{C}$ oil bath. The solution was again brought to dryness while heating the distillation apparatus with electrical heating tape to avoid condensation. The residue was picked up in $5\ \mu\text{l}$ of perchloric

and then diluted with 50 μl of water. Initially, this process was repeated but to no apparent advantage.

$\text{Al}(\text{OH})_3$ was precipitated with 10 μl of 13M NH_4OH , which tends to buffer the pH, preventing the amphoteric Al from re-dissolving. Gentle heating and mixing, followed by centrifuging, resulted in a minute translucent precipitate. The supernate was drawn off and saved, as precipitation was typically only 85% efficient. The precipitate was subsequently washed three times with 100 μl of water, losing 2% per wash. The remaining $\text{Al}(\text{OH})_3$ was then finally picked up in 5 μl of dilute acid.

2.2: molecular plating (targets 1-4)

Pure aluminum targets would result in the highest sensitivity possible, but several factors prevented their realization. Aluminum can not be electroplated directly from an aqueous solution since water is more easily reduced, nor is Al readily reduced to the metal (which could then be evaporated). Only the fluoride and oxide were considered reasonable target compounds which could be evaporated onto appropriate backings. However, AlF_3 is suitable only for proton energies below 340 keV due to strong fluorine resonances at higher energies, and refractory Al_2O_3 would require extremely high evaporation temperatures. Thus the molecular plating technique of Aumann and Müllen (AUM74) was investigated. Their method is to disperse the metal ion, dissolved in a small amount of acid, into an organic solvent. The resulting organic complex can then be electrodeposited with high efficiency. Subsequent heating in air will burn the metal complex to its oxide.

Platinum backings were chosen, allowing the targets to be flamed to red heat in air, converting the organic complex to Al_2O_3 , and later permitting us to burn off beam-induced carbon buildup. Later recovery of the ^{26}Al is also simpler from a noble-metal substrate. The backings were 9/16" in diameter and 10 mil thick. After some investigation into polished backings, it was concluded that an organic-solvent wash, light etch, distilled-water rinse, and heating to red heat was suitable substrate

preparation. No background was expected from the Pt backings due to its high Z . However, boron was found as a contaminant in the Pt and proved troublesome. Oxygen has only a small direct-capture cross section for protons below 2.6 MeV and gave unobtrusive background. (However, in the ^3He , d work, oxygen gave a very prominent deuteron background group.)

The plating equipment for making ^{26}Al targets #1 \rightarrow #4 is shown in Figure 2.1. A 5/16" hole in the teflon mask defined a 0.5 cm² target area, compatible with a final beam collimator of 3/16" diameter. After the final wash, the $\text{Al}(\text{OH})_3$ was dissolved in 5 μl of 1.6 N HNO_3 , dispersed in 1 ml isopropanol, and transferred to the quartz plating tube. A plating voltage of 240 volts gave a current of 1.7 mA, which over the 1.5-hour plating time dropped to 1.5 mA. The platinum anode strip was rotated continuously to ensure mixing. The plating solution was then removed with a pipette and the targets allowed to dry. They were then brought to red heat from the reverse side with a Bunsen burner to convert the aluminum to its oxide. No loss was incurred in this step. Plating efficiency was typically 94%, giving an overall efficiency from initial sample to target of about 60%.

Since the Al in the targets was 94% ^{27}Al , the $E_p = 992$ keV resonance in $^{27}\text{Al}(p, \gamma)^{28}\text{Si}$ was used as a diagnostic tool. Yield of this narrow ($\Gamma = 100$ eV) resonance, compared to that of pure Al_2O_3 or solid Al blanks, provided a measure of target stoichiometry. Raising the incident beam energy integrates this resonance further below the surface. The resulting curve of yield versus beam energy is called an excitation function, and in this case provides a depth profile of the target whose integrated area is proportional to the areal density of target nuclei (see Chapter 3). The surfaces of these targets were determined to be about 60% Al_2O_3 , with this fraction decreasing at greater depths (Figure 2.4). Continued yield, even from energies probing substantially deeper than the expected target thickness, is believed

to arise from a non-uniform or fritted surface. The process of converting the organic complex to an oxide is not well characterized and might be responsible.

Initial runs were taken with these targets, re-examining the known resonances at $E_p = 287$ and 376 keV and searching for new resonances between 400 and 700 keV. However, these runs were plagued with target difficulties, including sputtering holes in the target with sharply focussed beams, and carbon deposition despite pressures of 5×10^{-7} torr. Figure 2.5 illustrates this latter problem. After a mere 0.5 C was accumulated on target #4, the leading edge of the 992 -keV resonance yield showed signs of carbon deposition. Had the carbon been on the surface, the Al_2O_3 target profile should be retained (ignoring straggle in surface carbon) albeit shifted to higher beam energies due to energy loss in the overlying carbon. What is observed indicates either uneven carbon deposition, or build up within the Al_2O_3 itself. Dismounting the targets and heating them to red heat in atmosphere removed the carbon as anticipated. However, the long tails of the excitation function, exacerbated by carbon deposition, gave significant yield from lower-energy $^{27}\text{Al}(p, \gamma)^{28}\text{Si}$ resonances, hampering the search for $^{26}\text{Al}(p, \gamma)^{27}\text{Si}$ resonances. The changing profile also made yield measurements difficult if not altogether unreliable. A thinner target (#1) was made to help alleviate these problems, and care was used to run a defocussed beam, adjusting with the aid of a beam-profile monitor immediately before the final collimator. However, the major difficulties remained, as seen in Figure 2.5.

2.3: evaporation of oxide (targets 5-6)

These problems prompted us to tackle the evaporation of Al_2O_3 , knowing evaporated targets enjoy a reputation of success. The ^{26}Al targets fabricated by Buchmann et al. (BUC84a) were made by the purported reduction of the oxide. However, there appears to be some discrepancy within their work. Among other problems, the final heating step before "reduction" of the Al_2O_3 took place was to heat the

carbon boat to 3000 °C for half an hour. With the boiling point of Al_2O_3 being 2980 °C, it is unclear how it survived this step. One cannot deny their success, only the explanation given.

We decided to explore possible boat materials and reducing agents, guided by the success of previous work (KAV60). During the testing stages, carbon disks were used as backings to allow the use of Rutherford backscattering as a diagnostic tool. Attempts to reduce Al_2O_3 with carbon, yttrium, or zirconium were unsuccessful and we resorted to direct high-temperature evaporation of the oxide.

Ta, W, and Re boats were attempted, but all had significant boat evaporation at the necessary temperatures, diluting the deposited Al_2O_3 . Reactor-grade graphite proved successful, and the limited amount of carbon which did evaporate could be burned off later. Figure 2.2 displays the final geometry while 2.4 illustrates the improved target quality. To minimize loss, we used a tight geometry in which the target backings had to be heat sunk. Following the final wash in the chemistry to remove oxalate, the Al_2O_3 was picked up in 10 μl of 3% HCl and transferred to a small dimple in the carbon boat. As it dried, Cl gas was given off and the residual $\text{Al}(\text{OH})_3$, with gentle heating, converted to Al_2O_3 . The bell jar was pumped to 10^{-6} torr and, monitoring the temperature with an optical pyrometer, the boat was brought to 2200 °C for 15 seconds six times, allowing five minutes cooldown between each heating. The resulting targets were finally flamed to red heat in air to burn off any carbon. Targets #5 and #6 were made in this manner, the latter being used for the complete excitation functions presented in Chapter 3. (Target deterioration under beam will be discussed there.)

The $^{26}\text{Al}/^{27}\text{Al}$ ratio in the target is needed to normalize our results, so the possibility of having added ^{27}Al to the sample during our chemical procedures (and thus reducing the ratio reported by Los Alamos), prompted us to measure it using target #6 itself. A tightly collimated 1/32" inch proton beam was used to map the

areal density of ^{27}Al by integrating the 992-keV resonance in $^{27}\text{Al}(p, \gamma)^{28}\text{Si}$. The "volume" under the plotted surface in Figure 2.6 indicates 1.86 μg of ^{27}Al present. The amount of ^{26}Al was determined to be 0.13 μg by counting the 1809-keV γ -ray activity and using the known half-life. We thus determined $^{26}\text{Al} : ^{27}\text{Al}$ to be $1 : 14.5 \pm 1$ compared to the Los Alamos value of $1 : 16.1 \pm .3$ and concluded that no dilution had occurred. The weighted average of $1 : 16 \pm .3$ was adopted.

2.4: transmission target (targets 7-9)

The transmission target for $(^3\text{He}, d)$ was also made by evaporation, but onto a thin carbon foil instead of Pt. The geometry used is given in Figure 2.3, where the Ta sheets acted as support, mask, and heat shield. Initial attempts, using a premounted self-supporting carbon foil, failed due to the excessive foil temperatures which prevented adhesion of the Al_2O_3 . Successful cooling was finally obtained by evaporating a carbon film directly onto a lightly etched 3 mil Cu foil. (The carbon film would not adhere to a mirror finish.) This double foil was then clamped to a Cu block to provide an additional heat sink. A target would be ruined occasionally if the carbon separated from the copper when exposed to the 2200 $^\circ\text{C}$ boat, but a 70% success rate during testing allowed us to proceed. In an effort to prevent the brittle Al_2O_3 from flaking off, a 10- μg overlay of carbon was deposited prior to etching away the copper foil. The carbon layer also provided a conductive surface, preventing charge buildup on the insulating Al_2O_3 during subsequent bombardment.

Figure 2.7 presents the production sequence for target #8, which was used at Princeton. The 4-layer foil (Cu,C, Al_2O_3 ,C) was laid, carbon face down, over a tantalum frame having a 1/4" hole and a thin film of vacuum grease to hold the carbon. The excess foil was folded over the edges of the frame for support. An etching solution (1 ml H_2O : 1.1 ml 13M NH_4OH : 1 gm tri-chloro acetic acid) was made to *gently* flow over the backside of the target to remove the copper foil.

The final target was analyzed using Rutherford backscattering and the results are presented in Figure 2.8.

A summary of ^{26}Al targets is given in table 2.2.

Figure 2.1. Molecular Plating Equipment.

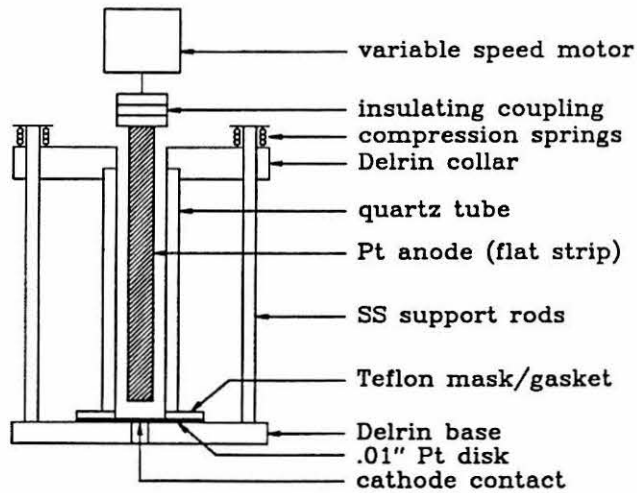


Figure 2.2. Evaporation Equipment.

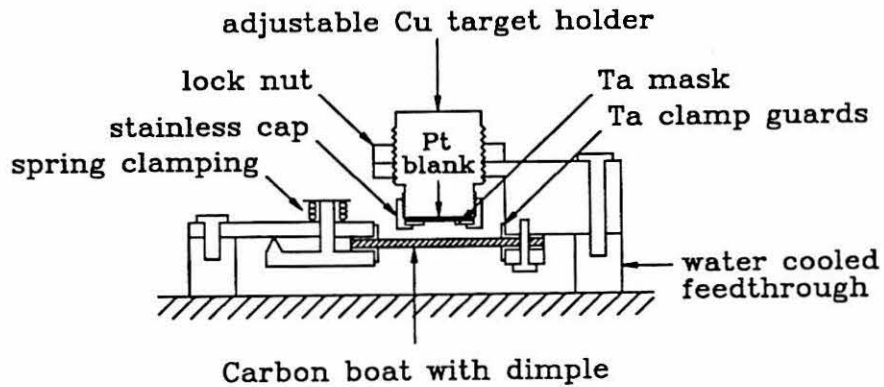
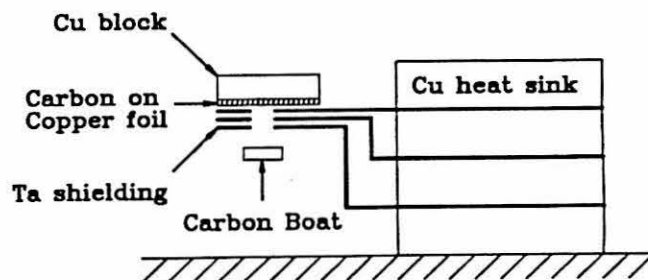


Figure 2.3. Foil Evaporation Equipment.



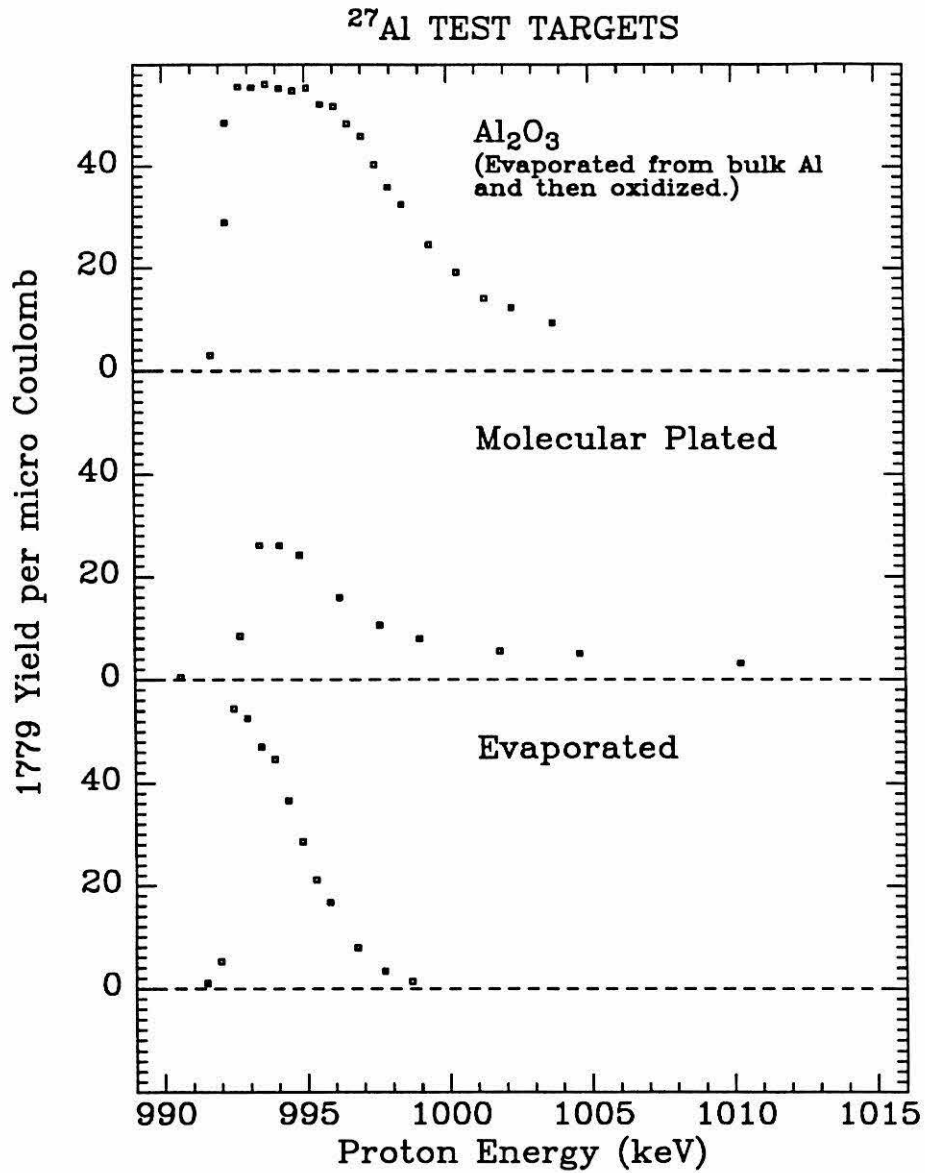
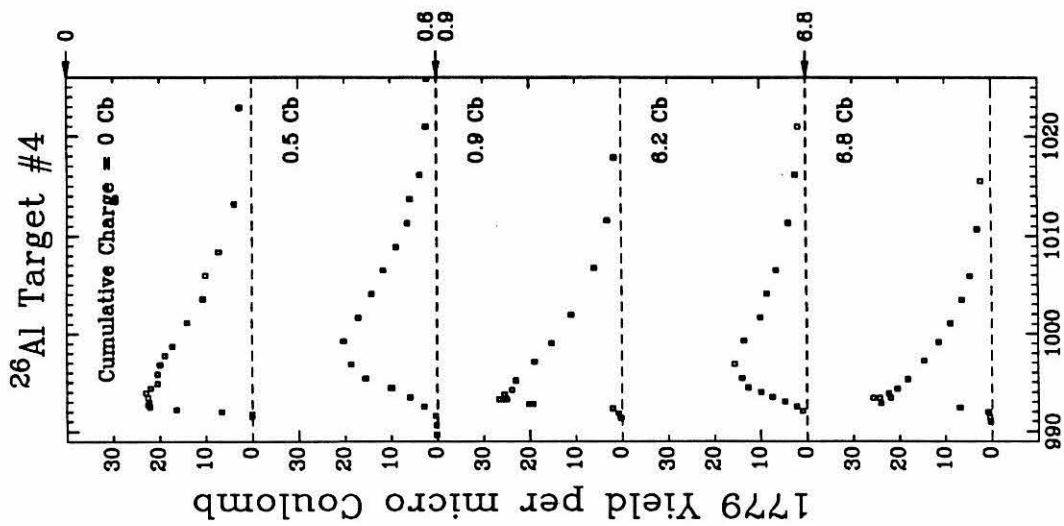
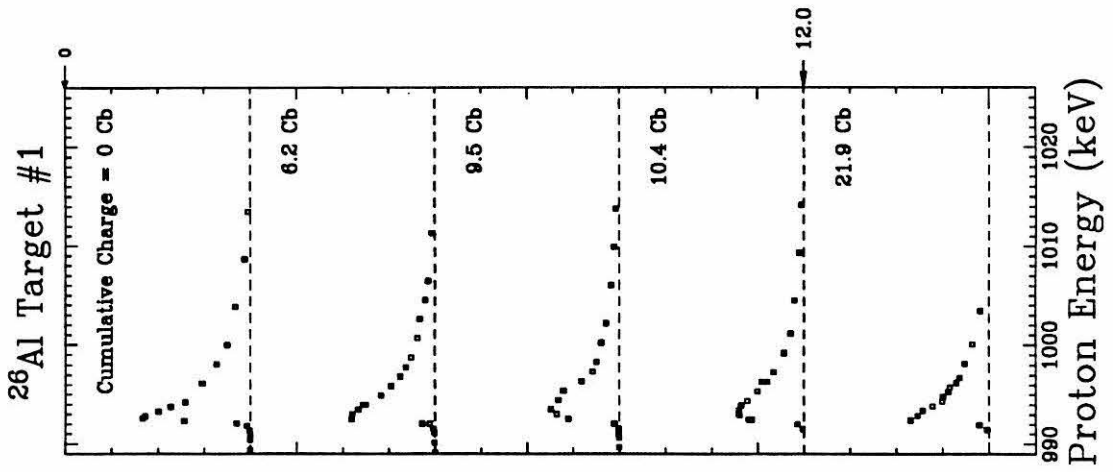
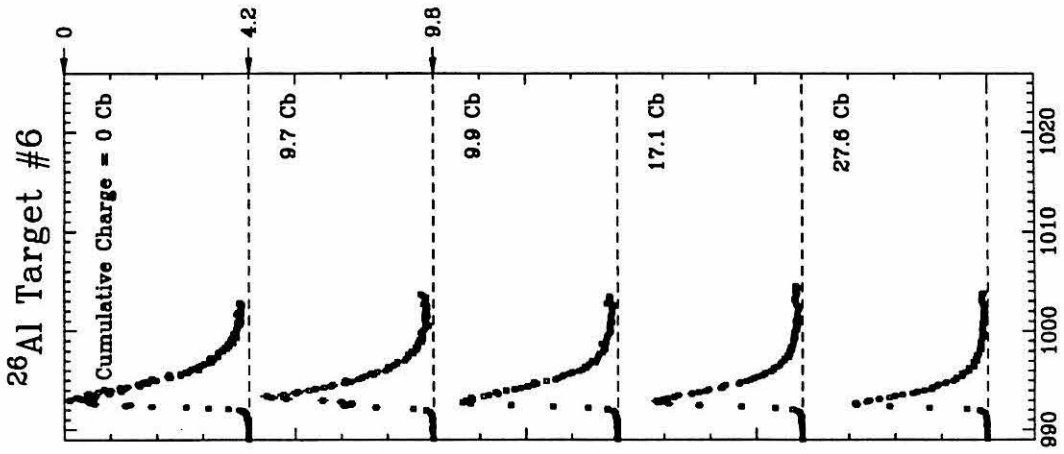


Figure 2.4. Profiles of Test ^{27}Al Targets. The narrow 992-keV resonance in $^{27}\text{Al}(p, \gamma)^{28}\text{Si}$ was used to examine target profiles as described in the text. Surface yield from the molecular-plated target is clearly down compared to pure Al_2O_3 while the evaporated target appears undiluted.

Figure 2.5. Changes in Target Profiles after Bombardment. These profiles show the change in target quality during the course of a run. The numbers to the right indicate the cumulative charge when the targets were removed and brought to red heat in atmosphere to burn off carbon build-up. Targets #1 and #4 were made by electro-deposition, while #6 was made by evaporation. Pure $^{27}\text{Al}_2\text{O}_3$ would have an ordinate value of 55. Even correcting for the 6% of ^{26}Al present, this purity was never achieved.



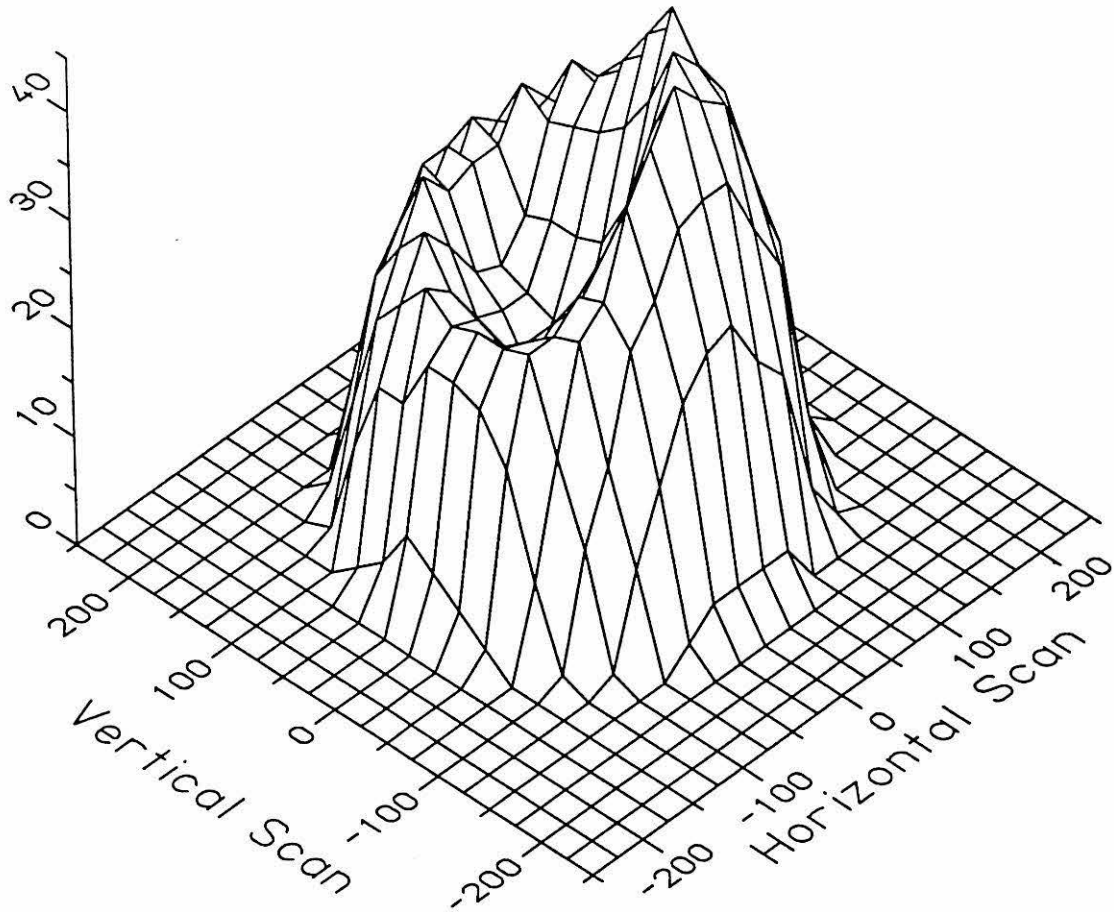
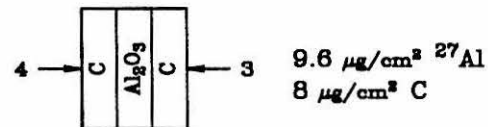
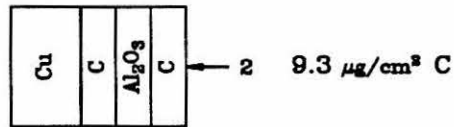
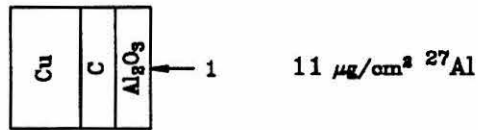
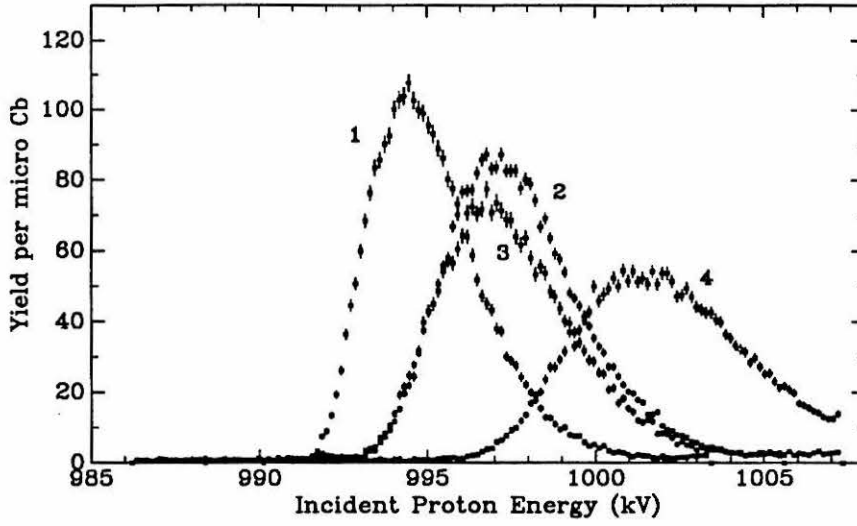


Figure 2.6. Surface Profile of ^{26}Al Target #6. This plot shows the areal ^{27}Al density in target #6, measured after receiving 28 Coulombs of incident beam. The target was rastered in 25-mil steps and at each vertex a target-depth profile was mapped out using the 992-keV resonance in $^{27}\text{Al}(p, \gamma)^{28}\text{Si}$ and a $1/32''$ -diameter proton beam. The area under each profile curve was proportional to the total ^{27}Al areal density at that location and provides the z coordinate value.

Figure 2.7. Transmission Target Production. Various stages in the production of target #8 are presented. The plotted profiles result from ^{27}Al in the target but their shapes and locations reflect dE/dx and straggle in covering layers. Leading-edge positions were used to determine the thickness of carbon films. The profiles presented are:

- 1) immediately after the Al_2O_3 evaporation
- 2) with the carbon overlay
- 3) after etching off the Cu backing.
- 4) as in 3), except from the other side of the target.

²⁶Al Foil Target
Various Stages of Production



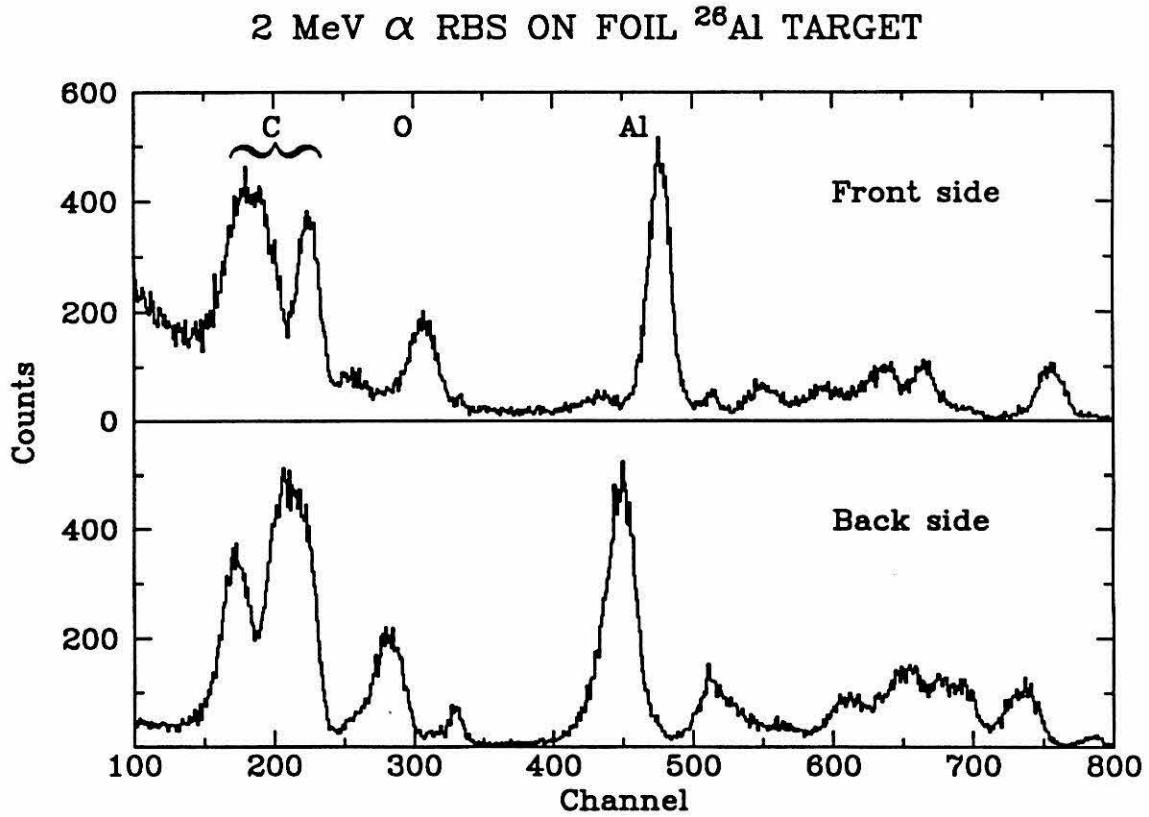


Figure 2.8. Rutherford Backscattering on Target #8. The double carbon peak from backscattered alphas reflects the target's layered structure. Reversing the target shifts the Al and O peaks by the difference in thickness of the two carbon films. Other structure comes from target contaminants and pin-holes in the carbon.

Table 2.1

Analyzed Impurities in the ^{26}Al Solution from LANL[†]

Element	Concentration ($\mu\text{g}/\text{ml}$)	Limit of Detection ($\mu\text{g}/\text{ml}$) [*]
Al	103.	0.02
B	0.95	0.05
Ca	0.23	0.001
K	0.08	0.02
Li	0.2	0.06
Mg	0.09	0.006
Na	0.58	0.001
Si	N.D.	1.7
Sr	0.005	0.001

*Limit of Detection as defined by twice the standard deviation of the blank at each element's analytical line.

[†] (BEN82)

Table 2.2
Initial Properties of ^{26}Al Targets

Target	Type	Amount of ^{27}Al		Half Width ^a (keV)	Tenth Width ^a (keV)
		$\mu\text{g}/\text{cm}^2$	(atoms/cm ²) $\times 10^{15}$		
1	mol. plated	7.8 \pm .6	174	3.1 \pm .2	13.6 \pm .6
2	mol. plated	3.5 \pm .6 ^c	78	—	—
3	mol. plated	7.8 \pm 1. ^c	174	—	—
4	mol. plated	10.7 \pm .6	328	6.2 \pm 1.	>30
5	evaporated	3.4 \pm .3	76	1.3 \pm .2	2.7 \pm .4
6	evaporated	7.3 \pm .4	163	2.8 \pm .3	7.0 \pm .5
7	evap. (trans.)	11.0 \pm 1.	245	4.4 \pm .3 ^b	—
8	evap. (trans.)	11.0 \pm .5	245	3.8 \pm .5 ^b	6.8 \pm .5 ^b
9	evap. (trans.)	6.8 \pm 1. ^c	151	—	—

- a* observed energy loss to 1-MeV protons
b before C overlay was applied
c from ^{26}Al activity

CHAPTER 3

$^{26}\text{Al}(\text{p}, \gamma)$ with a Germanium Detector

The resonance strengths can be determined from a measured excitation function by knowing the efficiency of the detector for a given γ ray which, coupled with the detected count rate per unit charge, will then allow the total target yield to be calculated. For an isolated Breit-Wigner resonance, this yield can take two limiting forms. Working in the lab frame, if the target has thickness t in centimeters, then the target energy loss is

$$\Delta E = n t \epsilon \quad \text{keV}$$

where

$$n \equiv \# \text{ atoms per cm}^3$$

$$\epsilon \equiv \text{atomic stopping power (keV cm}^2 / \text{atom)}.$$

If the resonance width Γ is in keV, then for

$$\Gamma \gg \Delta E : \quad Y = 4.102 \times 10^{-9} \frac{n t A_1}{\mu_A^2 E} \frac{f b W(\theta) \omega \Gamma_a \Gamma_b}{(E - E_r)^2 + (\Gamma/2)^2} \quad (\text{per } \mu\text{C})$$

$$\Gamma \ll \Delta E : \quad Y = 2.577 \times 10^{-8} \frac{A_1}{\mu_A^2 E_r \epsilon} f b W(\theta) \omega \frac{\Gamma_a \Gamma_b}{\Gamma} \quad (\text{per } \mu\text{C})$$

$$\text{for } E_r < E < E_r + \Delta E,$$

$$= 0 \quad \text{elsewhere,}$$

and in either case, the integrated excitation function is

$$A = \int_0^\infty Y(E) dE = 2.577 \times 10^{-8} \frac{n t A_1}{\mu_A^2 E_r} f b W(\theta) \omega \frac{\Gamma_a \Gamma_b}{\Gamma} \quad (\text{keV-counts}/\mu\text{C}),$$

provided the Γ_i do not vary appreciably over the range of several Γ . The reduced mass μ_A , and incident particle mass A_1 , are in amu, while the statistical factor ω is defined as in Chapter 1. The branching ratio for the γ ray is given by b , and its angular distribution by $W(\theta)$. As the target may contain other nuclei besides the ones of interest, f is the fraction of target nuclei to the total number of nuclei.

3.1: target considerations

Since $\Gamma < 1$ keV for all resonances of interest here, making targets thicker than a keV would not increase the yield at resonance, but would make **A** easier to measure. Beyond 10 keV though, we would no longer be able to resolve individual resonances amidst the high density of $^{27}\text{Al}(p, \gamma)^{28}\text{Si}$ resonances. Consequently, we aimed for a target 5 keV thick to 1-MeV protons, having $14 \mu\text{g}/\text{cm}^2$ of Al as Al_2O_3 . Because of the target difficulties previously described, the resonance yield **Y**, which depends on ϵ , was suspect. However, the integrated yield **A** is independent of target stoichiometry, and instead depends on mapping out a complete yield profile of the target.

3.2: experimental setup

To reduce the possibility of systematic errors in these maps, we decided to apply a (0 \leftrightarrow +20) kV ramping voltage to the target chamber, in effect varying the incident beam energy. By measuring yield versus ramp voltage, we were able to acquire a complete target profile in a single run, even when using H_2^+ beams. This approach had additional benefits. Several runs included the leading edge of an $^{27}\text{Al}(p, \gamma)^{28}\text{Si}$ resonance, which then provided an internal beam-energy calibration. Using the ramp also gave us a virtually continuous excitation function, eliminating the possibility of missing a high point. And finally, repetitive re-tuning of the accelerator was minimized.

The target region is diagrammed in Figure 3.1. A 35%, intrinsic germanium detector (Ortec HPGe #26-P14P) was placed in close geometry at 0° to increase efficiency and reduce angular-distribution dependence. Its proximity was limited by the need to stand off 20 kV and to provide direct water cooling to dissipate the 50 watts of beam power. Finite-detector coefficients for a 3-MeV γ ray were $Q_2 = 0.41$, and $Q_4 = -0.03$ in the notation of Rose (ROS53). A two-inch lead house

was erected to reduce room background. We sealed the Pt-backed targets directly to the stainless steel target chamber using a 20° bevel, allowing the system to be baked. Targets could be resealed several times, which permitted their occasional removal to burn off carbon.

To determine the relative detector efficiency versus γ -ray energy, a ^{56}Co source was mounted on a standard Pt backing and installed in the target chamber. Its known decay scheme, corrected for summing but not angular correlations, provided this information from 0.8 to 3.5 MeV. To extend the curve to 10.8 MeV we ran beam on a 10-mil Al blank and used the known cascade scheme of the 992-keV resonance in $^{27}\text{Al}(p, \gamma)^{28}\text{Si}$ (ANT77), correcting for summing, but not angular distributions. Finally, to extend the curve to the 417-keV line arising from (p, p_2) on ^{26}Al , the $^{16}\text{O}(p, \gamma)^{17}\text{F}$ direct capture reaction was employed. At $E_p = 800$ keV this gives a 1354-keV line in coincidence with a 495-keV line so the efficiency can be scaled. We corrected for summing and angular distributions using the work of Rolfs (ROL73). Absolute normalization was made to NBS source #4275 (a mixture of ^{125}Sb , ^{154}Eu , and ^{155}Eu calibrated to $\leq 1\%$). The resulting photopeak-efficiency curve is presented in Figure 3.2.

Our energy resolution was typically 3.4 keV for a 1.33-MeV γ -ray, despite efforts to attain the 1.7-keV specifications of the detector. Some of this problem came from our desire to record up to 14-MeV γ rays which translated every millivolt of noise to the ADC into a 2-keV energy spread. The expected (or observed) locations of peaks corresponding to known transitions were identified in the 8K pulse-height spectra collected. With this information, a software window was established encompassing several channels about this location to allow for the system resolution. An additional window was established on either side of this peak window (being careful not to include any other lines) to determine the background level. Events in each window were then binned into 256 channels according to the ramp voltage. To allow

later extraction of an arbitrary line, an additional lower-resolution two-dimensional spectrum (4096×16) was collected.

Dead time was monitored and corrected for as a function of ramp voltage by introducing a 20 Hz pulser peak at the top of the spectrum and setting a software window about it. Other excitation functions were then divided by that of this window. This method also corrected for any non-linearity in the ramp (which was in fact linear to within 0.5%). In addition, possible corona and leakage currents due to the high voltage were monitored and corrected for by binning the integrated charge against the ramp voltage. Visual inspection of this spectrum identified runs which had some leakage. In these cases the extrapolated zero-voltage charge was used to correct for "missing" charge at the higher voltages. Some distortions of this spectrum arose because of the capacitive charging and discharging of the target chamber and cooling system as the ramp voltage rose and fell. However, current integration could always be corrected to the 3% level. The voltage monitor of the electrically isolated HV supply was coupled out through a FET, while virtual ground was established through the current integrator.

The variable-energy proton beam was provided by Caltech's NEC-3UDH Pelletron Accelerator using the internal *rf* ion source. A substantial effort eventually enabled us to obtain $100 \mu A$ of protons on target with regularity, though we chose never to exceed 50 watts of beam power. Below $E_p = 350$ keV an H_2^+ beam was used because the beam optics were better at higher terminal voltages. The 0° beamline constructed for this experiment maintained a pressure of 5×10^{-7} torr. The final $3/16''$ diameter, water-cooled collimator was followed by a $1/4''$ diameter beam wipe to prevent scattered beam from hitting a -300 V suppression ring used to assure proper current integration. A beam-profile monitor was located immediately prior to the collimator so we could deliberately over-focus the beam.

3.3: excitation function

Using the above arrangements, an excitation function with target #6 was taken from 170 to 1000 keV using about 2×10^{20} protons (30 C). Target loss was measured and corrected for by frequent determinations of A for the $E_p = 992$ -keV $^{27}\text{Al}(p, \gamma)^{28}\text{Si}$ resonance. The measured loss is shown in Figure 3.4 and was nearly linear with accumulated charge, allowing target thickness corrections to be made by linear interpolation. The limited scatter in the data reflects our ability to deliberately over-focus the beam and thus average over the loss pattern seen in Figure 2.6. The previously known $^{26}\text{Al}(p, \gamma)^{27}\text{Si}$ resonances were re-measured early on, and once again later, during the course of a complete excitation function. In every case but one, the deduced resonance strengths, corrected for the intervening target loss, were in agreement to within 10%. (The deviant run gave a 50% higher yield for the 286-keV resonance, but was discarded due to multiple computer failures from unknown causes during the course of the run.)

The ground-state spin of ^{26}Al is 5^+ , so proton resonances having a small l -transfer will populate high-spin states in ^{27}Si . These are then expected to preferentially cascade to the $\frac{5}{2}^+$ ground state through high-spin intermediate states. Figure 1.7 suggests the $2910 \left(\frac{9}{2}^+\right) \rightarrow 0$ and $2164 \left(\frac{7}{2}^+\right) \rightarrow 0$ transitions as candidates. Indeed, all the $^{26}\text{Al}(p, \gamma)^{27}\text{Si}$ resonances observed with the germanium detector appear in the excitation function of the 2164-keV line.

A γ ray having several MeV could manifest itself several ways in the germanium detector, and a typical spectrum is presented in Figure 3.3. (Complete spectra for each resonance are available in the Appendix.) About 1% of the γ rays deposited their full energy and appeared in the "photo peak" while a comparable number appeared in each of two escape peaks corresponding to the escape of one or two annihilation quanta following pair production. Another 10% Compton scattered from electrons which then provided a continuous background below the "Compton

edge.” It was this continuous background from contaminant (p, γ) reactions which limited our sensitivity at several bombarding energies. However, the background near 2164 keV was generally dominated by target activity—Compton events from the 1809-keV γ ray from ^{26}Al decay summing with annihilation quanta from the emitted β^+ .

To gain an understanding of the background, we plotted the excitation function of a window encompassing all events which deposited between 2630 keV and the maximum energy possible for $^{26}\text{Al}(p, \gamma)^{27}\text{Si}$ resonances (Figure 3.5). As expected, ^{27}Al was the dominant source of background, and “tails” in the target profile compounded the problem. Analyzing the pulse-height spectrum at each resonance identified the nuclei responsible and, using known resonance strengths, allowed us to determine the target composition as presented in Table 3.1. Note that the critical region below $E_p = 200$ keV was obscured by the 163-keV resonance in $^{11}\text{B}(p, \gamma)^{12}\text{C}$ from B at depth.

The net 2164-keV yield versus beam energy was obtained using a 6-keV software window centered on the expected photopeak location, and a similar background window on either side. Twelve resonances were observed, five of which had not been seen before. Figure 3.6 presents the excitation function for this line, along with the upper limits from Buchmann et al. (BUC84). The locations of known $^{27}\text{Al}(p, \gamma)^{28}\text{Si}$ resonances are indicated, which correspond to regions of large background. Special attention was also paid to proton energies which would populate known states in ^{27}Si . For example, the new resonance at 770 keV corresponds to the $E_x = 8206$ state seen in $^{27}\text{Al}(^3\text{He}, t)^{27}\text{Si}$. Excitation functions were also routinely monitored for the 2910-keV photopeak, as well as transitions from the entrance $E_x \rightarrow 0^-$, 2164-, and 2910-keV states, correcting for Doppler and recoil energy shifts. The 417-keV region was monitored for possible (p, p_2) resonances, populating the second excited state of ^{26}Al .

Following the arguments in Chapter 1, below $E_p = 300$ keV one can estimate the maximum yield of 2164-keV γ rays for an arbitrary resonance. Assuming $\theta^2 = 1$, $l = 0$, and a 50% branch through the 2164-keV state, one can normalize to the known 286-keV resonance yield and produce the dashed curve in Figure 3.6. Apparently, using the current target, beam power, and detector, one would not expect to see resonances below $E_p = 150$ keV.

Three states were known in ^{27}Si which could correspond to proton resonances between the limit of 150 keV and the lowest previously observed resonance at 286 keV. Our attention thus turned to $E_p = 193, 235, \text{ and } 247$ keV. Our sensitivity to the latter two could not be readily improved, but the background at 193 keV was mostly due to boron contamination. The Pt backings contained some boron, but there was also a surface layer having about $10^{15} \text{ }^{11}\text{B}/\text{cm}^2$ ($20 \text{ ng}/\text{cm}^2$) in the target. This boron may have leached from the boro-silicate test tubes during the chemistry, but despite switching to quartz tubes, and distillation of our sample with nitric acid and ethanol (which should remove the boron as ethyl borate (BUR80)) we failed to solve the problem.

Although our sensitivity at low energies was comparable to previous work (which used fifty times the integrated charge), above 290 keV we averaged a thirty-fold improvement. Unobserved resonances below our sensitivity between 0.3 and 1 MeV would not compete significantly with known resonances in determining $\langle\sigma v\rangle$.

As a result of this work, five previously unobserved resonances were identified. Evidence for each is presented in Figure 3.7. We required observation of at least two transitions in ^{27}Si to assure a unique signature. The 770-keV resonance falls between two $^{27}\text{Al}(p, \gamma)^{28}\text{Si}$ resonances at 767 and 774 keV, which presumably obscured it in previous work. The 847-keV resonance is quite weak, but shows up clearly in a window integrating all events above thorium background. The 876-keV resonance falls close to one in fluorine at 872 keV which presumably obscured it previously.

We do not know why 917-keV resonance was missed previously, as it is quite clear in the current work. Finally, the 928- and 929-keV resonances were reported as a single resonance in (BUC84). Closer inspection, though, reveals the leading edge of the 417-keV excitation function due to (p, p') appearing 1.6 keV above the edge in a window on the 2910-keV line. A run with a thinner target (shown in inset) shows the 2910-keV excitation function itself to be double peaked.

The germanium spectra at each of the eleven resonances were analyzed, correcting for summing but assuming $W(\theta) = 1$, and gave the cascade schemes presented in Figure 3.8. (Further details are given in the Appendix.) Table 6.1 presents the deduced resonance strengths and limits on unobserved states.

Resonance energies were determined with respect to well known $^{27}\text{Al}(p, \gamma)^{28}\text{Si}$ resonances (END78). (See, however, comments to Table 6.1.) Using the measured ramp voltage, runs which included the leading edge of an $^{27}\text{Al}(p, \gamma)^{28}\text{Si}$ resonance whose location was known to within ± 0.5 keV gave a relative uncertainty of 0.2 keV, and the combined error is quoted. In runs which did not encompass a suitable reference resonance, energies were determined by a Hall probe in the analyzing magnet, which was calibrated via the known $^{27}\text{Al}(p, \gamma)^{28}\text{Si}$ resonances. Each set of runs between checks of the target deterioration (at $E_p = 992$ keV) was calibrated separately, which enabled resonance energies to be determined to ≤ 0.5 keV. Using the ground state transitions of the 770-, 917-, and 929-keV resonances, correcting for Doppler and recoil shifts, we find the Q-value for $^{26}\text{Al}(p, \gamma)^{27}\text{Si}$ to be 7463.6 ± 1.6 , in good agreement with the value of 7464.9 ± 0.8 keV obtained by Buchmann et al. (BUC84). Combining these with that of (WAP85) (7464.4 ± 1.1) we adopt a Q-value of 7464.6 ± 0.6 keV.

Comparing the resonances which were observed in both this and prior work there are some significant discrepancies in the deduced resonance strengths which are worth noting. Although cascade schemes can frequently differ in detail without

affecting the final strength, major differences certainly play a role and are presented on a case-by-case manner in the Appendix. Here we will focus on those resonances where the quoted uncertainties in the strengths do not overlap.

The 729-keV resonance has a strength double that reported in (BUC84). One of the major cascades from this resonance is through the 2910-keV state, whose transition to the ground state, corrected for the Doppler shift, should appear at 2914 keV. In (BUC83) this line was dominated by the 731-keV resonance in $^{27}\text{Al}(p, \gamma)^{28}\text{Si}$ which has a major branch giving a line at 2915 keV and forced the use of line-shape fitting to extract the peak area. We were able to separate cleanly the two resonances, and avoid this difficulty.

The combined strength of the 928- and 929-keV resonances is twice that of the previously reported single resonance at 927 keV. The spectrum for this resonance found in (BUC83) is dominated by lines from $^{19}\text{F}(p, \alpha\gamma)^{16}\text{O}$ resulting in a background level at 2910 keV fifty times larger than we observed and obscuring a major cascade mode.

The (p, p_2) strength at 929 keV is also twice that reported in (BUC84). A possible explanation arises from the corrections which were necessary with their target due to the 928-keV resonance in $^{25}\text{Mg}(p, \gamma)^{26}\text{Al}$ which has a 5.5% branch to the 417-keV state in ^{26}Al . The yield from this resonance was normalized by the 2070 \rightarrow 417-keV line which sat on the large $^{19}\text{F}(p, \alpha\gamma)^{16}\text{O}$ background. However, the magnitude of this correction is small compared to the discrepancy. The current target contained no observable Mg, and so our larger result cannot arise from the same difficulty. The remaining possible problems are target thickness and detector efficiency.

The two lowest resonances at 286- and 381-keV, which dominate $\langle\sigma v\rangle$ at $T_9 \approx 1$ are in good agreement.

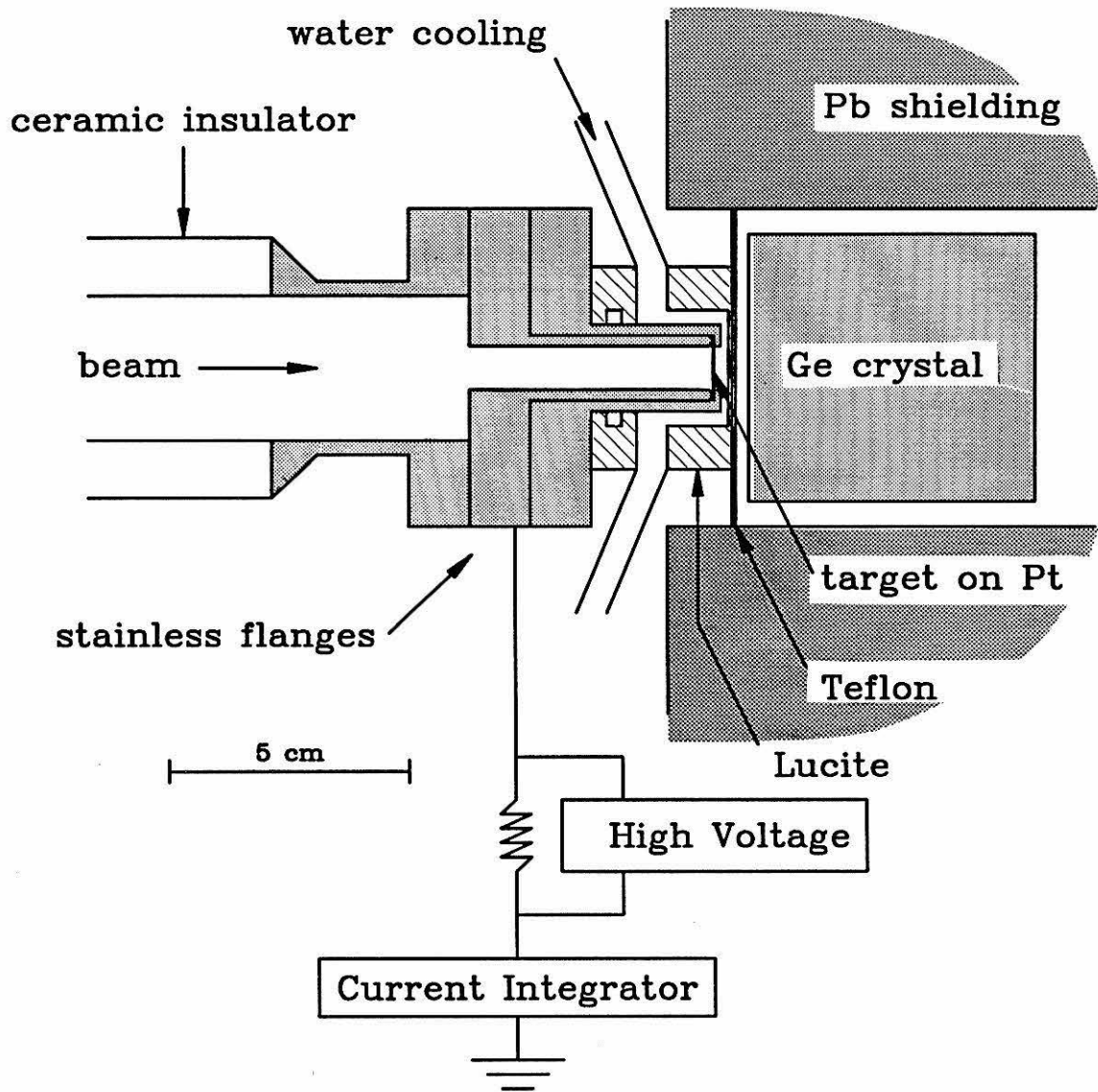


Figure 3.1. Germanium Detector Geometry. Cooling water was gravity fed from an insulated reservoir to prevent leakage currents due to the high voltages used. The capacitance of the system (a few nF), coupled with a kV/s voltage ramp, gave rise to an artificial current of \pm a few μA which made tuning low current beams difficult, but had no net effect on charge integration.

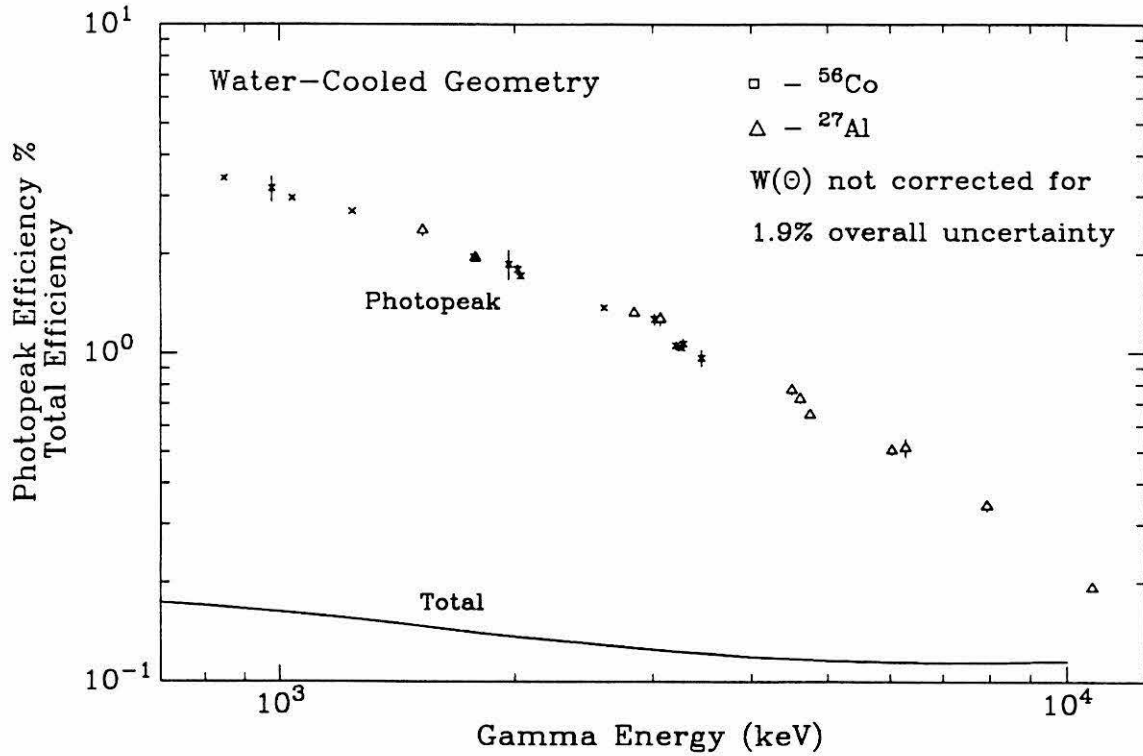
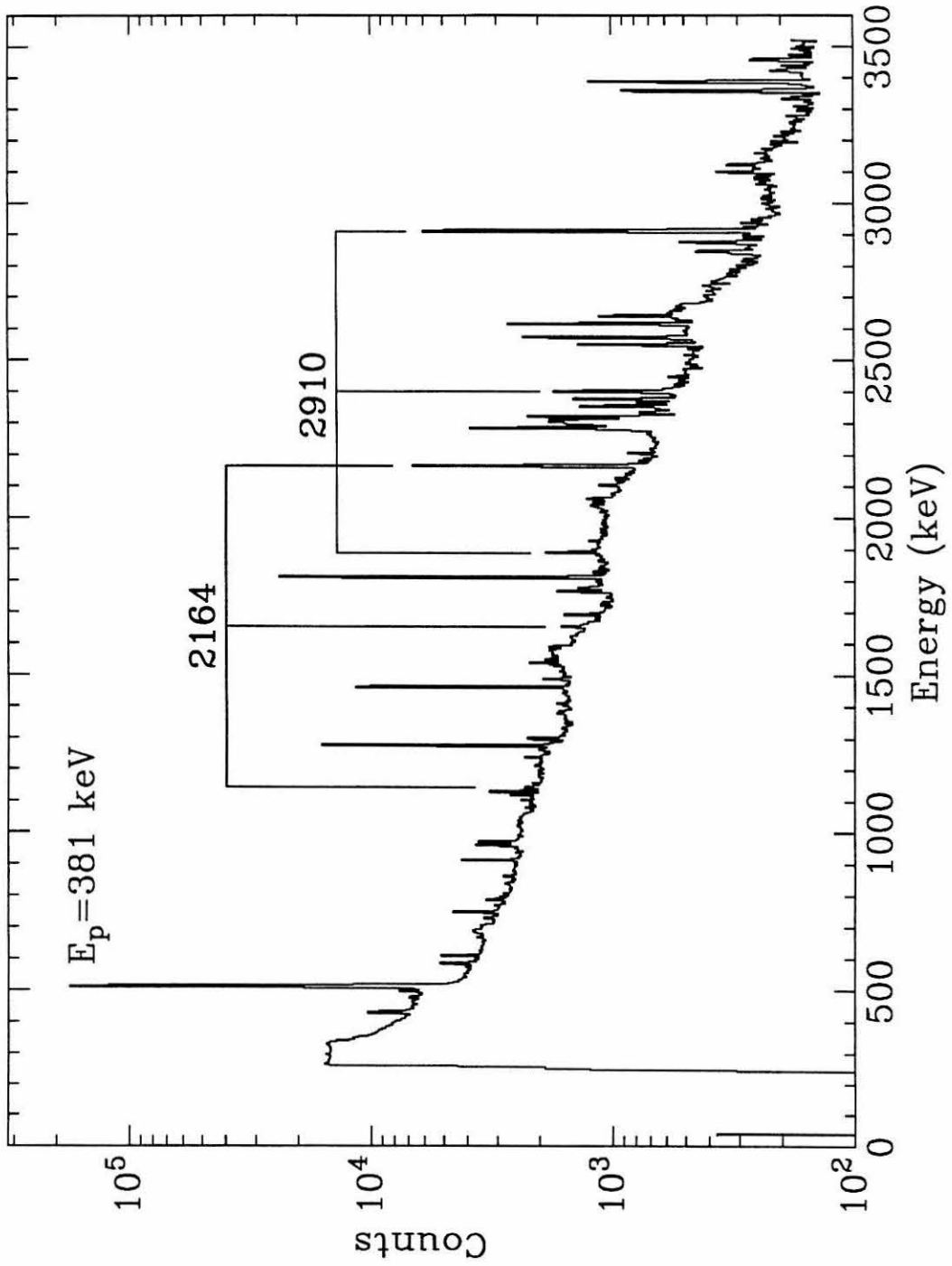


Figure 3.2. HPGe Efficiency. Both the measured photopeak efficiency (%) and calculated total efficiency (fractional) are shown. The latter can be used to estimate the magnitude of summing corrections.

Figure 3.3. Typical Germanium Spectrum. For clarity only two of the major transitions are indicated. For each, the photopeak, first escape peak, and second escape peak, are identified.

Germanium Spectrum



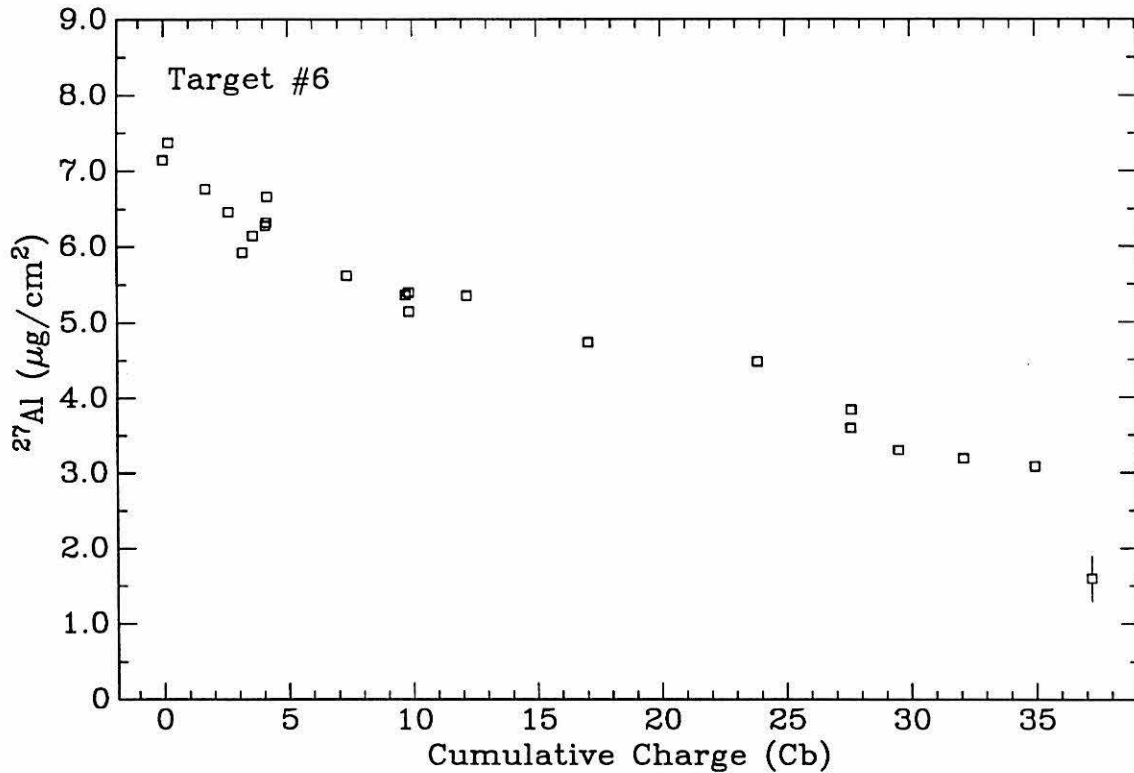


Figure 3.4. Target Deterioration. The amount of ^{27}Al in target #6 was determined by measuring A for the 992-keV resonance in $^{27}\text{Al}(p, \gamma)^{28}\text{Si}$ at frequent intervals. The loss seemed independent of beam power, but grew linearly with cumulative charge. The beam was always brought to a focus upstream from the final collimator so it would be diffuse at the target location. This should average over the variations in target thickness so apparent in figure 2.6. The limited scatter in the above data reflects the success of this approach.

Figure 3.5. Background Excitation Function. The number of events having an energy greater than the room background line at 2614 keV and less than the $E_x \rightarrow 0$ transition for an $^{26}\text{Al}(p, \gamma)^{27}\text{Si}$ reaction is plotted against incident proton energy. Most of the events in this broad window are from Compton electrons. The isotope responsible for each feature was identified by examining the corresponding pulse-height spectrum.

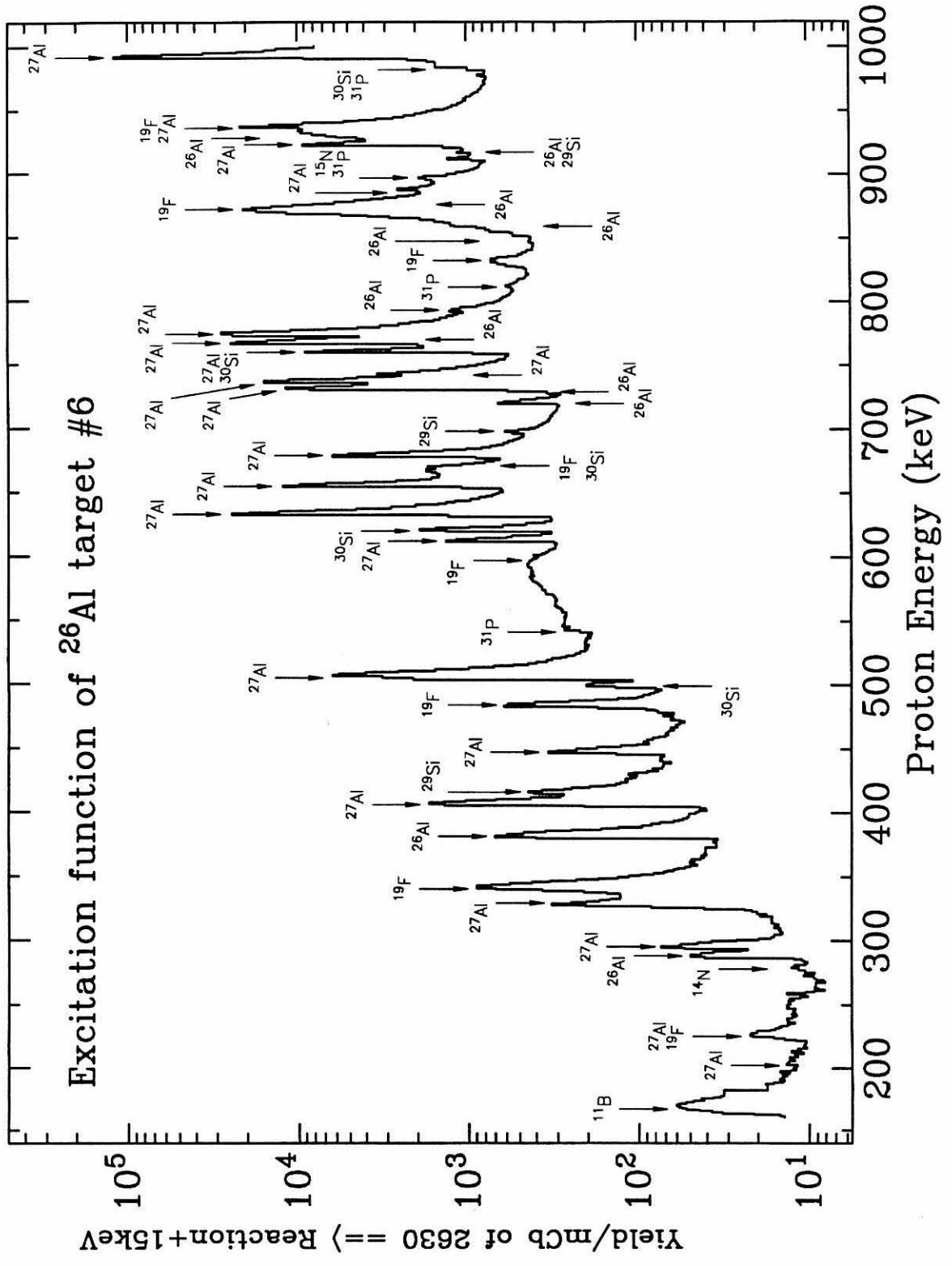


Figure 3.6. 2164-keV Excitation Function. The net 2164-keV photopeak yield is plotted versus proton energy. For clarity we have binned our results into keV steps in regions where no resonance was observed. The solid curve represents the upper limits obtained by Buchmann et al. (BUC84) while the dashed curve indicates the maximum yield a resonance at that energy could be expected to have (obtained by assuming $l = 0$ and $\theta^2 = 1$). Along the upper abscissa there are two sets of arrows. The lower set marks known $^{27}\text{Al}(p, \gamma)^{28}\text{Si}$ resonant energies and the upper set indicates possible $^{26}\text{Al}(p, \gamma)^{27}\text{Si}$ resonant energies based on identified states in ^{27}Si . New resonances are seen at 770, 847, 876, 917, and 928 keV.

$^{26}\text{Al}(p,\gamma)^{27}\text{Si}$

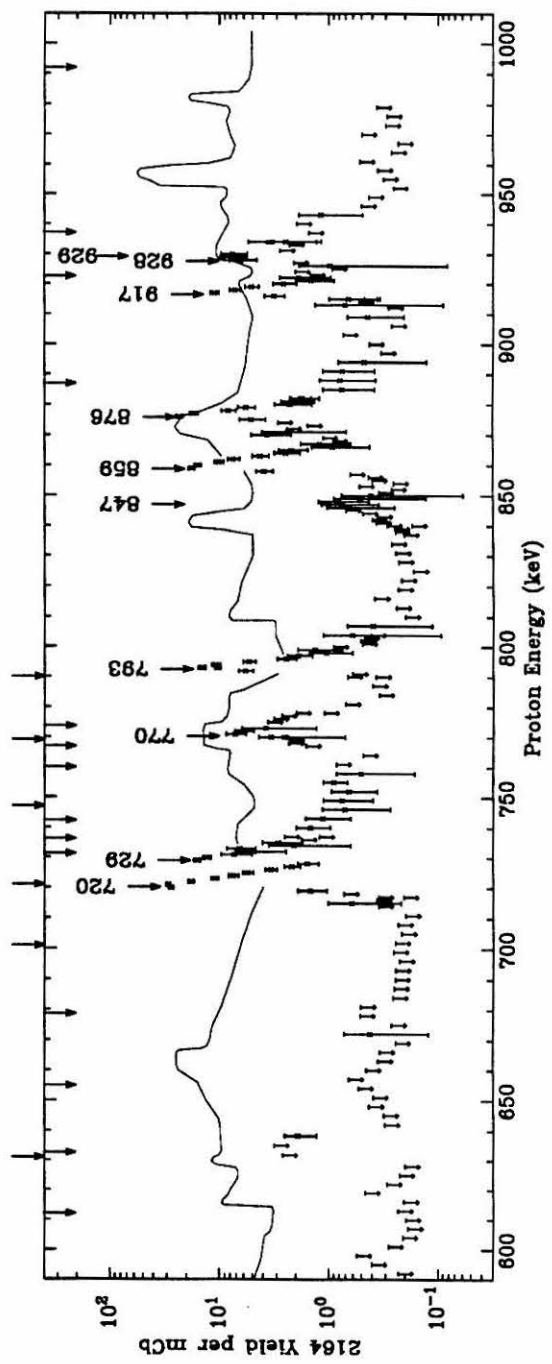
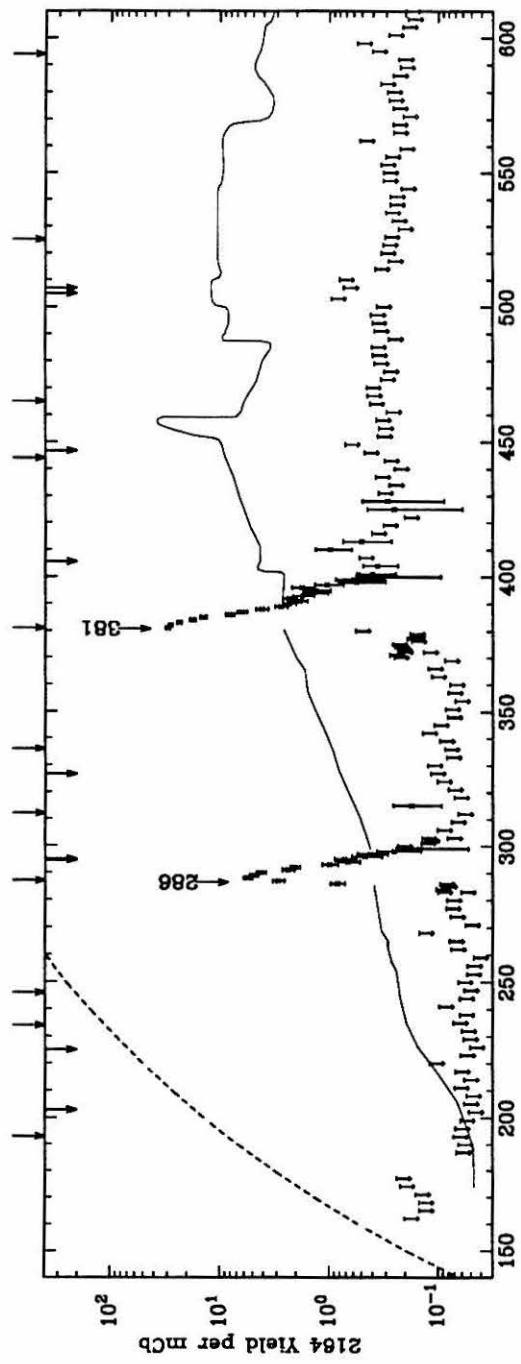
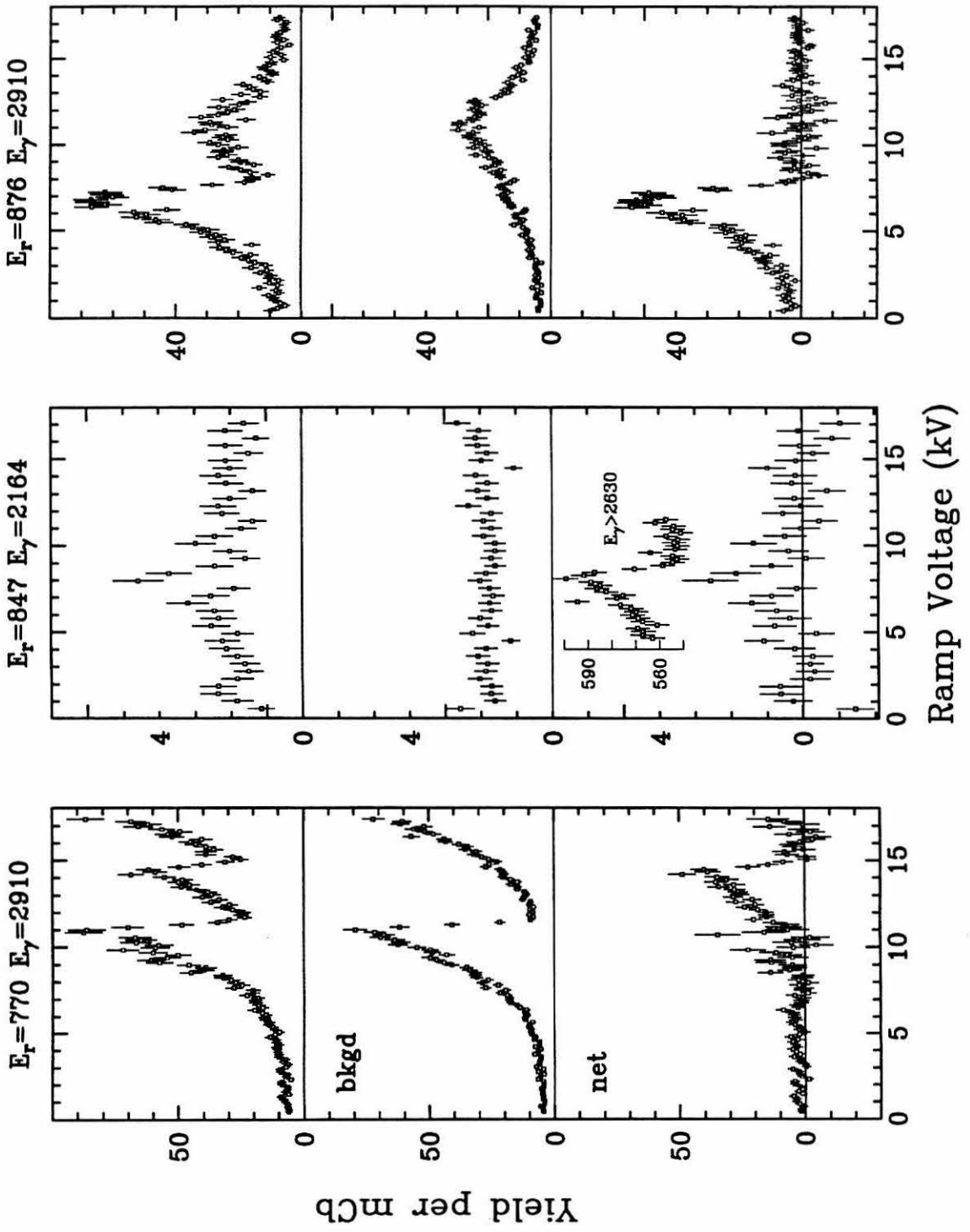


Figure 3.7. New Resonances. Selected windows illustrate each of the new resonances. The top frame presents the excitation function obtained from a window about the γ -ray line indicated. The middle frame presents the excitation function from windows on either side of this line and has been normalized to the same number of channels as in the center window. The bottom frame presents the net excitation function.

The structure in the background reflects the increased Compton yield due to other (p, γ) resonances and is identical to the structure in figure 3.5. The final two panels illustrating the 928- and 929-keV resonances are taken from the same run.



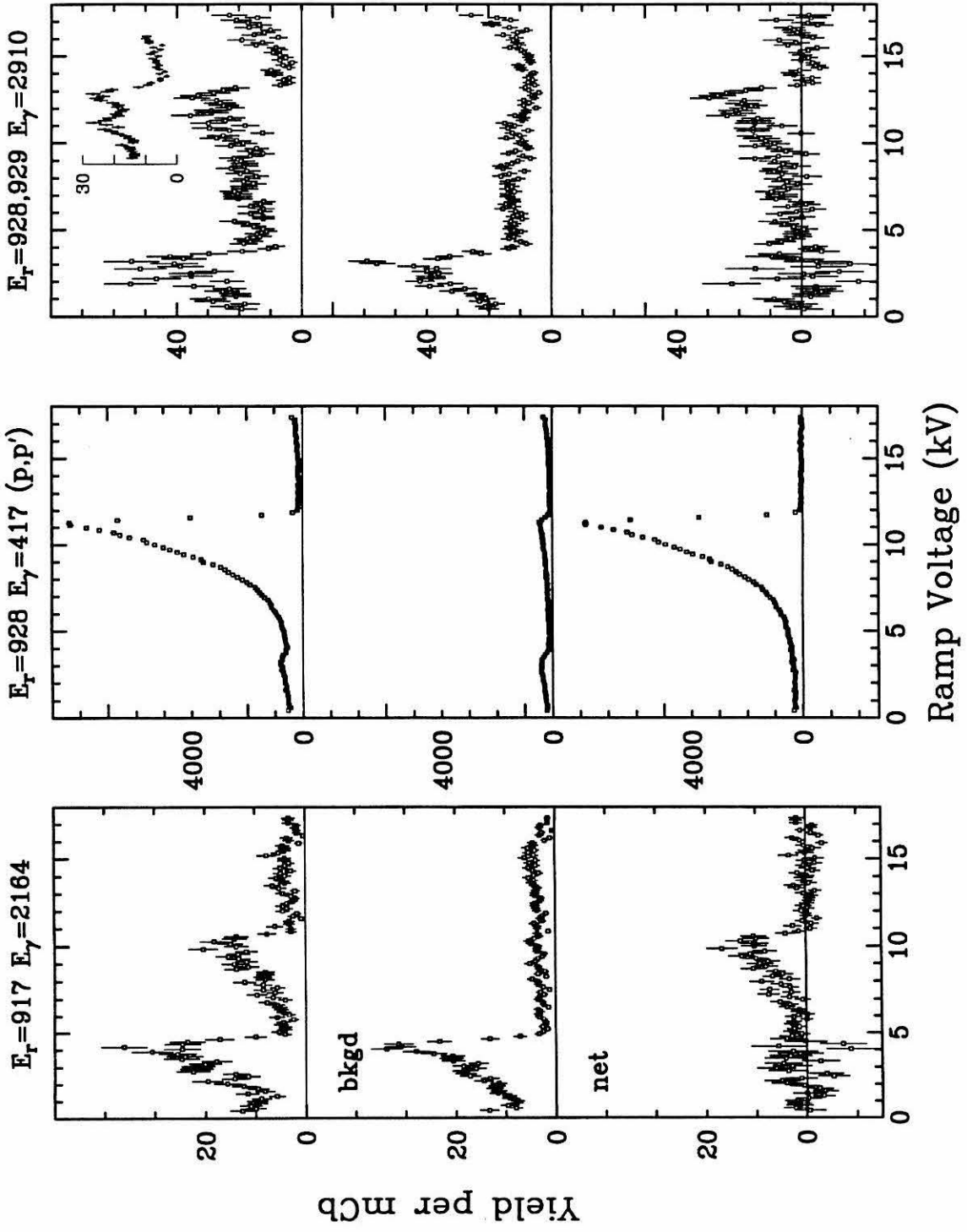
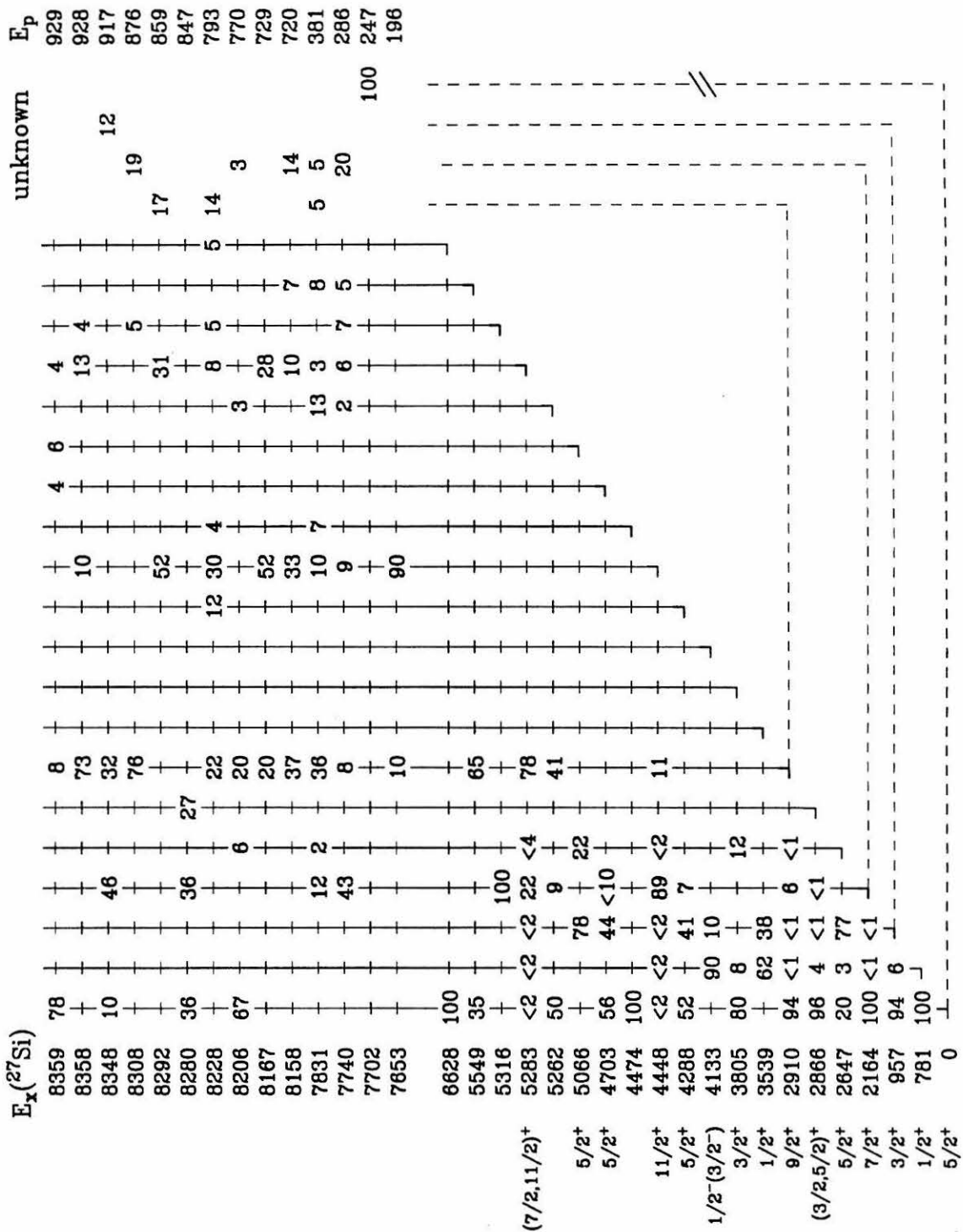


Figure 3.8. Branching Ratios. This figure presents the cascade schemes for each resonance as determined from this work, along with those from (BUC84). Values for the 196- and 247-keV resonances come from Chapter 5. The branching ratios for the 5262-keV state seen in (BUC84) have been adjusted to fit the observed spectra. A new state at 5549 keV has been identified with the branching ratios indicated. The state at 6628 keV has been observed previously in (p, t) (BEN77). See Appendix for estimates of uncertainties. The branching ratios for all the other bound states are taken from (END78).

Wigner limits on the resonance strengths below 400 keV indicate $l_p \leq 2$. This limits the spins of these states to $\frac{7}{2} - \frac{15}{2}$. Further arguments could be made on the basis of Weisskopf transition strengths, but not with any certainty.



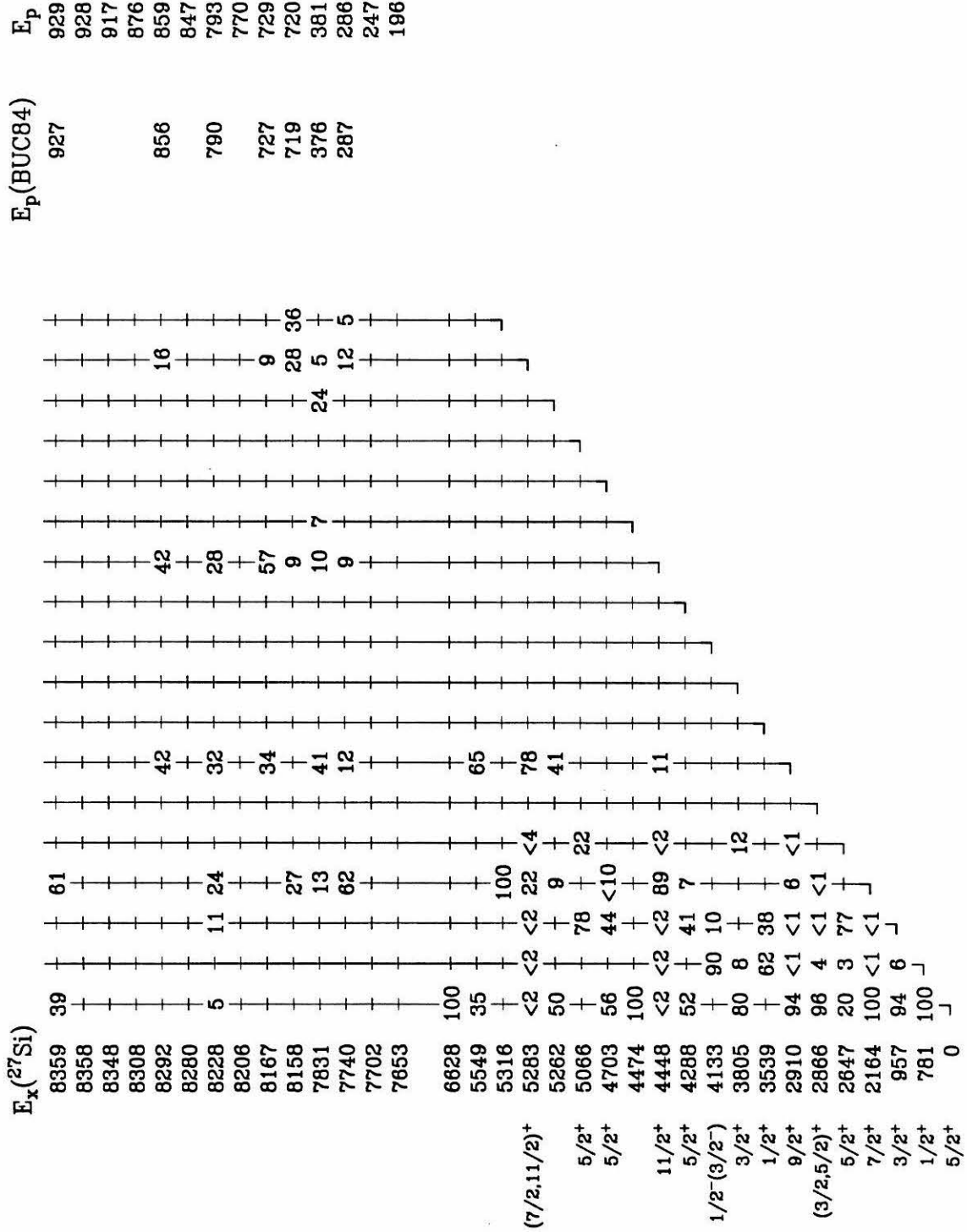


Table 3.1

Observed Elemental Composition of ^{26}Al Target #6

Element	Amount [†]	
	$\mu\text{g}/\text{cm}^2$	(atoms/ cm^2) $\times 10^{15}$
^{26}Al	0.46	10.6 $\pm 10\%$
^{27}Al	7.3	163. $\pm 10\%$
O	7.2	272. $\pm 15\%$
Si	1.6	35.
C	0.3	15. *
B	0.040	2.2
P	0.009	0.2
N	0.006	0.3
Na	0.005	0.1
F	0.001	0.03

† Amounts were determined by (p, γ) reaction yields from known resonances (except for ^{26}Al which was scaled from the ^{27}Al amount). Those having uncertainties indicated are initial amounts. Otherwise, amounts were determined to about 20% from suitable resonances that were scanned during the course of acquiring a complete excitation function from 0.2 to 1.0 MeV.

*Amount varied during course of experiment by about a factor of two.

CHAPTER 4

$^{26}\text{Al}({}^3\text{He}, d)$ using a Q-3D Spectrometer

To determine more information about possible resonances below $E_p \approx 200$ keV, it was necessary to circumvent the Coulomb barrier. The $^{26}\text{Al}({}^3\text{He}, d){}^{27}\text{Si}$ reaction proceeds by direct proton transfer, where the energy of the outgoing deuteron allows an incident ${}^3\text{He}$ energy well above the Coulomb barrier, yet still permits the proton to populate threshold states in ${}^{27}\text{Si}$. The angular distribution of the outgoing deuteron reflects the proton's l -transfer, while its energy identifies the residual ${}^{27}\text{Si}$ state formed. As the flux of each deuteron group is proportional to the proton width of the residual state, we have the basic ingredients to determine Γ_p , i.e., E_r , l , and something proportional to θ^2 . Combining these we have (GOV59)

$$\Gamma_p(E, l) = \left(\frac{3\hbar^2}{2\mu r^2} \right) 2kr P_l(E) C^2 S$$

as before, except θ^2 has been replaced by $C^2 S$ where C^2 is an isospin Clebsch-Gordan coefficient, and S is the spectroscopic strength.

Using the program DWUCK (KUN69), one can determine $C^2 S$ from the measured angular cross section by comparison with DWBA calculations. For $({}^3\text{He}, d)$ on ${}^{26}\text{Al}$ we have

$$\begin{aligned} \frac{d\sigma}{d\Omega}(\text{exp}) &= 4.42 C^2 S \frac{2J+1}{(2J_t+1)(2J_2+1)} \frac{d\sigma}{d\Omega}(\text{DWBA}) \\ &= 4.02 C^2 S \left(\frac{2J+1}{2J_t+1} \right) \frac{d\sigma}{d\Omega}(\text{DWUCK4}) \quad \text{mb/sr,} \end{aligned}$$

where J_t is the transferred spin.

Champagne et al. (CHA83B) argue that the uncertainty arising from the model dependence of the extracted $C^2 S$ can be avoided in special cases by scaling to the $C^2 S$ of known states. If two states, less than about 500 keV apart, are populated by the same partial wave and have fairly large spectroscopic strengths, then if Γ_p

of one is known, it can be used to determine Γ_p for the other. Specifically, one can write $\Gamma_p(E, l) = 2krP_l(E)\gamma_p^2$ while from (MAC60) we have $S = \gamma_p^2/\gamma_{sp}^2$. Champagne et al. then argue that the single-particle width γ_{sp} should be similar for the two states described, giving

$$\omega_1\Gamma_p(E_1, l) = \frac{S_1}{S_2} \frac{k_1P_l(E_1)}{k_2P_l(E_2)} \omega_2\Gamma_p(E_2, l) \frac{2J_1 + 1}{2J_2 + 1}.$$

In any case, it should be possible to determine $\omega\Gamma_p$, which at these low energies is equivalent to $\omega\gamma$. With this motivation we fabricated a transmission target of ^{26}Al suitable for ($^3\text{He}, d$) measurements at the Princeton cyclotron laboratory.

4.1: target considerations

The observed energy spread of a deuteron group comes from beam-energy resolution, detector resolution, straggle in the target, and, for forward angle detection, the difference in stopping powers of ^3He and deuterons. With a 20-MeV ^3He beam from the Princeton AVF Cyclotron, and using their Q-3D (quadrupole-dipole-dipole-dipole) spectrometer (KOU74) to detect the deuterons, it was straggle in the target which limited the maximum thickness possible. Aiming for a resolution of 10 keV, we fabricated an Al_2O_3 target supported by carbon foil as described in Chapter 2. The total target had about $55 \mu\text{g}/\text{cm}^2$ but only 1% of that was ^{26}Al .

4.2: experimental setup

The combination of a cyclotron and a Q-3D spectrometer made the Princeton facility attractive. Their cyclotron beam can usually be dispersion-matched to the Q-3D spectrometer, allowing a particle group to have a single image point despite small variations in the incident beam energy, provided these variations are correlated with a transverse object location. This feature allows a superior resolution compared with other facilities. Figure 4.1 shows the physical layout of the equipment. The focal-plane detector consisted of a thin, position-sensitive, gas proportional counter

(ΔE), followed by a thick scintillation detector ($E - \Delta E$). A graph of E versus ΔE allowed identification of the outgoing particles (Figure 4.2), while focal-plane position determined their momentum.

The spectrum range of the Q-3D using the 60-cm focal-plane detector was $E_{max}/E_{min} = 1.08$, which allowed us to study states in ^{27}Si between about 7.25 and 8.25 MeV. The deuteron-energy calibration and absolute yields were determined from “background” particle groups, corresponding to known states in ^{28}Si (CHA86a) having $E_x \approx 12$ MeV (from ($^3\text{He}, d$) reactions on the ^{27}Al in the target). Runs were taken at $\theta_{lab} = 0, 5, 10, 13, 15, 17.5, 20,$ and 30 degrees.

4.3: analysis

The deuteron spectra typically had about 12-keV resolution; a representative run at $\theta_{lab} = 5^\circ$ is presented in Figure 4.3. The spectrum is clearly dominated by $^{27}\text{Al}(^3\text{He}, d)^{28}\text{Si}$ reactions, as well as by reactions on ^{12}C , ^{16}O , and ^{14}N —the latter perhaps coming from ammonia in the copper etch. In anticipation of this problem, we had produced a reference target, made in an identical fashion except for the lack of ^{26}Al . By comparison, excess yields from the ^{26}Al target were identified, corresponding to the 7653- and 7740-keV states in ^{27}Si . Additionally, at several angles the region corresponding to the 7589-keV state was clear of background, so an upper limit on its proton width could be set. Because of the large background elsewhere, no new information could be obtained for other states in ^{27}Si .

Analysis of these three states—7589, 7653 and 7740—was done both by direct subtraction and line-shape fitting. Figure 4.4 provides an example of each approach. Subtraction was accomplished by normalizing the yields at isolated strong peaks from ^{27}Al in each target, calibrating the abscissa, and then subtracting. Absolute cross sections were then obtained from the $^{26}\text{Al}/^{27}\text{Al}$ ratio and the known ^{27}Al cross sections. This straight-forward approach assumed similar contaminants in the targets and that the line shapes did not vary between runs. Both assumptions proved

reasonably justified, and the locations of the residual peaks at various angles were consistent with the kinematics expected from a mass 26 target.

To avoid having to make the above assumptions, we attempted to fit the spectra using the versatile fitting program NUFIT (JAM86). To extract the 7740-keV particle group, the region fitted included the $E_x = 11870$ - and 11901-keV particle groups from $^{27}\text{Al}(^3\text{He}, d)^{28}\text{Si}$ (hereafter called ^{28}Si groups), while the 7653-keV fitted region included the 11780- and 11801-keV ^{28}Si groups. We developed the following procedure aimed at reducing systematic errors. Isolated ^{28}Si particle groups within a spectrum were used to define a single "Si" line shape. Lines from nuclei with different mass had distorted shapes because of their different $dE/d\theta$. Initial shapes for these groups came from the reference-target fit, which was constrained to give the known relative strengths of the ^{28}Si groups. Yields of identified background groups from each target were then forced to be in the same ratio for all fits. Remaining parameters, including a linear background, were then varied to minimize χ^2 .

The particle-group centroids returned by this procedure are presented in Figure 4.5. Centroids of the 11780- and 11901-keV ^{28}Si groups were used as calibration points, and then the difference of each centroid from that of the 11901-keV level was plotted against exit angle. The curves were calculated using simple kinematic relations and known level spacings. The background ^{15}O group, whose line shape changed drastically with angle, appears to have been handled successfully based on the kinematic shift of its centroid. More significantly, the two peaks of interest are indeed consistent with a mass 26 target. At some angles fitting became impractical because of background peaks which moved into the region. (The fit centroid of the 7653-keV group at 5 degrees reflects the limitations of this analysis; however, the centroid of this peak obtained by direct subtraction is consistent with a mass 26 target.)

With these groups thus assigned to $^{26}\text{Al}(^3\text{He}, d)^{27}\text{Si}$ reactions, their angular distributions were analyzed. Results of the subtraction and fitting analyses were combined by taking weighted averages for the cross sections and combining the errors using the method of Wohl et al. (WOH84). Figure 4.6 shows the complete data set, including DWBA fits using potential parameters appropriate to this mass and energy region (Table 4.1). The data would not allow definite extraction of the l -transfers, although some pure l -transfers could be ruled out. This prevented use of the scaling arguments given by Champagne et al. For the 7589-keV group, which was never observed, an upper limit assuming $l = 0$ was established. Table 4.2 tabulates the expected strength of each resonance under various assumptions for the l -transfer.

Although the goal of determining l_p and C^2S for all the ^{27}Si states of interest was not achieved because of target background, what *was* determined still impacts $\langle\sigma v\rangle$. The 7589-keV state in ^{28}Si , which Wang et al. (WAN89) suggested as a possible $l = 0$ proton resonance in $^{27}\text{Al}(p, \gamma)^{28}\text{Si}$ at $E_p = 130$ keV, is at least 200 times weaker than the previous limit of $\theta^2 = 1$. Also, the $E_p = 196$ -keV resonance was shown to have a reduced width of order unity, which coupled with a maximum l -transfer of 3 (estimated from Figure 4.6), raises the experimental limit on $\langle\sigma v\rangle$ at low temperatures.

The importance of a proton resonance at 196 keV prompted further experiments to determine the spin of the 7653-keV state in ^{27}Si and so determine the proton's l -transfer and consequent Coulomb-barrier penetration factor. Using a self-supporting ^{28}Si target, the $^{28}\text{Si}(^3\text{He}, \alpha\gamma)^{27}\text{Si}$ coincidence measurement was attempted. Gating on the alpha group corresponding to populating the 7653-keV state in ^{27}Si identifies that state's de-excitation γ rays in a suitable detector. The combination of a 0^+ target, $\frac{1}{2}^+$ beam, and 0^+ outgoing particle, means that alphas emitted at 0° correspond to aligned ^{28}Si states having magnetic substates $\pm\frac{1}{2}$. The

angular distribution of their decay radiation might then identify the state's spin. Unfortunately, the small cross section, coupled with a large beam-induced background not only made measuring such angular distributions impossible, but even prevented identification of any ^{27}Si transitions, and the experiment was abandoned.

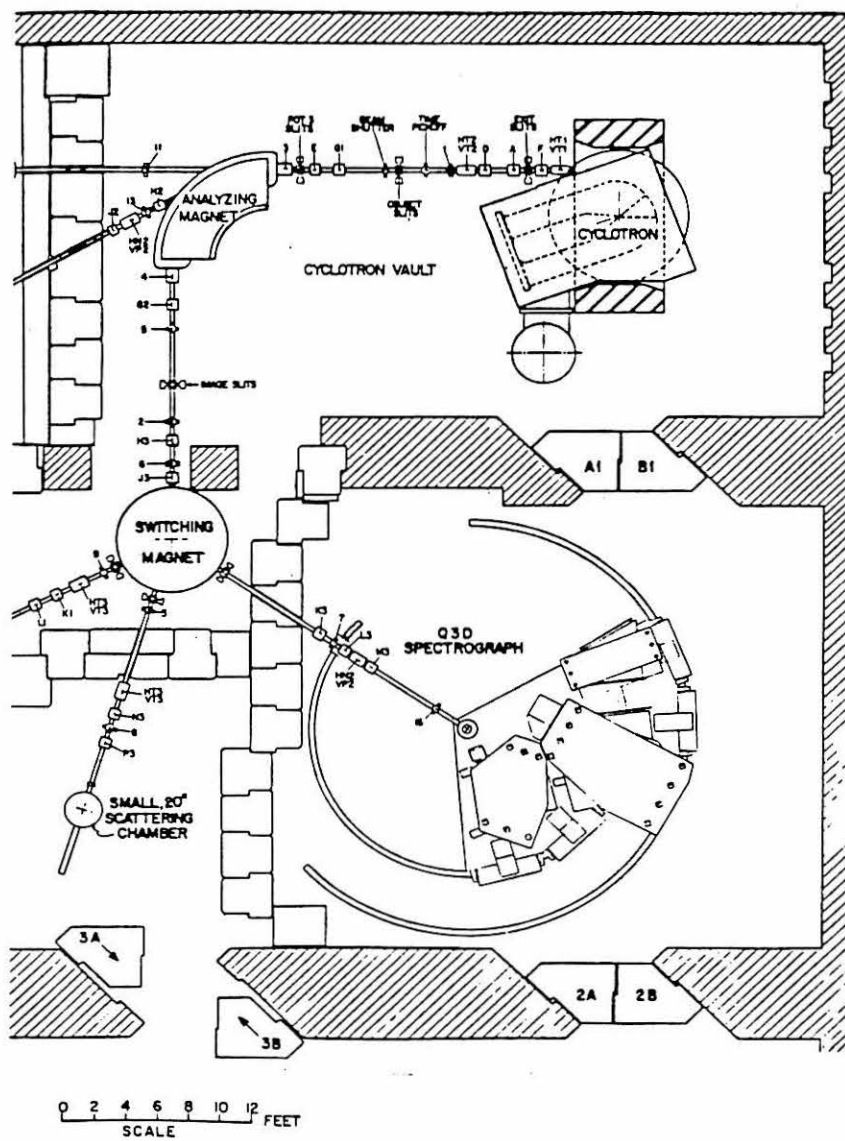


Figure 4.1. Princeton AVF Cyclotron Facility.

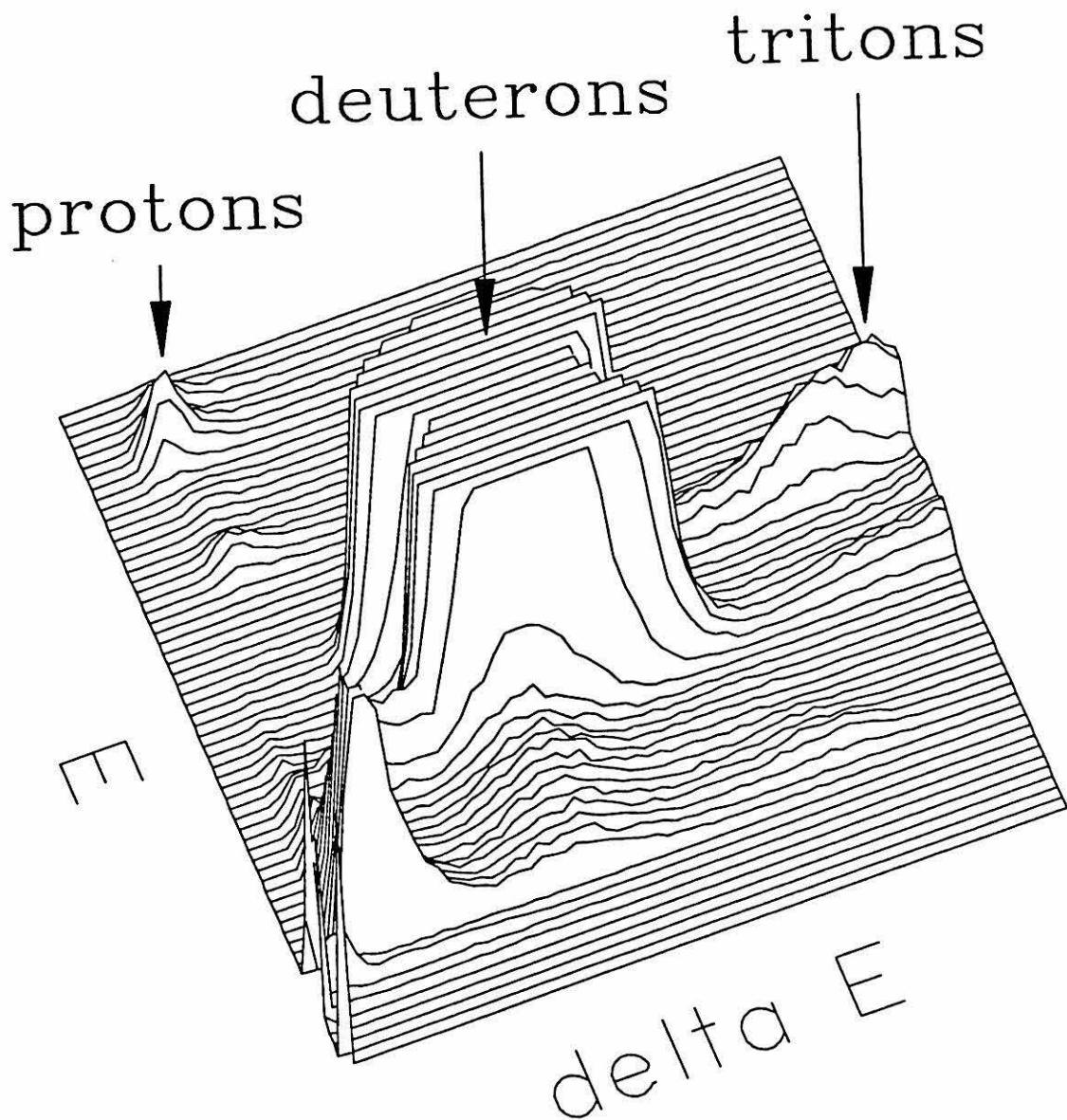


Figure 4.2. Particle Identification. The deuteron peak is resolved from other particles and has been truncated for clarity. The two major lobes arise from deuterons corresponding to $({}^3\text{He}, d)$ reactions on ${}^{12}\text{C}$ and ${}^{16}\text{O}$ creating ${}^{13}\text{N}^*$ and ${}^{17}\text{F}^*$, respectively.

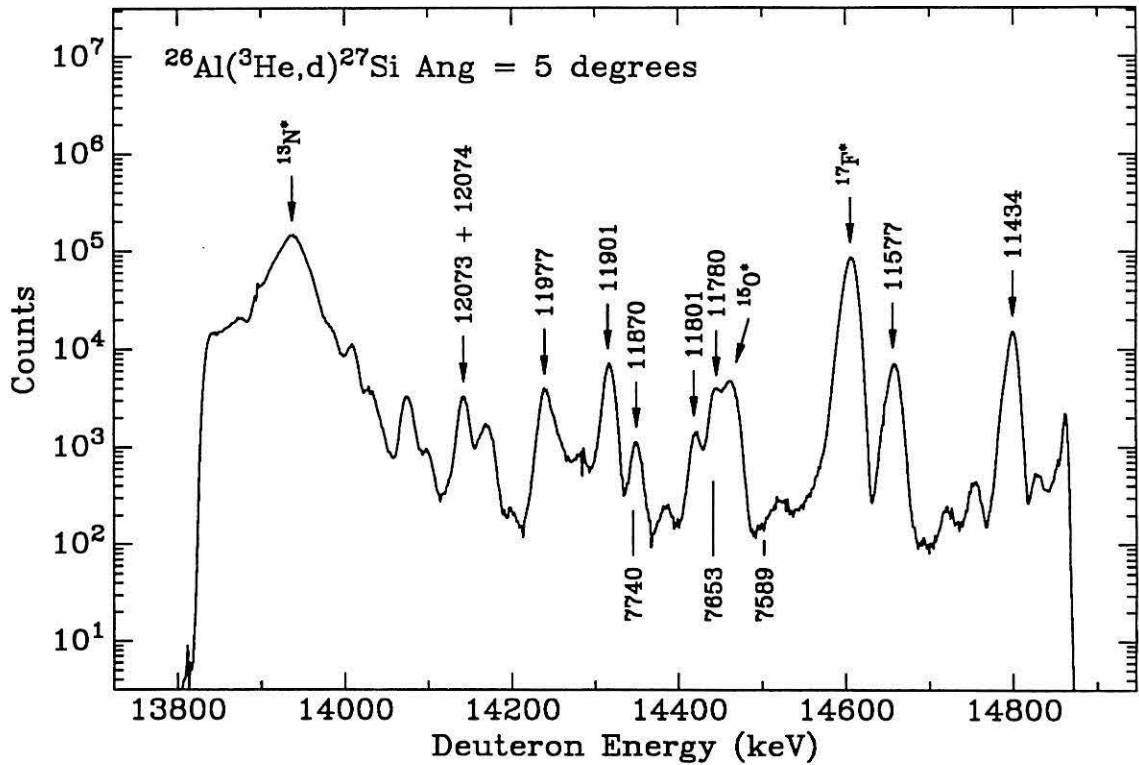
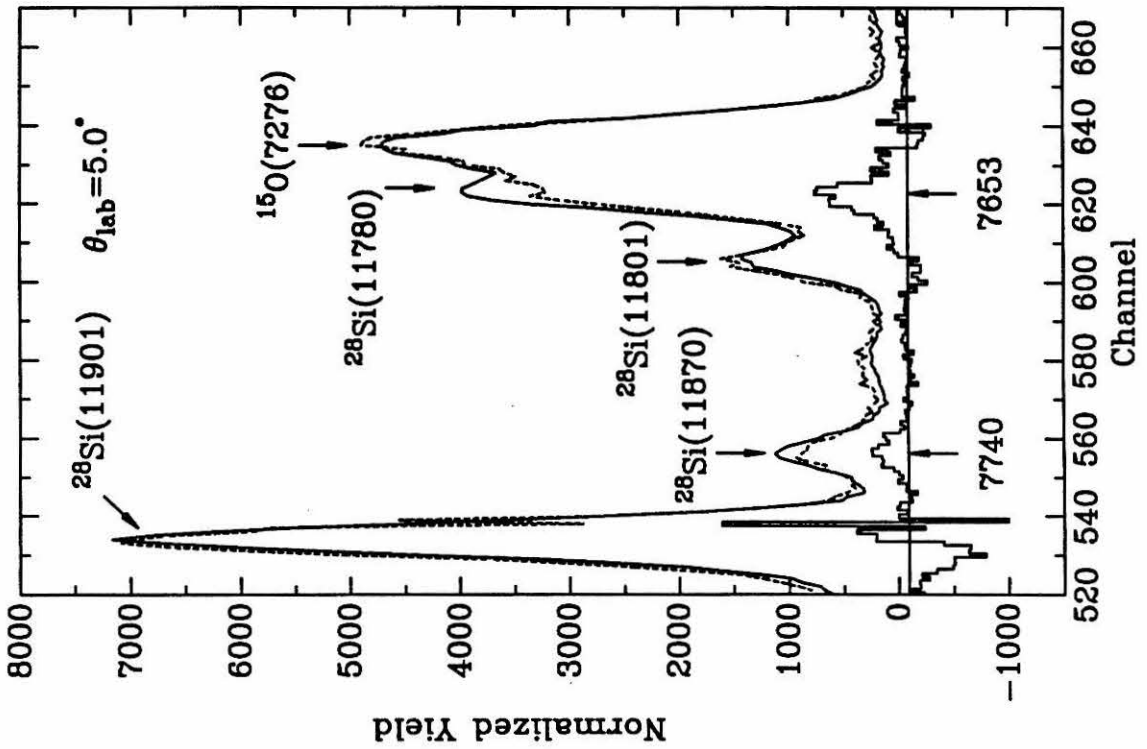
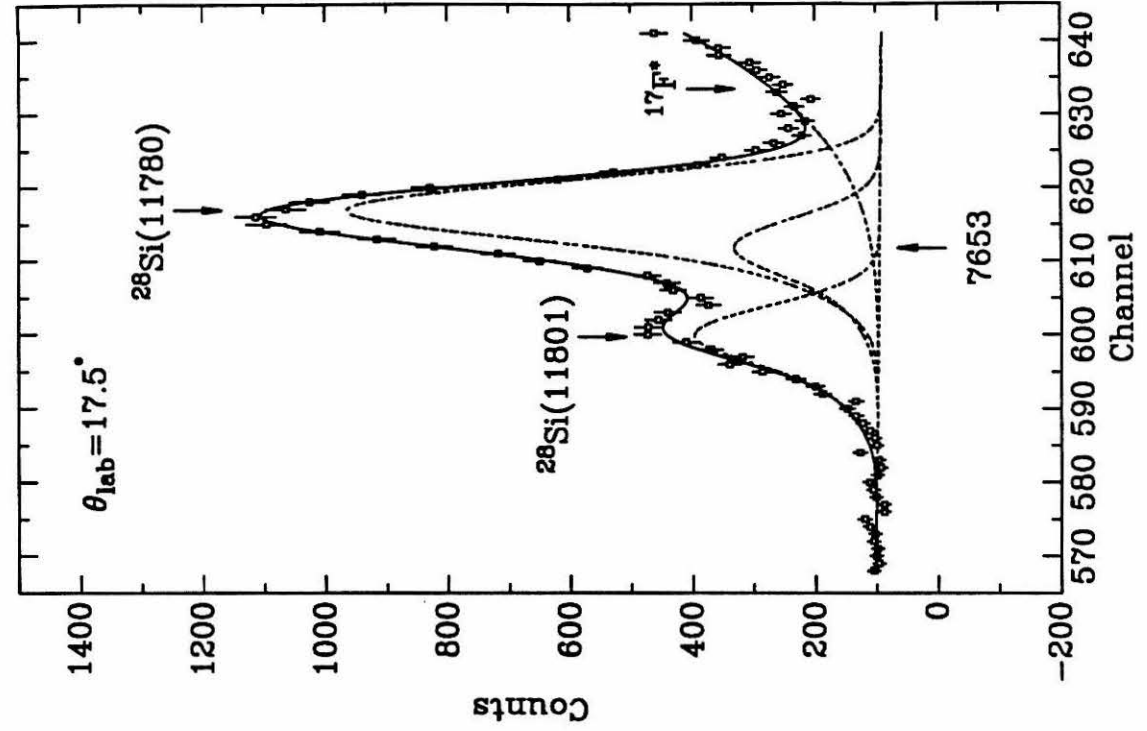


Figure 4.3. Deuteron Spectrum at $\theta_{\text{lab}} = 5^\circ$. Groups are identified by the excited states of the recoiling nucleus. Those from ^{28}Si states are labeled above the curve, while those from ^{27}Si states are labeled below. The excesses are not readily visible on this scale.

Figure 4.4. Subtraction and Fitting Analyses.
The two procedures described in the text are illustrated. Notice the difference in line shape between the Si and F groups. Residual groups attributed to ^{27}Si are labeled below the curves.



Kinematic Shifts

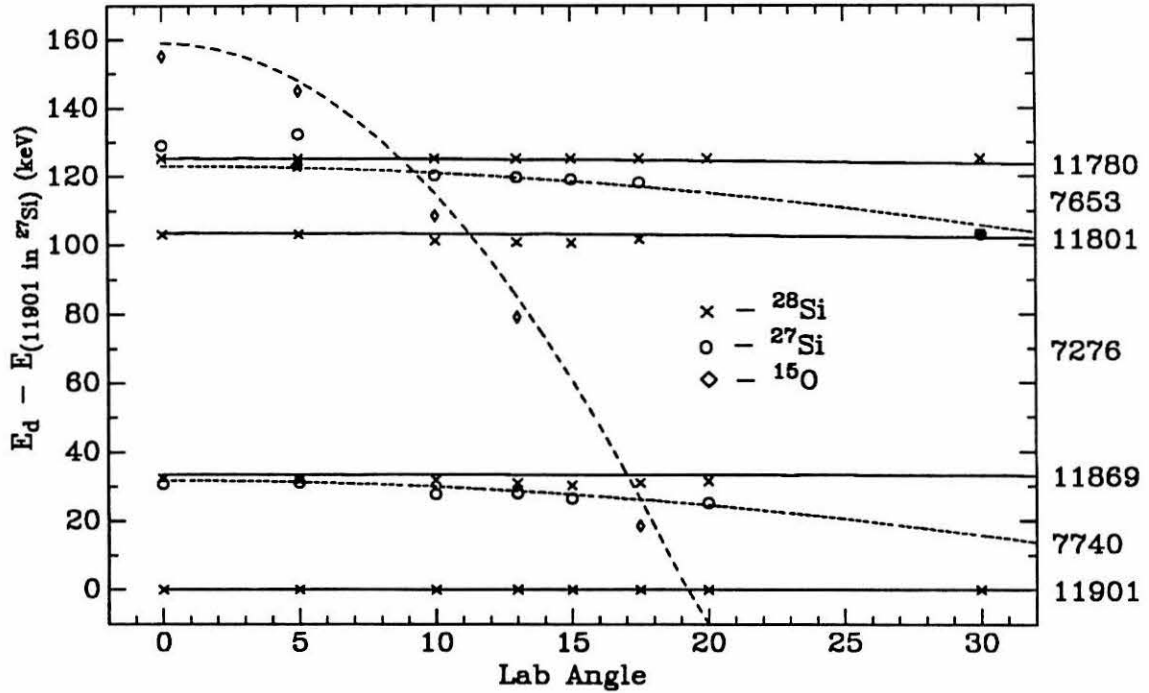


Figure 4.5. Kinematic Identification. The kinematic energy change of a deuteron group with angle is related to the target mass. This dependence is shown for the seven groups being fit, assuming they have been correctly identified. Actual observations are indicated and confirm that the 7740- and 7654-keV groups come from a mass 26 target.

Figure 4.6. Angular Distributions and DWBA Fits. Angular distributions for the 7589-, 7653-, and 7740-keV deuteron groups are presented along with DWBA fits for a variety of l -transfers. At each angle the fit result (left) and subtraction result (right) were combined to give the datum used. One sigma limits are indicated for the 7589-keV group.

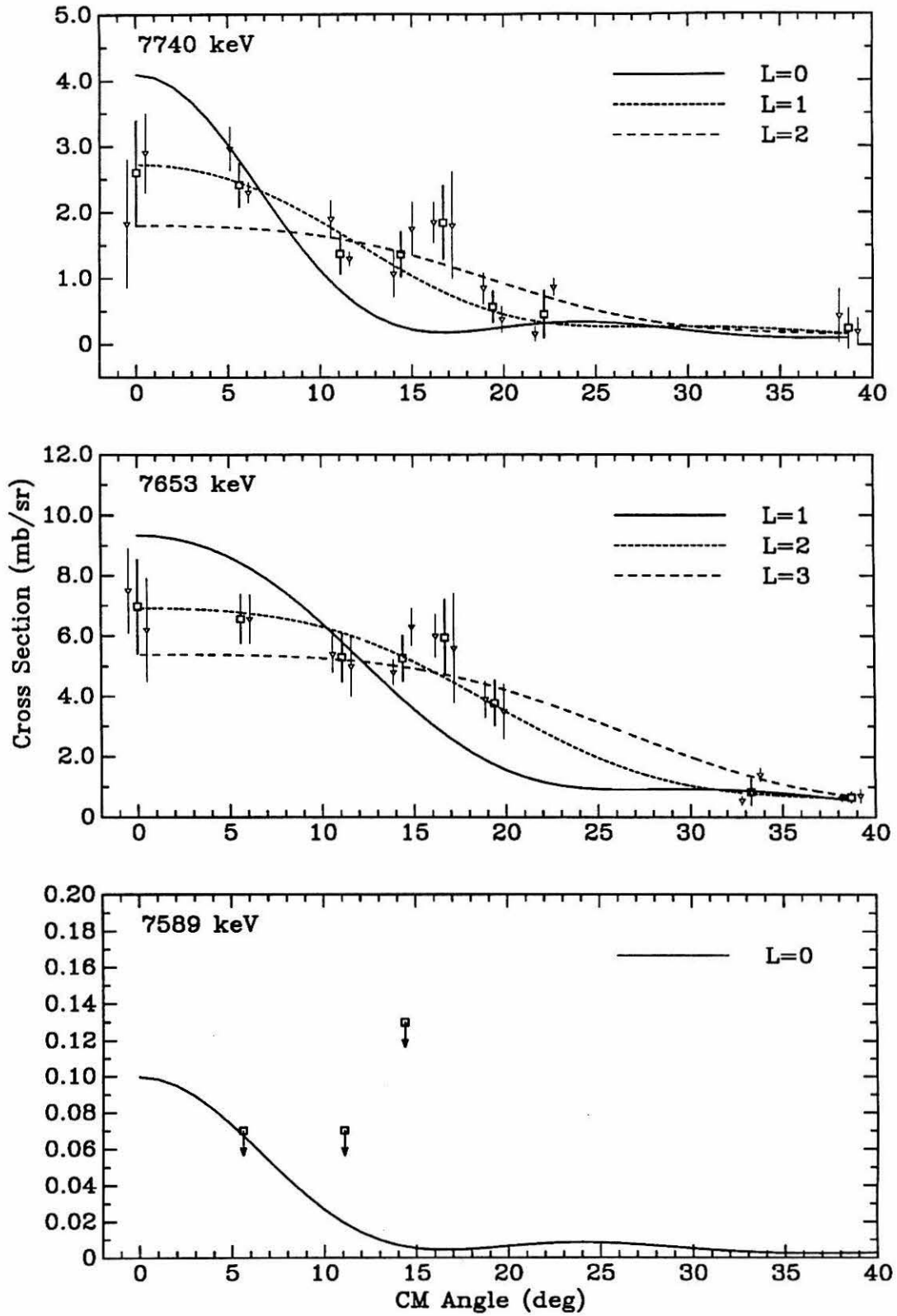


Table 4.1

DWBA Parameters[†]

Channel	V (MeV)	r (fm)	a (fm)	W (MeV)	W' (MeV)	r' (fm)	a' (fm)	$V_{s.o.}$ (MeV)	r_c (fm)
$^{26}\text{Al} + ^3\text{He}$	159.3	1.149	0.683	17.86		1.567	0.878		1.25
$^{27}\text{Si} + d$	39	1.3	0.883		89	1.48	0.535		1.3
$^{26}\text{Al} + p$	varied [†]	1.25	.65					$\lambda = 25$	1.25

[‡] (CHA86a, PER76)

[†] Adjusted to give 10-keV binding.

Table 4.2

DWBA Fits

E_p (keV)	$E_x(^{27}\text{Si})$ (keV)	l	$2J_t + 1$	N	$(2J + 1)S$	P_l	$\omega\gamma$ (meV)
286	7740	0	2	2.8	1.4	5.99(-7)	120
		1	4	0.9	0.9	1.36(-7)	18
		2	4	1.9	1.9	8.61(-7)	2.3
196	7653	0	2	7.4	3.7	4.71(-9)	2.1
		1	4	2.9	2.9	1.03(-9)	0.35
		2	4	6.9	5.0	6.03(-11)	0.036
		3	8	4.2	8.4	1.23(-12)	0.0012
130	7589	0	2	0.06	0.03	7.98(-12)	$< 2.3 \times 10^{-5}$

For brevity N is defined by $\frac{d\sigma}{d\Omega}(\text{exp}) = N \frac{d\sigma}{d\Omega}(\text{DWUCK4})$. Since J_t is not uniquely determined by l , we have chosen $2s_{1/2}$, $2p_{3/2}$, $1d_{3/2}$, and $1f_{7/2}$. The resulting uncertainty is small compared to the final uncertainties in $\omega\gamma$. Values in parentheses are to be read as 10 raised to that power.

CHAPTER 5

 $^{26}\text{Al}(p, \gamma)$ with a NaI Detector

The predicted $E_p = 196\text{-keV}$ resonance strength obtained from the ($^3\text{He}, d$) work was $\omega\gamma = 0.04\text{ meV}$ if one assumed $l_p = 2$. This was tantalizingly close to the 0.1 meV limit set using the germanium detector: a slight improvement in sensitivity might permit a *direct* measurement using (p, γ).

5.1: experimental setup

The availability in Kellogg Radiation Lab of four large sodium-iodide crystals prompted the consideration of a high-efficiency, albeit low-resolution, γ -ray detector. Three advantages over a germanium detector are quickly recognized. First is the increase in efficiency from a few percent to order unity. Second, arranged as a 4π calorimeter, all events should appear in the full-energy peak corresponding to the entrance E_x , independent of cascading scheme. Events of interest will sum well above target activity and room background. This feature also sums the troublesome boron background events to 16 MeV , well above the 7.7 MeV expected from $^{26}\text{Al}(p, \gamma)^{27}\text{Si}$. Third, such a geometry should be insensitive to angular distributions.

Substantially reduced resolution, however, compromises these advantages. This, and the realization of less than 100% efficiency, means that at higher beam energies where many background resonances have significant yield (Figure 3.3), the possibility of extracting identifiable lines becomes questionable. However, the lowest states of interest, in particular the state at $E_p = 196\text{ keV}$, are well suited to this approach.

Such a detector was assembled as illustrated in Figure 5.1. The four $6 \times 6 \times 10$ -inch crystals were packed in a tight array leaving a one-inch square channel down the center into which the target chamber slid as the detector was rolled forward.

Natural activity of the target ($\approx 90\text{ disint/sec}$), background events from the room, ^{22}Na beamline contamination from a prior unrelated experiment, and cosmic

rays, necessitated some background rejection in order to reduce the event rate to the computer. A two-inch-thick Pb enclosure was erected and this, in addition to electronics thresholds requiring either a single detector to have more than 2.7 MeV deposited, or two detectors to have more than 200 keV each, reduced the ^{22}Na and room backgrounds sufficiently. Standard plastic paddles were used to veto cosmic rays with about 90% efficiency. Nothing, though, could be done to reject the actual target activity without also rejecting valid events which did not deposit their full energy. A schematic of the front-end electronics is provided in Figure 5.2.

Unfortunately, the background still contained a shelf out to 7 MeV which was attributed to neutrons capturing on iodine as was verified with an Am-Be neutron source. To reduce this, a large paraffin house was constructed, achieving a 50% reduction. The remaining yield was attributed to high-energy neutrons related to cosmic rays, and was difficult to shield against. Ultimately, the background at the 196-keV resonance was still dominated by boron contamination, making further room background reductions less significant.

With these provisions, background events were reduced to a rate of ≈ 90 Hz and of these, only those which summed above the decay energy of ^{26}Al were recorded in event mode, having a rate of ≈ 3 Hz. For each event we recorded the energy deposited per detector (four 1K spectra) and a ramp-voltage tag (256 channel). Programming was developed for high-density event-mode recording to accommodate the large files expected. During the runs, two spectra of ramp voltage versus the total energy deposited were collected. One of these, though, required that at least one set of diagonally opposing detectors have more than 700 keV deposited in each. This latter spectrum was expected to have a better signal-to-noise ratio, as was indeed the case.

The target chamber was specially designed to accommodate existing targets, provide water cooling, hold high voltage, and minimize material. Any γ -ray interaction not in the NaI crystals removes that event from the full-energy peak in the detector, making identification harder.

At the energies and currents desired, it was necessary to run with H_2^+ beams due to better machine optics at higher terminal potentials. During preliminary tests, the detector was determined to have $\approx 100\%$ efficiency for detecting low-energy neutrons. The natural abundance of ^2H in hydrogen gives a small, contaminant, deuteron beam of twice the proton energy because of its similar rigidity, resulting in substantial (d,n) yield. These neutrons gave beam-induced background out to 7 MeV, forcing the use of deuterium-depleted hydrogen as the source gas.

5.2: preliminary runs

Preliminary runs using pure Al targets and the $^{27}\text{Al}(p, \gamma)^{28}\text{Si}$ reaction indicated an achievable sensitivity of $\omega\gamma \approx 1 \mu\text{eV}$ at $E_p = 203 \text{ keV}$. Scaling by the stoichiometry of the current ^{26}Al targets, this meant we could detect a 0.064 meV resonance in $^{26}\text{Al}(p, \gamma)^{27}\text{Si}$ if there were no other background. Requiring various coincidences between two detectors above annihilation radiation—in effect looking for cascades—enhances this sensitivity by about a factor of ten, at the cost of becoming dependent on branching ratios and angular correlations.

It was decided to use the $E_p = 406\text{-keV}$ resonance in $^{27}\text{Al}(p, \gamma)^{28}\text{Si}$ for normalization, since the resonance is isolated, of known strength, and requires a minimum of retuning to reach—simply switch to an H^+ beam. Higher-lying resonances, though better known, have excessive yields for reasonably low beam currents. The ability to identify a particular reaction through its Q-value is demonstrated by a run whose range of beam energy, due to the voltage ramp, included several resonances (Figure 5.3).

5.3: efficiency

In order to determine the efficiency, several known resonances in the $^{27}\text{Al}(p, \gamma)^{28}\text{Si}$ and $^{18}\text{O}(p, \gamma)^{19}\text{F}$ reactions were measured. In addition, a calibrated ^{24}Na source was used. All measurements were performed in an identical geometry and the results are presented in Figure 5.4. The term SUM refers to the total energy deposited in all four detectors and the solid curve indicates the integrated yield of events with SUM falling between the abscissa value and E_x for that reaction. The ordinate has been normalized to the expected yield from the known resonance or source strength. (An ideal detector would give a step function falling from 100 – 0% at E_x as the lower limit was raised from zero.) The major cascade multiplicities are indicated, showing the correlation between efficiency and decay scheme. For the resonances shown, a window from $0.9 E_x$ to $1.1 E_x$ has an efficiency varying from 20% to 50%—distressingly low numbers for such a wide window.

The basic simplicity of the geometry, and the well known interactions of radiation in this energy domain, encouraged us to Monte-Carlo the detector response in an effort to understand and perhaps predict these efficiency curves. Accordingly, code was written to model the detector geometry suitable for use with the *Electron Gamma Shower* (EGS4) code obtained from Stanford (NEL85). To accurately predict the observed curves it was necessary to include details of the geometry including the detector’s stainless steel jackets, the reflective material surrounding the crystals, and details of the target chamber. The resulting simulations using known decay schemes agree remarkably well with observed features and are within experimental uncertainties. Based on this success, absolute efficiencies were taken from EGS4 simulations.

5.4: data runs

The runs presented here were taken on ^{26}Al target #5, though the first runs were on target #6. The run sequence included normalizations of target thickness,

rechecking the lowest known (p, γ) resonances, and searches for the $E_x = 7653$ -keV state observed in $^{26}\text{Al}(^3\text{He}, d)^{27}\text{Si}$ (as well as for other known states).

Other work, including $(^3\text{He}, d)$, predicted an $^{26}\text{Al}(p, \gamma)^{27}\text{Si}$ resonance at $E_p = 193$ keV and our first run, scaled down from the known and observed 203-keV resonance in $^{27}\text{Al}(p, \gamma)^{28}\text{Si}$, bracketed this region. A resonance was indeed observed at $E_p = 196$ keV and subsequent analysis confirmed it to come from $^{26}\text{Al}(p, \gamma)^{27}\text{Si}$. Several runs were taken on this resonance for a total integrated charge of 4.7 Cb, at an average beam current of $110 \mu\text{A}$. Target deterioration was monitored periodically and corrected for. In addition, we remeasured the 286- and 381-keV resonances, looked for possible resonances at 235 and 247 keV, and checked several $^{27}\text{Al}(p, \gamma)^{28}\text{Si}$ resonances.

5.5: analysis

Analysis consisted of five steps: first, software cuts were used to enhance the signal-to-noise ratio of the full-energy peak, thereby identifying the reaction's Q-value; second, the area under the excitation function was determined; third, the multiplicity and branching ratios were measured; fourth, the cascade was modeled with the EGS4 code to normalize the efficiency curve; fifth and finally, systematic corrections similar to those described in Section 3.2 were taken into account.

Figures 5.5 through 5.9 present this sequence for the 196-keV resonance. The raw SUM spectrum was dominated by the $^{11}\text{B}(p, \gamma)^{12}\text{C}$ reaction, giving lines at 4.4 and 11.6 MeV as well as their sum at 16 MeV. However, a window from 5 to 8 MeV projected onto the ramp-voltage axis showed a clear resonance. Requiring coincidence between two detectors removed much of the boron background from the region of interest, and provided a statistically clearer resonance shape. Finally, requiring three detectors each to have over 2 MeV deposited virtually eliminated the background and enhanced the probability that such an event had deposited its full energy in the detector. The 7.65-MeV centroid of the resulting sum peak was

consistent with the $^{26}\text{Al}(p, \gamma)^{27}\text{Si}$ reaction and the presence of a triple cascade was suggested, and subsequently confirmed.

Requiring coincidence between detectors obviously creates a strong dependence on branching ratios and angular correlations and was avoided in the yield measurements. Integrated area of the excitation function \mathbf{A} could be determined by simple background subtraction for most resonances. However, because of the large background for the 196-keV resonance, it was necessary to create a template which could then be fitted to the excitation function by varying only its height and a linear background (Figure 5.5). The coincidence windows creating this template gave the best statistics on the resonance shape but rendered analysis of its yield impractical. Background subtraction in determining the template was given by applying these same coincidence windows to events depositing 9–17 MeV, and then normalizing to the non-resonant region of the ramp. Excitation functions resulting from integrating the SUM spectrum between successively lower limits and E_x were then fitted using the template, thus mapping out an efficiency curve as before (Figure 5.6). The useful lower integration limit for all $^{26}\text{Al}(p, \gamma)^{27}\text{Si}$ resonances was about 1.2 MeV, since the detector had about a 60% efficiency for detecting the annihilation radiation following the delayed β^+ decay of ^{27}Si . This phenomenon is displayed in Figure 5.7. For the 196-keV resonance, the lower limit was even higher at 2.9 MeV, below which the signal to noise quickly fell to $\approx .01$ because of background target activity. Poor statistics prevented extraction of resonance yields at this level.

Cascade schemes were determined by looking at individual detector contributions to events which appeared in the full-energy region. The resulting four spectra—one from each detector—were then combined. Figure 5.8 shows this decomposition, both on the peak of the resonance and below it. Several lines are apparent and correspond to known transitions in ^{27}Si . Further coincidence requirements helped in their identification as illustrated in Figure 5.9. Looking at the

energy deposited in each of three detectors (and combining the results) when the fourth had 2.2 MeV deposited, one still finds a line at 2.2 MeV, as well as one at 3.2 MeV. This corresponds to the cascade $\Gamma \rightarrow 4448 \rightarrow 2164 \rightarrow 0$ keV, deduced by listing all possible cascades through known states and checking for overall consistency. By this process the main transitions were identified. Similar efforts for the stronger 286- and 381-keV resonances were in good agreement with the principal branching ratios previously determined with the germanium detector.

Using this branching information, the detector response was modeled with the EGS4 code. For the 196-keV resonance, one can see in Figure 5.9 that most of the spectrum can be accounted for by the triple cascade determined above; the line at 2.9 MeV requires another deexcitation mode. The final branching ratios are given in Figure 3.8. An EGS-modeled efficiency curve using these branching ratios was created to which the experimental curve was normalized. Figure 5.6 shows the quality of this approach. For the 286- and 381-keV resonances, branching ratios taken from the germanium work were used in the Monte-Carlo calculations.

Finally, several corrections were taken into account. Target deterioration was fit linearly with the cumulative charge deposited. Dead time as a function of ramp voltage was also corrected for by dividing out the pulser spectrum. Charge leakage to ground was monitored by recording the integrated charge versus target voltage. Since beam currents for the normalization runs were limited to $7 \mu A$ (to keep dead-time corrections to a few percent), and the leakage current at 20 kV was occasionally as high as $1 \mu A$, a 7% charge correction was sometimes required. Beam focusing due to the lens effect of 20 kV on the target chamber gave less than a 10% change in beam spot size. The effect of this was found negligible by comparing the ramped excitation function of one resonance when it appeared at low voltages to one where it appeared at high voltages (arranged by using different terminal potentials in the accelerator). The amount of ^{27}Al in the target was determined by comparing the

406-keV resonant yields of the target to that of a solid ^{27}Al blank, removing any dependence on the resonance strength, but requiring knowledge of the dE/dx of protons in Al.

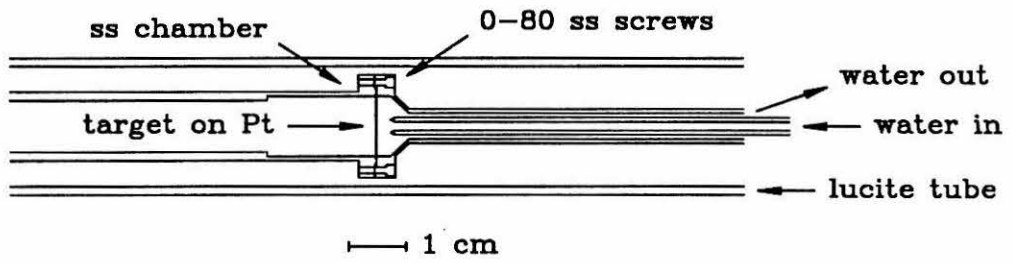
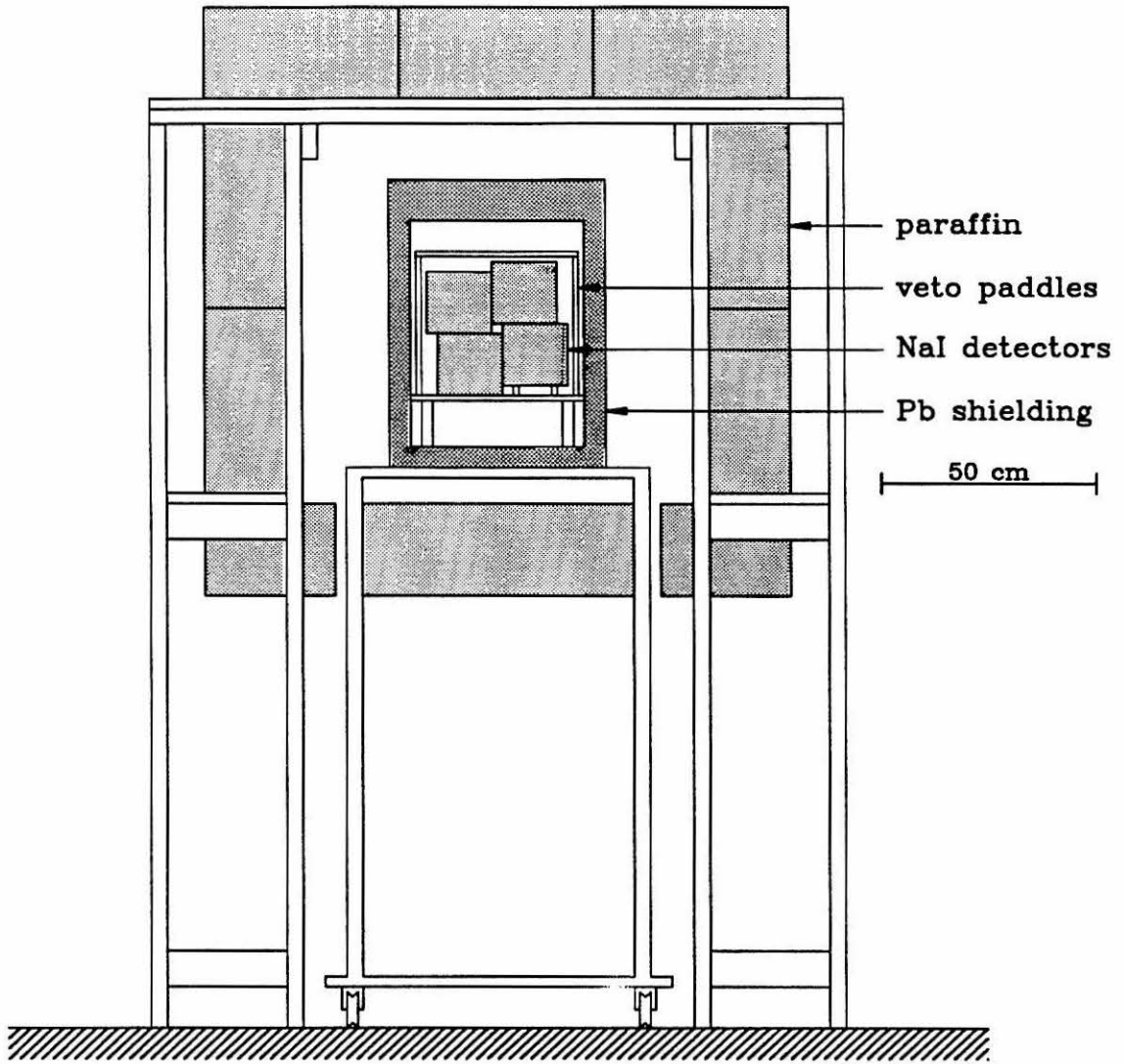
5.6: resonance strengths

We find the 196-keV resonance to have a strength of $\omega\gamma = 55 \pm 9 \mu\text{eV}$, consistent with the previous upper limits. The possible resonance at $E_p = 234 \text{ keV}$ is given an upper limit of $\omega\gamma \leq 40 \mu\text{eV}$ by scaling the 286-keV resonance yield with no coincidence requirements. Should this resonance cascade through either the 2164- or 2910-keV state, a lower limit can be set by requiring 2 MeV be deposited in at least two detectors, thereby improving the signal to noise ratio. Requiring this same coincidence for the 286-keV resonance (or the 196-keV resonance with its different cascade scheme), provides a scaled limit of $\omega\gamma \leq 10 \mu\text{eV}$.

The possible resonance at 247 keV was analyzed similarly. With no coincidence requirements, a limit of $\omega\gamma \leq 40 \mu\text{eV}$ was established. However, when two detectors were required to have at least 2 MeV, a resonance was observed at 247 keV. To verify that this arose from $^{26}\text{Al}(p, \gamma)^{27}\text{Si}$, the total energy spectrum resulting from this coincidence requirement was examined at the peak of the resonance yield. For an ^{26}Al resonance, the full-energy peak should fall at 7.70 MeV where one does indeed find a peak (Figure 5.10). The statistics were insufficient to establish a cascade scheme so the efficiency for this coincidence requirement and SUM window was measured for the 196-, 288-, and 381-keV resonances giving 35, 25, and 28%, respectively. The average value implies a resonance strength of $\omega\gamma = 10 \pm 5 \mu\text{eV}$.

Table 6.1 summarizes the resonance strengths measured with this detector.

Figure 5.1. NaI Detector Geometry. By removing the rear shielding (not shown) the inner stand could be rolled out of the paraffin house to facilitate changing the target. The lucite tube around the target chamber was needed to stand off the 20 kV. Water cooling was gravity fed from an insulated reservoir as before.



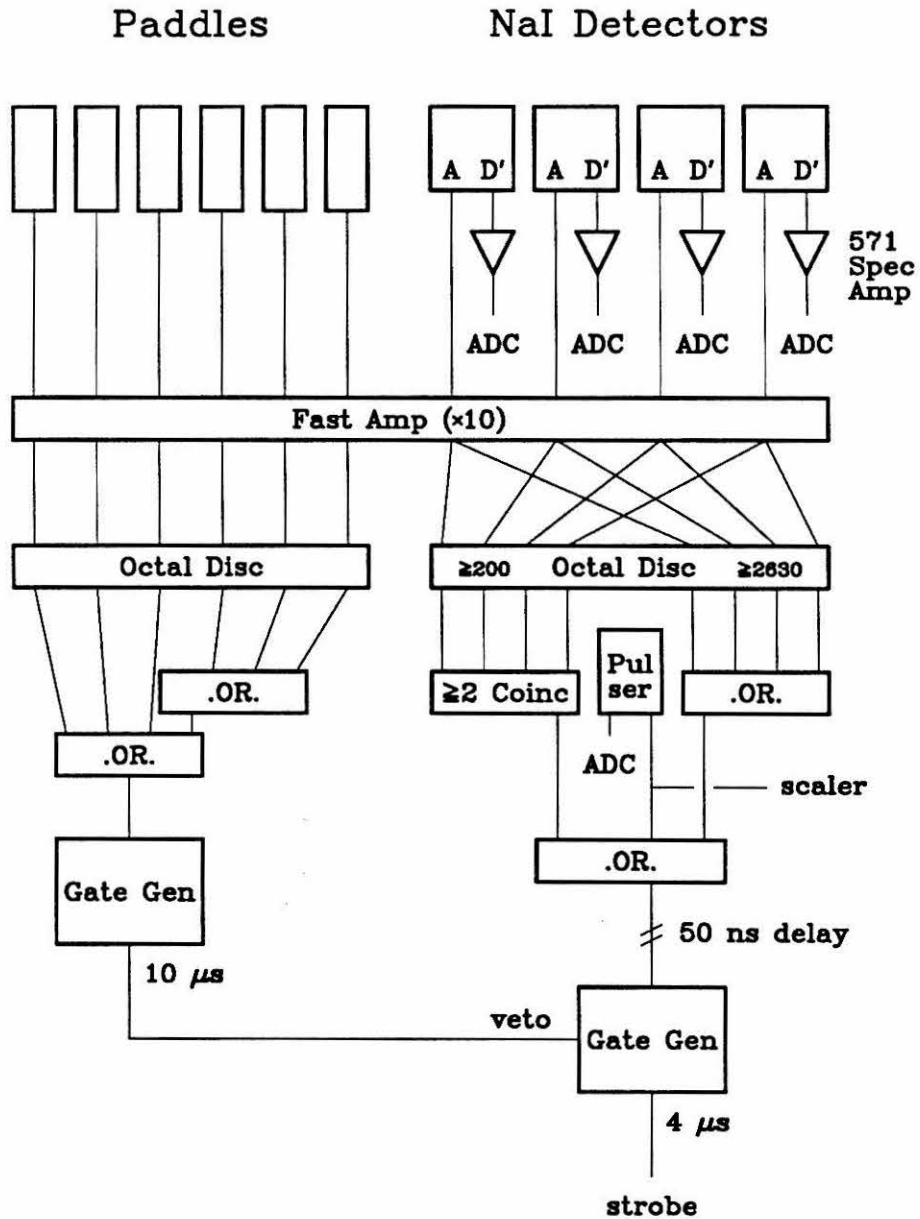


Figure 5.2. Front-End Electronics. The 4- μ s strobe necessary for the ADC conversion, along with CAMAC data-rate limitations, accounted for most of the dead time. (The cosmic-ray veto rate gave only a 1% dead time.) This meant a pulser could be inserted after the discriminator as shown and still accurately reflect the dead time.

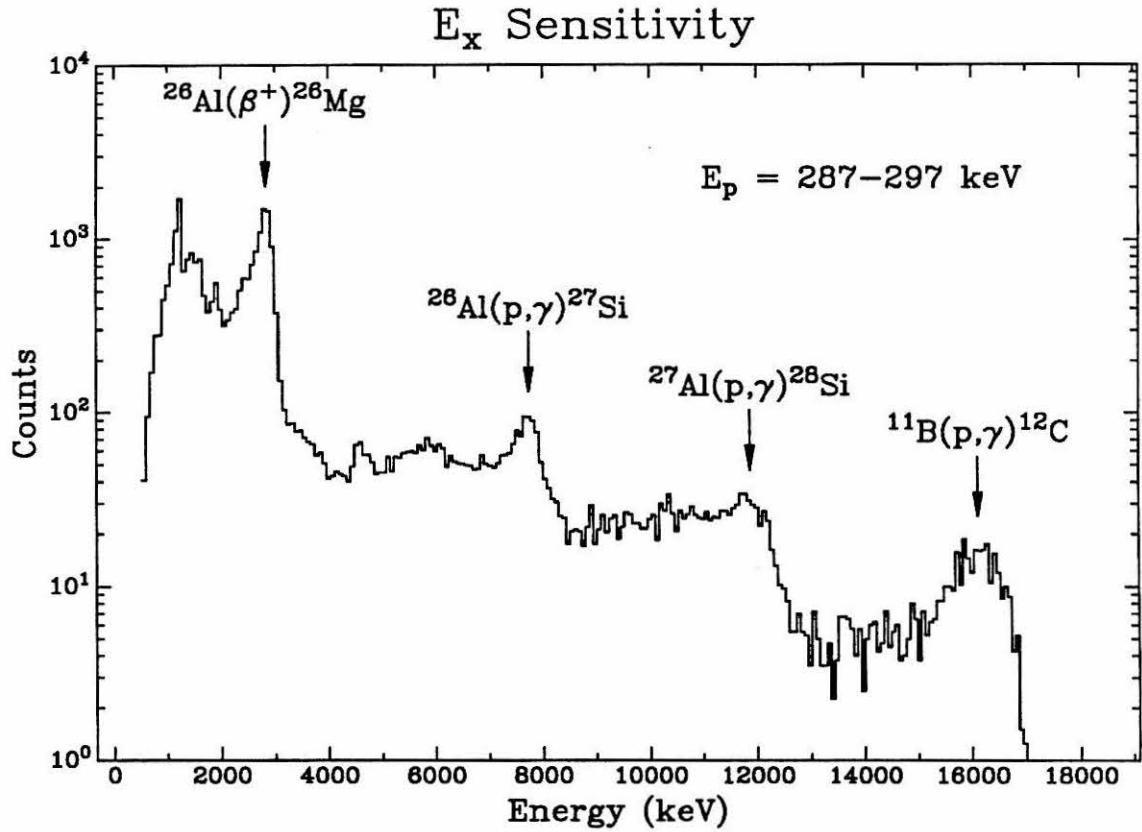


Figure 5.3. Separating Reactions by E_x. The major gamma transitions (in MeV) giving rise to this spectrum are:

$^{11}\text{B}(p, \gamma)^{12}\text{C}$:	4.4 + 6.6
$^{27}\text{Al}(p, \gamma)^{28}\text{Si}$:	1.8 + 3.2 + 6.8
$^{26}\text{Al}(p, \gamma)^{27}\text{Si}$:	2.2 + 5.6
$^{26}\text{Al}(\beta^+)^{26}\text{Mg}$:	0.5 + 0.5 + 1.8

Figure 5.4. Detector Efficiency. For each event, summing the energy deposited in the detectors (NA-SUM) would ideally give a delta function at E_x , and a narrow window integrating this peak would have 100% efficiency. Frequently, however, only a fraction of E_x is deposited in the active detector regions, forcing the integral to start from lower energies in order to include them. The solid curves show the fraction of events actually observed as a function of this lower threshold.

The legend in each frame indicates the reaction measured and the principal gamma multiplicities. Indicated at the upper left are uncertainties in the total calculated yield based on the literature $\omega\gamma$ and dE/dx . The ^{24}Na source was made and calibrated for this experiment.

Dashed curves are from EGS Monte-Carlo simulations using the known cascade schemes.

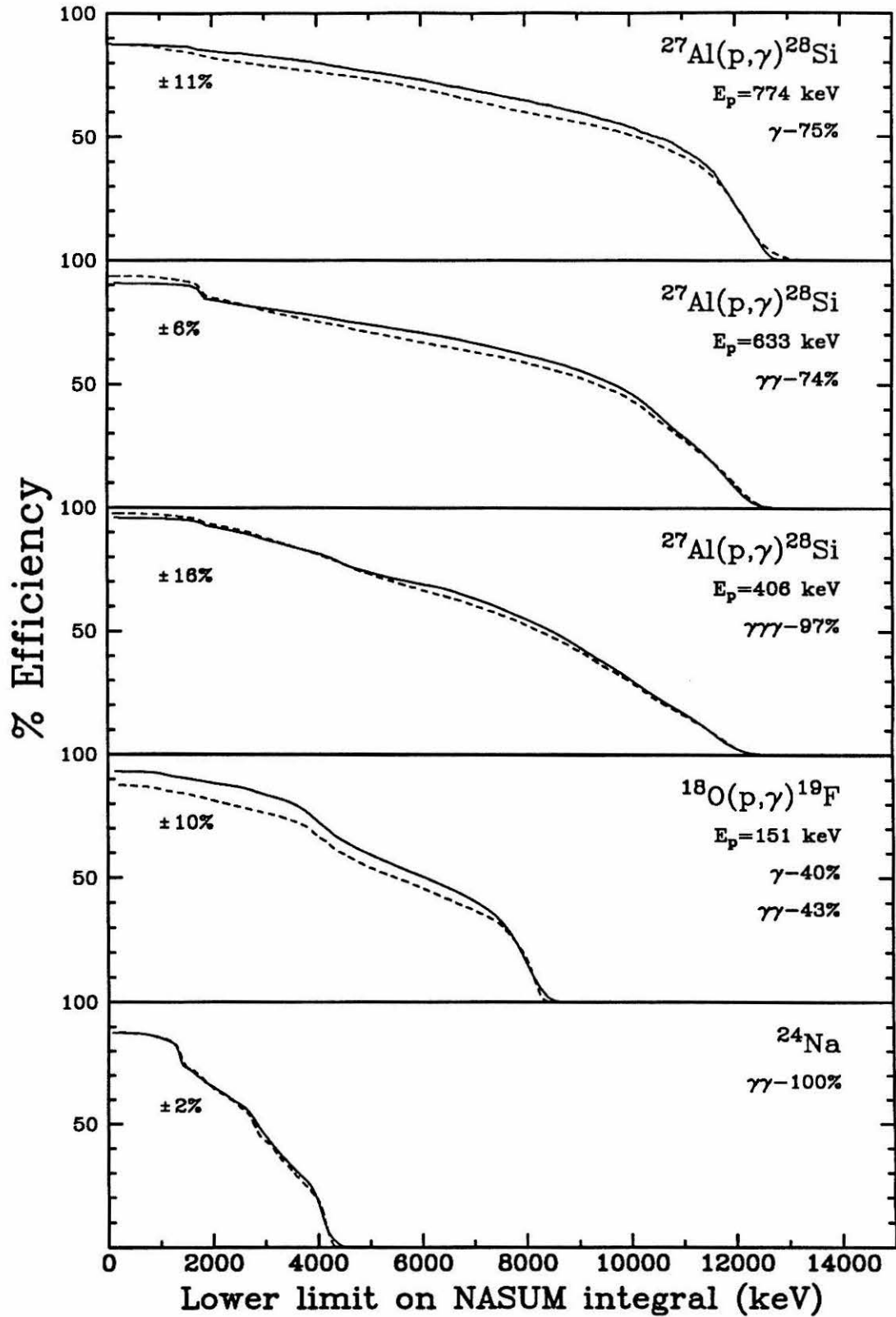
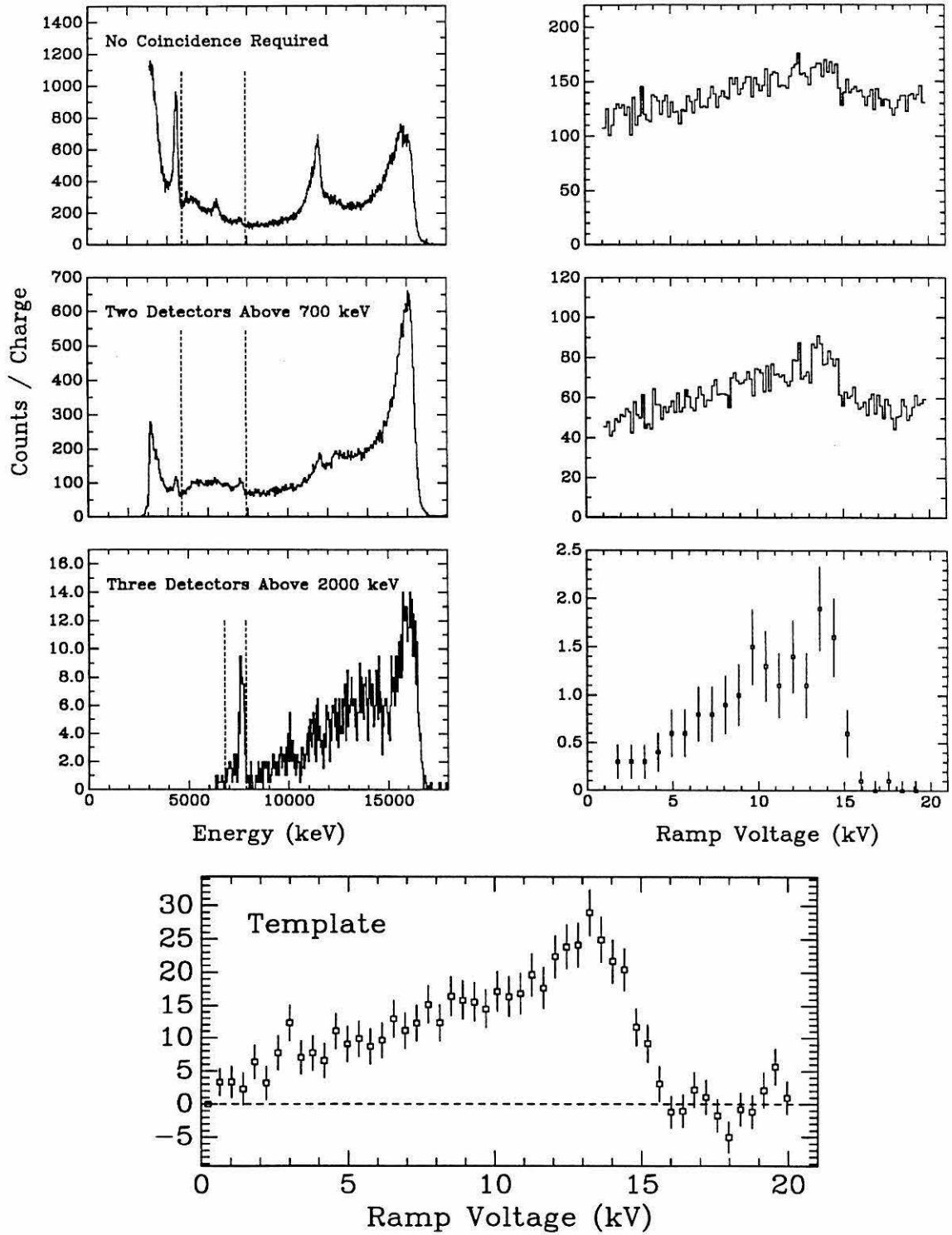


Figure 5.5. 196-keV Resonance. Energy spectra resulting from the indicated coincidence requirements are shown on the left. The region between the dashed lines was then projected against the ramp voltage to give the excitation function on the right.

The excitation function template shown at the bottom originated from an energy spectrum requiring two detectors be above 1.1 MeV. Events meeting this requirement and having an energy of 3.8–5.5 or 6.5–7.3 MeV were projected against the ramp voltage. Then, since the background excitation function should be that of boron, the excitation function of events having between 8.0 and 16.5 MeV was normalized to the region of the ramp below resonance and subtracted away.



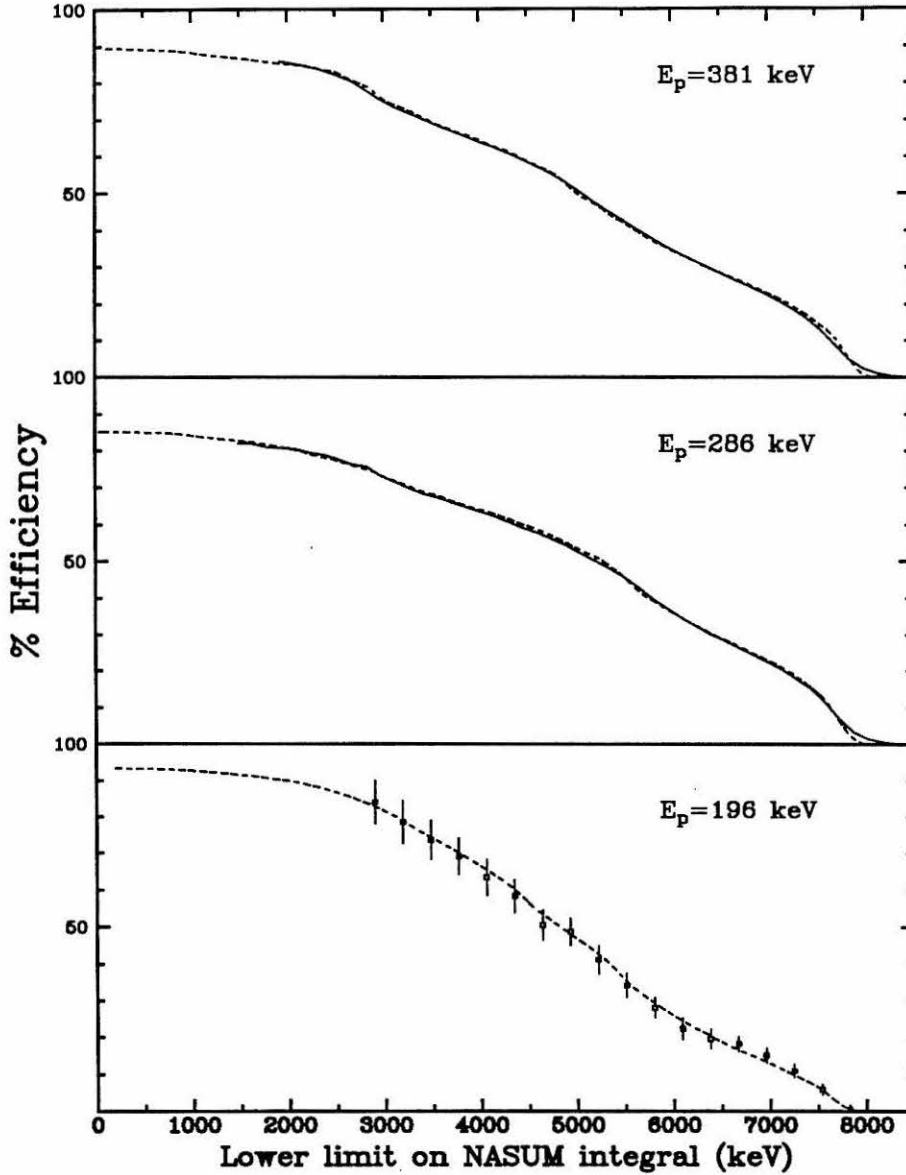
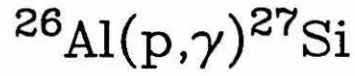


Figure 5.6. Efficiency Curves for ^{26}Al Resonances. The dashed curves are EGS Monte-Carlo simulations using the branching ratios of figure 3.8. Our results (solid curves) have been normalized to the EGS efficiency. The 196-keV resonance curve was mapped out by fits to a template as described in the text. (Note—the error bars are not independent.)

$^{26}\text{Al}(p,\gamma)^{27}\text{Si}$ ($E_r=381$ keV)

$^{27}\text{Si}(\beta^+)^{27}\text{Al}$ (4.13 sec)

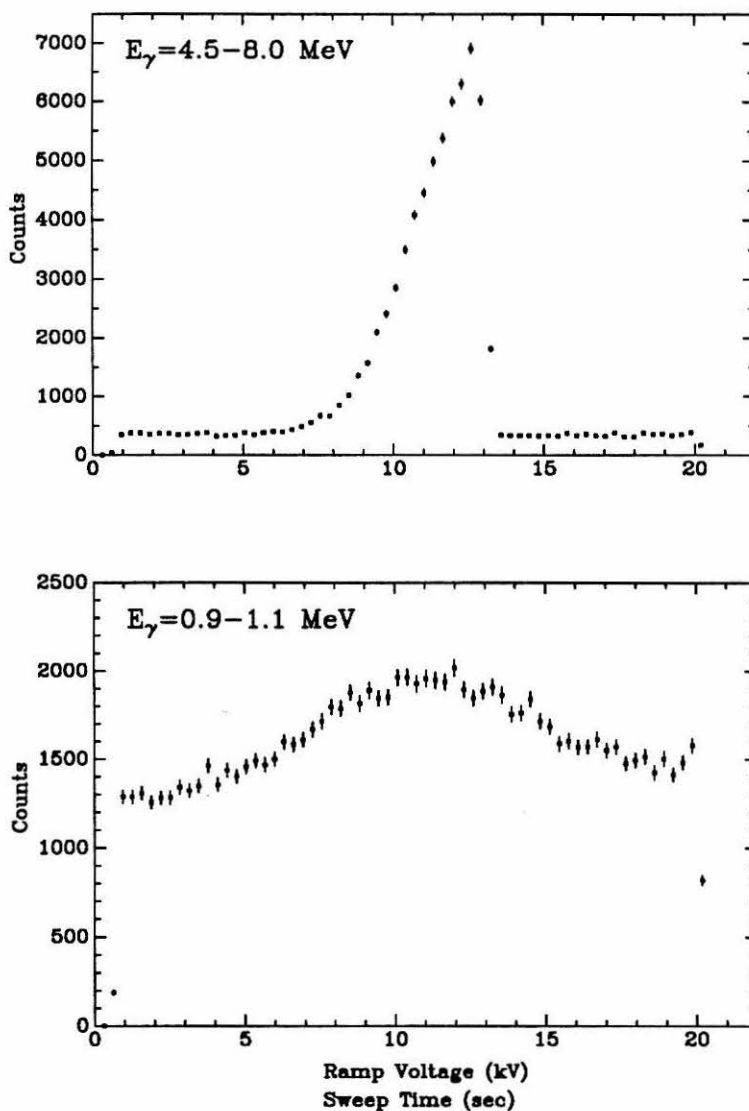


Figure 5.7. Delayed ^{27}Si β^+ Decay. The upper excitation function reflects prompt γ -rays from the de-excitation of $^{27}\text{Si}^*$ while the lower one reflects a 60% efficiency for detecting both annihilation quanta following $^{27}\text{Si}(\beta^+)^{27}\text{Al}$. The four-second half life of ^{27}Si allows the bi-directional ramp (which has a forty second period) to smear the excitation function of this 1.02 MeV line.

Decomposition of Full-Energy Region

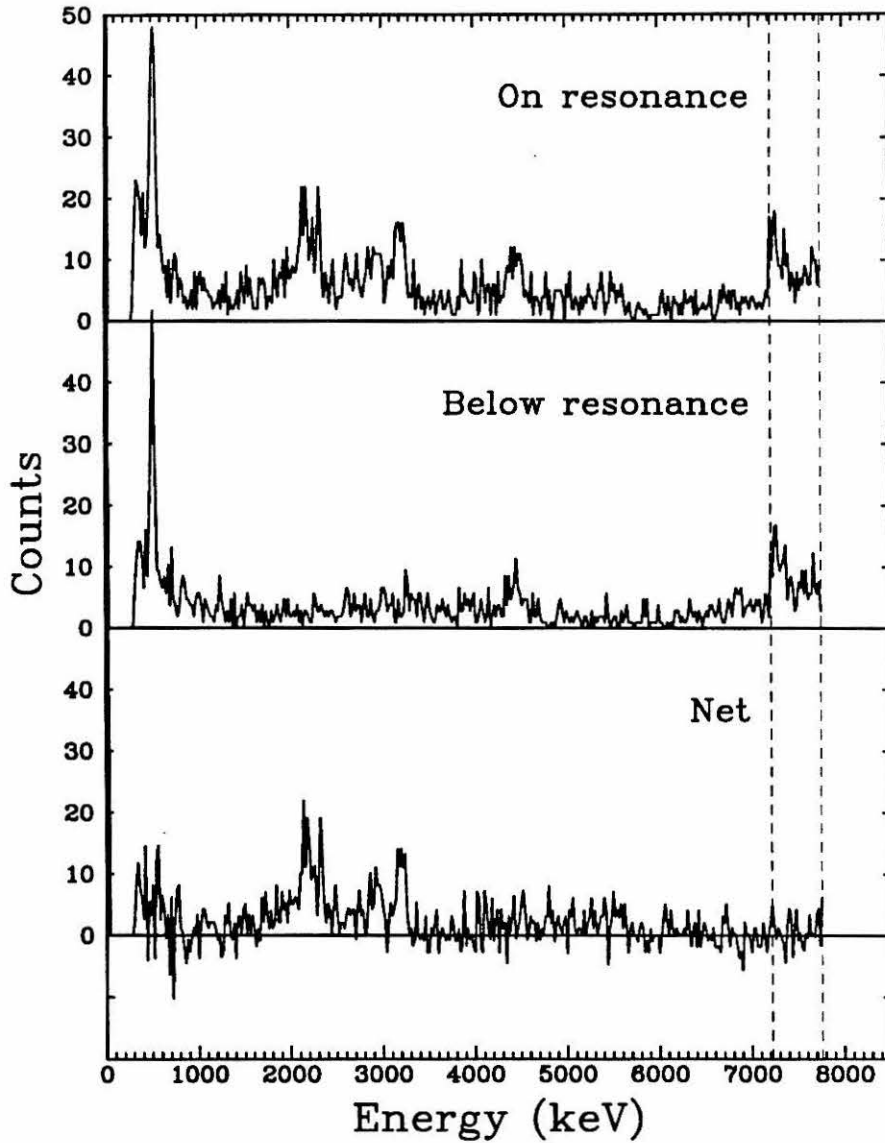


Figure 5.8. γ -rays from the 7653-keV State in ^{27}Si . The spectra of individual detectors have been combined for events which deposited a total energy of E_x (region between dashed lines). The line at 4.4 MeV comes from $^{11}\text{B}(p, \gamma)^{12}\text{C}$ when the 4.4 MeV γ -ray summed with a Compton event from the 11.6-MeV γ -ray, giving a total energy near E_x .

Branching Ratio Determination

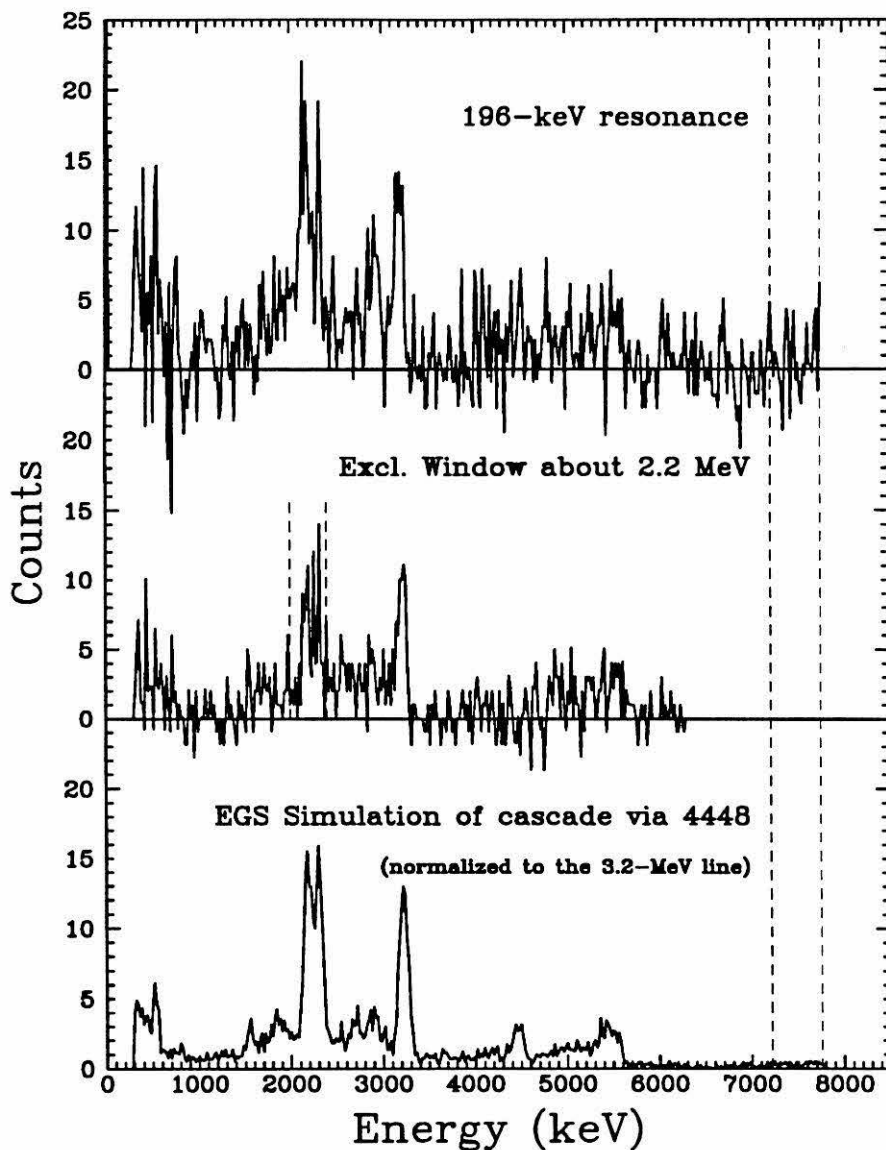


Figure 5.9. Determining Branching Ratios for the 7653-keV State. Individual cascade modes were isolated using suitable coincidence requirements and the resulting yields were normalized by Monte-Carlo methods. Identification of the $R \rightarrow 4448 \rightarrow 2164 \rightarrow 0$ decay mode is presented here.

247-keV Resonance

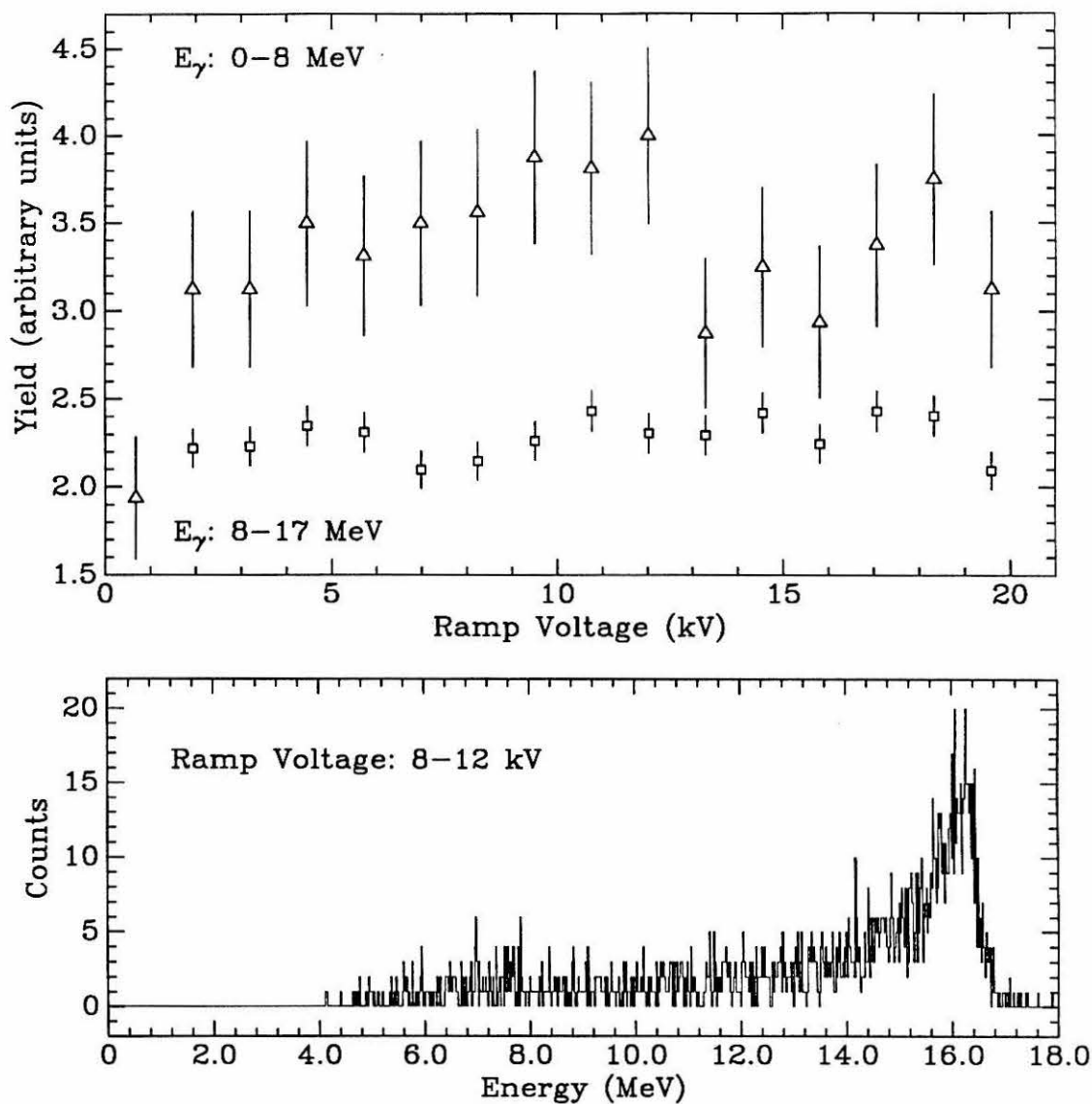


Figure 5.10. 247-keV Resonance. Events in the above spectra were required to deposit at least 2 MeV in each of two separate detectors. The full-energy peak for a resonance at $E_p = 247 \text{ keV}$ is expected to appear at 7.7 MeV. The large background from boron shows no signs of resonating.

CHAPTER 6

Conclusions and Future Directions

Results of our investigations are summarized in Table 6.1, where properties of each $^{26}\text{Al}(p, \gamma)^{27}\text{Si}$ resonance are tabulated. The ensuing reaction rate $N_A \langle \sigma v \rangle$ (where N_A is Avogadro's number) is plotted in Figure 6.1a as a function of stellar temperature, along with the findings of previous work. The increased lower limit reflects our direct measurement of the 196-keV resonance while the reduced upper limit reflects better limits on unobserved resonances.

6.1: comparison to statistical-model calculation

Direct comparison of our results to the Hauser-Feshbach (HF) statistical-model calculations of Woosley et al. (WOO78) is not strictly valid: our target was in the ground state whereas they assumed the ^{26}Al to be in thermal equilibrium with its excited states. Accordingly, we performed our own HF calculations using the code HAUSER*5 (MAN83) and specifying $^{26}\text{Al}_0$ as the target. The resulting cross section for $E_p = 0-10$ MeV was used to calculate $\langle \sigma v \rangle_{\text{HF}}$. In addition, the HF cross section for $E_p = 1.0-10$ MeV was used to determine the contribution to $\langle \sigma v \rangle$ of resonances above our measured excitation function. The fractional amount of this contribution is indicated in the lower right curve of Figure 6.1b.

An analytical expression for $\langle \sigma v \rangle$ similar to that found in (CAU88) was obtained by assuming $l_p = 2$ and $\theta^2 = 0.01$ for the hypothetical 72- and 97-keV resonances. (Assuming $l_p = 0$ for the 286- and 381-keV resonances gives $\theta^2 = .003$ in both

cases.) The resulting $\langle\sigma v\rangle$ was then fitted, giving

$$\begin{aligned}
 N_A\langle\sigma v\rangle = & \frac{8.744 \times 10^{14}}{T_9^{2/3}} \exp\left\{-\frac{27.602}{T_9^{1/3}}(1 + 0.158 T_9 - 0.0107 T_9^2 + 3.716 \times 10^{-4} T_9^3)\right\} \\
 & + \frac{3.26 \times 10^{-10}}{T_9^{3/2}} \exp\left\{\frac{-0.805}{T_9}\right\} + \frac{3.26 \times 10^{-3}}{T_9^{3/2}} \exp\left\{\frac{-1.453}{T_9}\right\} \\
 & + \frac{8.97}{T_9^{3/2}} \exp\left\{\frac{-2.191}{T_9}\right\} + \frac{473}{T_9^{3/2}} \exp\left\{\frac{-3.220}{T_9}\right\} \\
 & + \frac{7763}{T_9} \exp\left\{\frac{-3.944}{T_9}\right\} \quad \text{cm}^3\text{s}^{-1}\text{mole}^{-1},
 \end{aligned}$$

where terms for the four dominant low-energy resonances (72, 130, 196, and 286 keV) are included explicitly. This curve is shown as a dot-dash line in Figure 6.1b.

To facilitate comparison with widely used parameterizations of reaction rates, Figure 6.1c presents our current limits, the analytical form given above, the form found in (WOO78), and that found in (CAU88). Caughlan and Fowler (CAU88) incorporate the resonances observed by Buchmann et al. (BUC84) and also provide separate rates for reactions on $^{26}\text{Al}_o$ and $^{26}\text{Al}^m$ targets. The rate given in (CAU88) for the isomeric state was about twice that for the ground state. When considering the destruction of $^{26}\text{Al}_o$, however, even above $T_9 = 0.4$ when the 0^+ isomeric state comes into thermal equilibrium with the 5^+ ground state, the larger statistical weight of the ground state causes it to dominate the total destruction rate. This total rate is presented as the solid curve, while that for the ground state alone is given by the dashed curve and is slightly less than the total rate at the higher temperatures.

6.2: consequences for specific production sites

By comparing the current reaction rate to those used in the model calculations discussed in section 1.3, the effects of the new rate on net ^{26}Al production can be predicted.

For supernovae ($T_9 \approx 1-5$), the difference in $\langle\sigma v\rangle$ between (WOO78) and (CAU88), both of which are HF predictions (presumably using differing parameters) can reach

a factor of 2.5! Over this temperature range, the current $\langle\sigma v\rangle$ is nearly a constant factor of 2.5 below that found in (WOO78). This would substantially modify the fifty-fold under-production by this source estimated by Clayton. However, the galactic distribution of the 1809-keV γ -ray line also casts doubt on supernovae as a major source of ^{26}Al (section 6.4).

For novae ($T_9 \approx 0.07\text{--}0.3$), the observation of a 196-keV resonance also has a substantial effect. The most recent network calculations of nova nucleosynthesis were performed by Wiescher et al. (WIE86A). They calculated $\langle\sigma v\rangle$ for $^{26}\text{Al}(p, \gamma)^{27}\text{Si}$ based solely on the results of Buchman et al., choosing to disregard possible lower resonances which had been identified by Schmalbrock et al. Consequently, their destruction rate of ^{26}Al at $T_9 \approx 0.1$ is at least two orders of magnitude too low. (Additionally, other experiments have revealed a lack of low-energy resonances in $^{27}\text{Al}(p, \alpha)^{24}\text{Mg}$ which are needed to close the “Mg-Al cycle,” further depleting the amount of ^{26}Al produced (TIM88, CHA88).) Since Wiescher et al. had concluded that only about $0.2 M_\odot$ of ^{26}Al could be maintained by a nova rate of 40 per year, the even lower production implied by the current work casts doubt about novae as the dominant source of ^{26}Al . (To enable ready comparison of his results, which utilized updated reaction rates, to those of Hillebrandt and Thielemann (HIL82), Wiescher et al. only ran calculations for novae occurring on C-O white dwarfs with a solar mixture in the hydrogen envelope. The rarer novae involving O-Ne-Mg white dwarfs might give significantly larger yields because of the extra seed Mg (STA86, HOF86).)

The most dramatic reduction of uncertainty due to the current work occurs in the temperature range relevant to red giants ($T_9 = 0.07\text{--}0.09$). Nørgaard’s reaction rate for $^{26}\text{Al}(p, \gamma)^{27}\text{Si}$ was taken from (ARN80) and is virtually identical to that of (WOO78) over the relevant temperature range. Our best value is seen to fall within 50% of that used in his modeling and, because of the large uncertainty in our rate, we leave his results unmodified.

For Wolf-Rayet (WR) stars ($T_9 \approx 0.04$ – 0.07) there still remains a large uncertainty in the reaction rate. However, Prantzos and Cassé (PRA86), who used reaction rates taken from (WOO78), claim a remarkable insensitivity to both recent changes in the $^{25}\text{Mg}(p, \gamma)^{26}\text{Al}_0$ rate (CHA86, END87) and the enhancements proposed in 1986 by Schmalbrock et al. to the $^{26}\text{Al}(p, \gamma)^{27}\text{Si}$ destruction rate. In fact, using the upper limit given in (SCH86) only changed the net ^{26}Al production by a factor of two—much less than other uncertainties in predicting the galactic production of ^{26}Al by this source. Prantzos and Cassé explain this insensitivity by noting that the (WOO78) rate, averaged over the convective core having $T_9 \approx 0.04$, is 2–3 orders of magnitude less than the $^{26}\text{Al}_0(\beta^+)^{26}\text{Mg}$ decay rate, and only towards the end of hydrogen burning, as the temperature rises, do the two rates become comparable. As we have largely eliminated the enhancements of the $^{26}\text{Al}(p, \gamma)^{27}\text{Si}$ reaction rate proposed by Schmalbrock et al. (and subsequently refined by Wang et al.), the remaining uncertainty due to the nuclear destruction rate would appear to be of little consequence.

6.3: destruction timescales

Prompted by the comments of Prantzos and Cassé, we determined the temperature below which, for a given density, the upper limit on $\langle\sigma v\rangle$ for the $^{26}\text{Al}(p, \gamma)^{27}\text{Si}$ reaction would allow the beta decay of ^{26}Al to dominate its destruction. In such an environment, the current limits on $\langle\sigma v\rangle$ would suffice. To determine this temperature, one must evaluate the effective beta-decay rate by including coupling of the ground state to the isomeric state at 228 keV, which has a 6.4 second half-life.

Ward and Fowler (WAR80) show that, due to the short half-life of $^{26}\text{Al}^m$, and in the absence of other destruction reactions, $^{26}\text{Al}_0$ and $^{26}\text{Al}^m$ fall out of thermal equilibrium below $T_9 \approx 0.4$. However, contrary to their findings, the loss rate of $^{26}\text{Al}_0$ continues to be dominated by decay through the metastable state down to

$T_9 \approx 0.16$. By using their estimates for the branching ratios of the 417- and 1058-keV levels, we find that ^{26}Al initially created in the ground state has an effective beta-decay rate given by

$$\lambda_{\beta^+}(\text{s}^{-1}) = \begin{cases} 3.06 \times 10^{-14} + 0.265 e^{-4.84/T_9} + 6.29 \times 10^8 e^{-12.3/T_9} & T_9 \leq 0.39; \\ 9.9 \times 10^{-3} e^{-2.65/T_9} & T_9 > 0.39. \end{cases}$$

This rate is equated to the proton destruction rate for various environments to provide the curves in Figure 6.2. In the region below these curves the natural decay of ^{26}Al is the principal destruction route, making details of the reaction rate against protons inconsequential. (However, even 100 neutrons/cm³ at $T_9 = 0.1$ allows $^{26}\text{Al}(n, \alpha)^{23}\text{Na}$ to dominate over beta decay (SKE87).)

The significance of a measured $\langle\sigma v\rangle$ also depends on the dynamics of the stellar environment: a reaction can be ignored if its rate is slow compared to other timescales. The lifetime of a nucleus against reacting with a proton, given by $(\rho X_H N_A \langle\sigma v\rangle)^{-1}$, also creates a lower limit on the equilibration time for flow through the reaction network. Were equilibrium attained, static calculations could be used to predict final abundances. The lifetime of ^{26}Al against protons and beta decay is given in Figure 6.3 for various environments. Unfortunately, in the Mg-Al region, even when nuclear-reaction timescales are short compared to thermodynamic changes, the effects of delayed β decays, details of freeze-out, and exhaustion of seed material require dynamic calculations in order to obtain realistic results.

6.4: galactic distributions

Comparing the 1809-keV γ -ray galactic distribution with various source distributions can provide another criterion for determining the origin of ^{26}Al in our galaxy. This requires both an accurate map of the γ -ray emission and a consensus on source distributions, neither of which is currently available. The γ -ray distribution also impacts on the equilibrium amount of galactic ^{26}Al deduced from the observed γ -ray flux (section 1.2).

Four observations of the 1809-keV γ -ray line have been reported: two using detectors aboard satellites, and two with detectors carried aloft by balloons.

The satellite-mounted detectors used by Mahoney et al. (MAH84) and Share et al. (SHA85) had angular resolutions of 42° and 130° , respectively. Such resolutions were insufficient to distinguish among candidate sources, but were capable of indicating the galactic-center region as the major source. Their initial analyses assumed a distribution similar to that of high-energy photons as measured by SAS 2 (FIC75) and COS B (MAY82).

Ballmoos et al. (BAL87), using a Compton telescope having an angular resolution of 10° , measured a γ -ray flux of $6.4 \pm 2.6 \text{ m}^{-2}\text{s}^{-1}$ having a distribution consistent with a point source at the galactic center (Figure 6.4). Subsequently, MacCallum et al. (MAC87) used a germanium detector with collimating NaI detectors in anti-coincidence. On two separate balloon flights, the field of view determined by the anticoincidence detectors was $\sim 15^\circ$ in one case and $\sim 87^\circ$ in the other. With the detector aimed at the galactic center, the difference in the net 1809-keV γ -ray counting rate between these flights was 120%—inconsistent with a point source.

Re-analysis of the Mahoney, Share, and MacCallum data, assuming a point source, all gave an equivalent point-source flux about five times less than that reported by Ballmoos et al. (HIG89). Obviously, further observations with better angular resolution and statistics are required.

Galactic distributions assumed for the various proposed sources have also been disputed. Figure 6.5 shows the longitudinal variation of the 1809-keV γ -ray flux expected for various source distributions. The large discrepancies between the two nova distributions presented by Higdon and Fowler (HIG89), and that of Leising and Clayton (LEI85), reflect different methods of scaling the local nova rate to the rest of our galaxy by using comparisons with the observed nova distribution in M31.

The distribution of WR stars is very uncertain, and various assumptions made by Prantzos and Cassé (PRA86) lead to the curves indicated. For reference, they also present the distribution of high-energy γ rays obtained by COS B which was used in the initial analysis of the 1809-keV γ -rays by Mahoney et al.

6.5: general constraints and other reactions

It is doubtful that any resolution concerning the origin of ^{26}Al is just around the corner. While novae appear to be the favorite candidates, Dearborn et al. (DEA88) argue that for any source having only solar abundance of ^{25}Mg as seed nuclei, and constrained to be within the central 1 kps of the galaxy (as suggested by Ballmoos), virtually all the ^{25}Mg would have to be converted to ^{26}Al and quickly ejected to account for the observed 1809-keV γ -ray flux. If that source were novae, one would need a rate of 3000 per year in the central region of the galaxy—75 times that expected for the *entire* galaxy. This argument can be relaxed somewhat if ^{24}Mg could also be used without concurrently destroying more ^{26}Al , or if a more diffuse source were permitted.

Whether such an efficient conversion of ^{25}Mg to ^{26}Al is possible depends largely on the $^{25}\text{Mg}(p, \gamma)^{26}\text{Al}$ and $^{26}\text{Al}(p, \gamma)^{27}\text{Si}$ reaction rates, while the feasibility of using ^{24}Mg depends on the $^{24}\text{Mg}(p, \gamma)^{25}\text{Al}$ rate. Current limits for these rates, normalized to the analytical expression given for the $^{26}\text{Al}(p, \gamma)^{27}\text{Si}$ rate in section 6.1, are presented in Figure 6.6.

The two rates for the $^{25}\text{Mg}(p, \gamma)^{26}\text{Al}$ result from the difference in $\omega\gamma$ for the $E_p = 39$ -, 60- and 96-keV resonances found in (CHA86) and (END87). Caughlan and Fowler (CAU88) adopted the values in (END87), but we do not consider the issue resolved.

The $^{24}\text{Mg}(p, \gamma)^{25}\text{Al}$ reaction has a Q-value of 2.27 MeV and populates states in a well known region of ^{25}Al . Since there is no state which could provide a resonance

between threshold and the lowest known resonance at $E_p = 223$ keV, $\langle\sigma v\rangle$ is well determined.

6.6: summary

The importance of the $^{26}\text{Al}(p, \gamma)^{27}\text{Si}$ reaction rate in determining the origin of the ^{26}Al observed in our galaxy led us to re-examine the $^{26}\text{Al}(p, \gamma)^{27}\text{Si}$ excitation function below 1 MeV, resulting in a significantly better determination of $\langle\sigma v\rangle$ at the lower temperatures. While this reaction rate is now reasonably certain for temperatures relevant to novae, some uncertainty remains for lower temperature sites.

To eliminate this uncertainty an isotopically separated ^{26}Al transmission target is needed, as current efforts to examine possible resonances below $E_p = 190$ keV using the $(^3\text{He}, d)$ transfer reaction have been hampered by the large ^{27}Al component of the target. Unfortunately, efficiencies of existing separators would require a substantial amount of ^{26}Al , and therefore substantial cost. Inquiries are underway though, and more definite information on the lower-lying states should be forthcoming.

The suggestion by Skelton et al. (SKE87) that $^{26}\text{Al}(n, \alpha)^{23}\text{Na}$ might dominate over $^{26}\text{Al}(n, p)^{26}\text{Mg}$ should also be investigated as the neutron destruction rate has been used to rule out several possible sites for ^{26}Al production. The latter reaction has been measured directly by Trautvetter et al. (TRA86) while the former is currently being pursued by us in collaboration with Koehler at LANL.

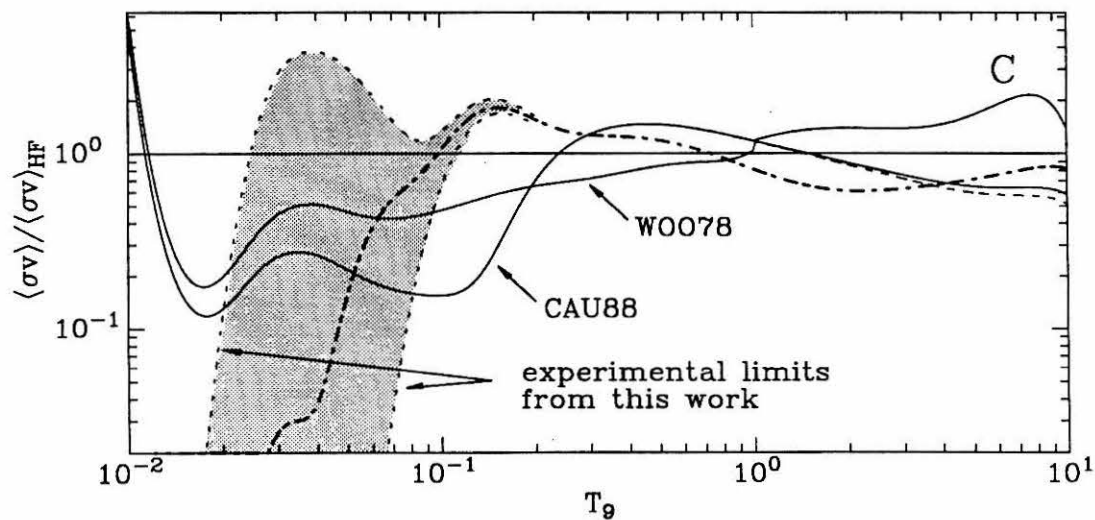
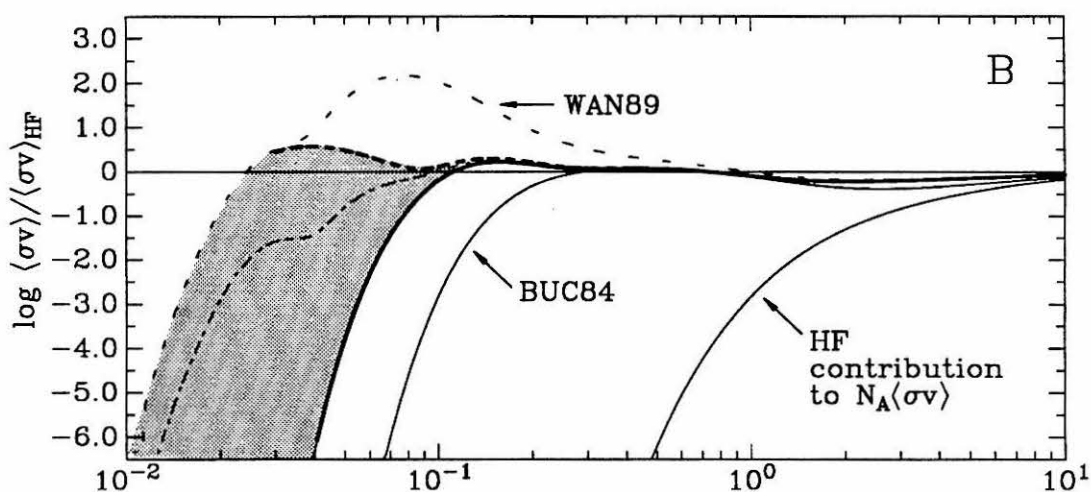
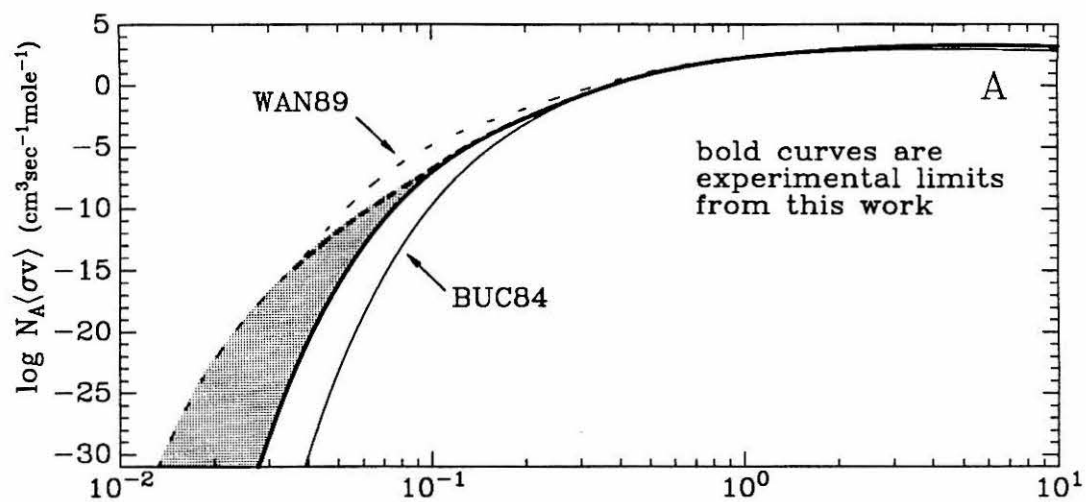
Knowing the destruction rate of ^{26}Al in various environments will not alone allow determination of its origin, but is necessary for any final scenario to be developed. Meanwhile, we await the results of stellar-model calculations using new reaction rates, and are especially eager for new information from γ -ray astronomy.

Figure 6.1. $N_A \langle \sigma v \rangle$ for $^{26}\text{Al}(p, \gamma)^{27}\text{Si}$.

A) Limits on the stellar reaction rate from this and prior work are presented. The shaded region indicates the current possible range.

B) The limits from A) have been normalized to our statistical model calculations for the reaction rate. The dot-dash line is given by the analytical expression found in Section 6.1 and represents our best “guess” for the actual rate. The fractional contribution to $\langle \sigma v \rangle$ due to resonances above 1 MeV (modeled by using Hauser-Feshbach predictions) is given by the lower right curve.

C) Our current limits and Hauser-Feshbach calculations are compared to those of Woosley (WOO78) and Caughlan (CAU88) (see text).



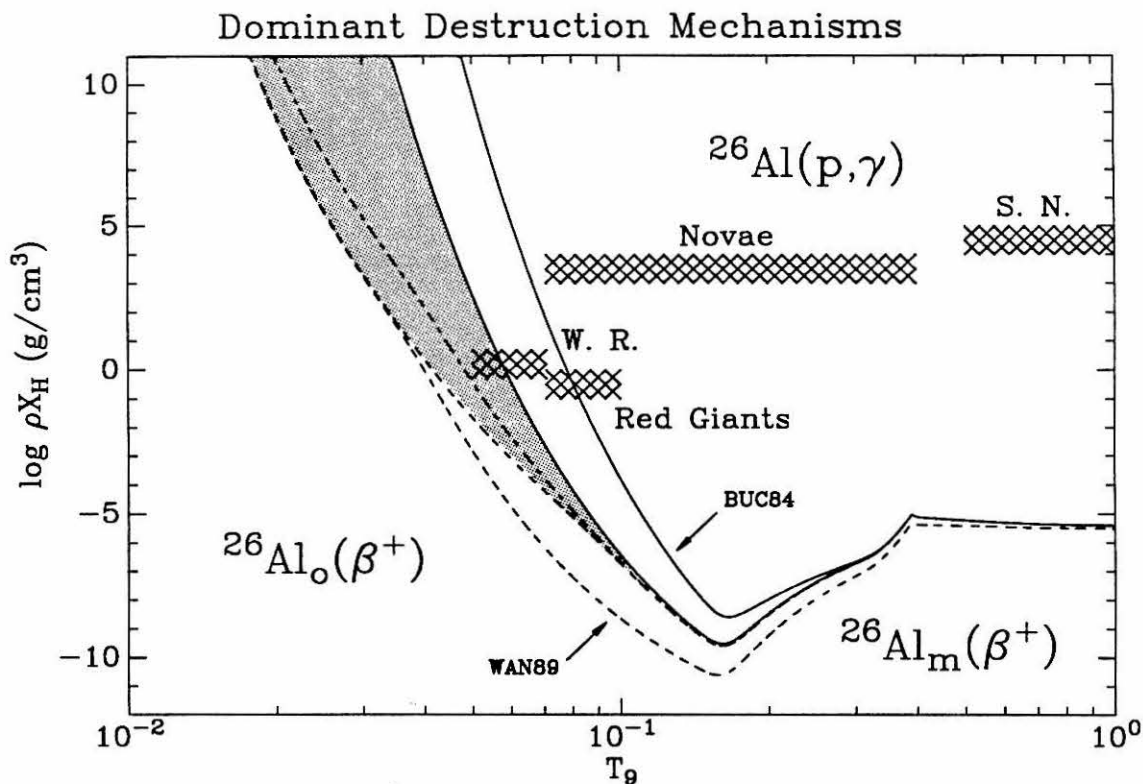


Figure 6.2. Dominant Destruction Mechanisms. These curves were determined by setting the effective β^+ decay rate of $^{26}\text{Al}_0$ equal to its (p, γ) destruction rate given by $\rho X_H N_A \langle \sigma v \rangle$. The temperatures and densities given for the stellar environments are only approximate.

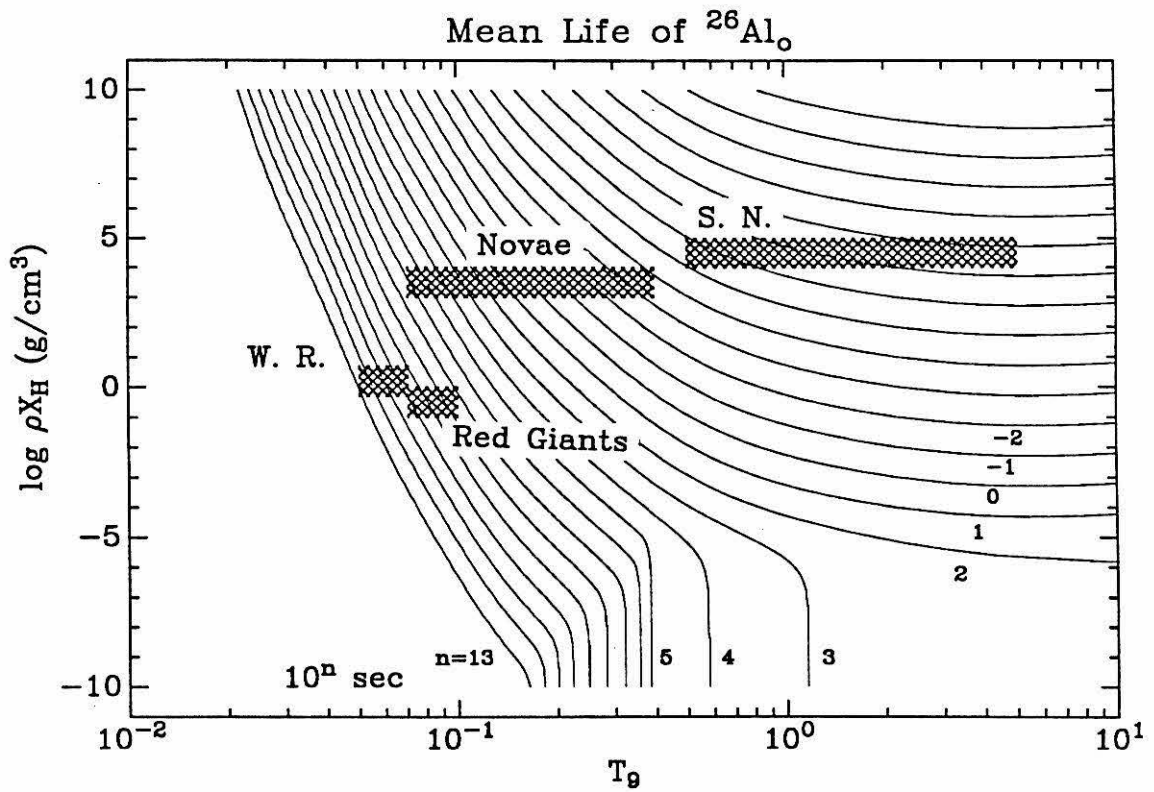


Figure 6.3. Mean Life of $^{26}\text{Al}_0$. This figure illustrates the timescales involved for the destruction of ^{26}Al either by protons or through β^+ decay. The nuclear-reaction rate used was given by the analytical expression found in Section 6.1.

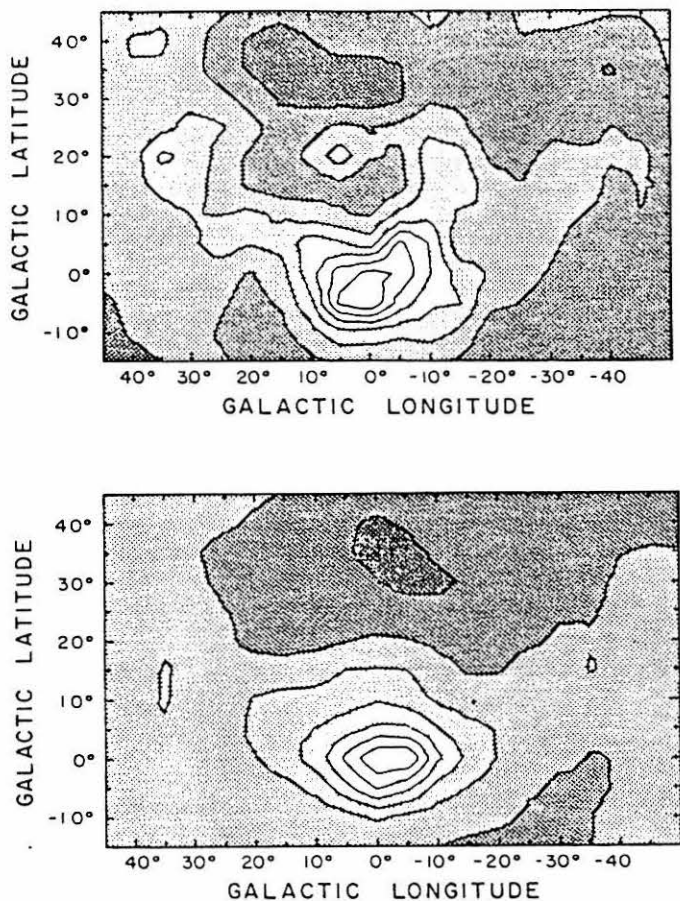


Figure 6.4. Galactic Distribution of 1809-keV γ -rays. This is Figure 3 taken from (BAL87). "SKYMAP of equidistant likelihood contour lines (in steps of 10% of the maximum value) derived from events in the interval 1.6 – 2.0 MeV. Background is determined by the mirror method. *Top:* the map derived from the balloon flight data. *Bottom:* the result of a Monte-Carlo calculations of the balloon flight under the assumption that the galactic center ($l = 0^\circ$, $b = 0^\circ$) is the only 1.8 MeV γ -ray source in the sky. No continuum and background were assumed to be present."

Figure 6.5 Model Distributions
Galactic distributions predicted for the 1809-keV γ -ray flux.

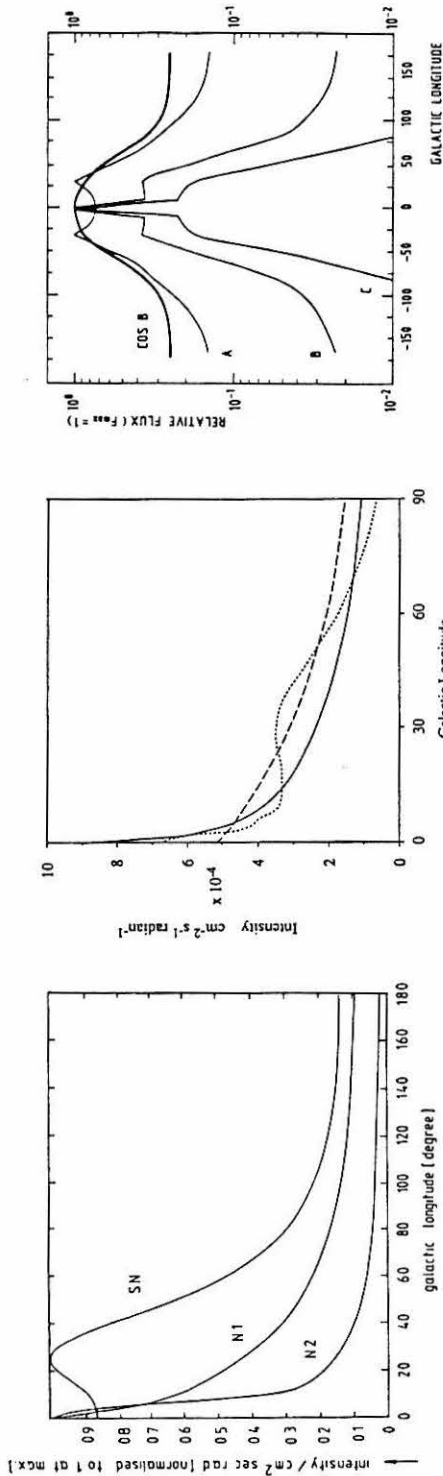


Figure 5 from (BAL87). The supernovae (SN) and N2 novae distributions are from (LE185). The N1 novae distribution is from (MAH85). The intensity has been normalized to have a maximum of unity.

Figure 1 from (HIG89). Predictions for various types of novae: the dashed curve is for accreting CO white dwarfs, the dotted line is for accreting ONeMg white dwarfs employing a population I spatial distribution, and the solid line is similar except employing a disk-spheroid nova distribution (HIG87).

Figure 5 from (PRA86). Expected flux for various assumptions about the radial distribution of WR stars: a) that of giant HII regions, b) that of molecular H₂, and c) as in b) but additionally assume that the number of WR stars relative to O stars varies as $(Z/Z_0)^{1.7}$. Fluxes have been normalized to unity. The distribution of high-energy γ rays observed with COS B is also indicated.

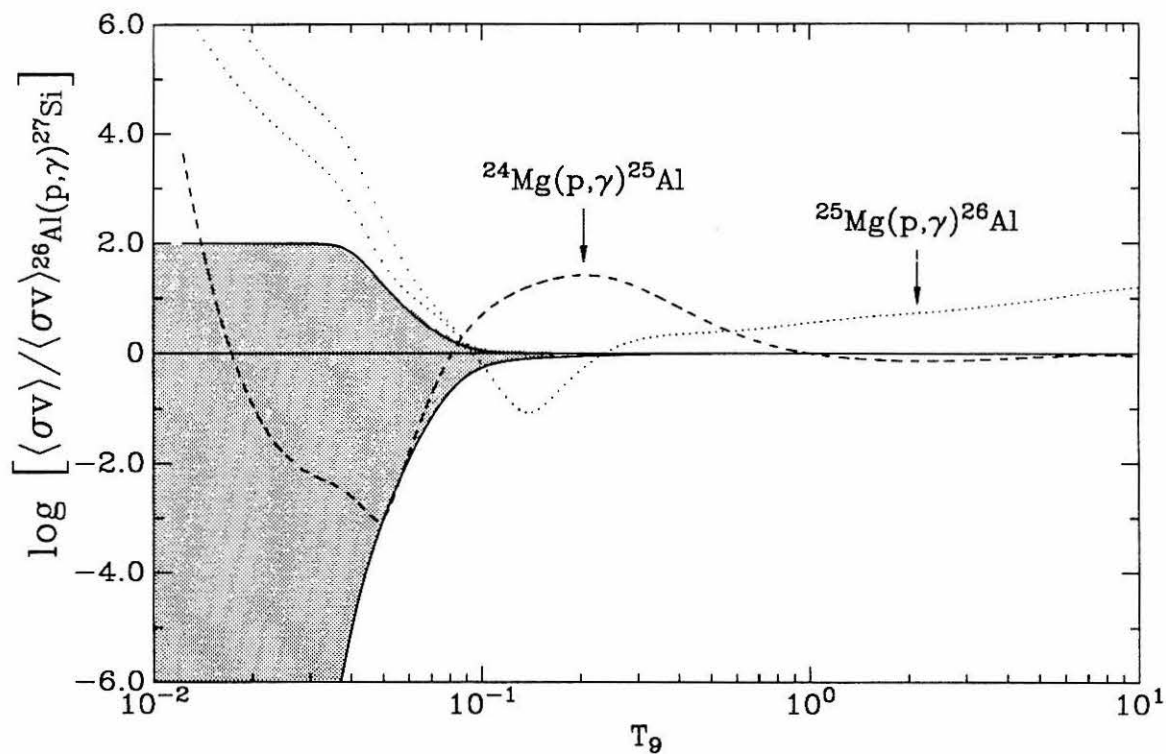


Figure 6.6. Comparison to Other Important Rates.

The $^{24}\text{Mg}(p, \gamma)^{25}\text{Al}$ and $^{25}\text{Mg}(p, \gamma)^{26}\text{Al}$ rates, taken from (CAU88) and (CHA86, END87), respectively, have been normalized to our "best value" for the $^{26}\text{Al}(p, \gamma)^{27}\text{Si}$ rate. The larger rate for $^{25}\text{Mg}(p, \gamma)^{26}\text{Al}$ comes from (END87), who finds larger strengths than (CHA86) for unobserved low-energy proton resonances (based on transfer reactions). Current experimental limits for the $^{26}\text{Al}(p, \gamma)^{27}\text{Si}$ rate bound the shaded region.

Table 6.1
 $^{26}\text{Al}(p, \gamma)^{27}\text{Si}$ Resonance Parameters

The resonance strengths and energies (in keV) from this and previous work are tabulated, along with the adopted strengths. Errors (in units of the least significant digit) are enclosed in parentheses. Excitation energies in ^{27}Si assume a Q-value for this reaction of 7464.6 ± 0.6 keV.

The upper limits of the 72- and 97-keV resonance strengths from (WAN89) assume $l_p = 2$ and $\theta^2 = 1$, while that for the 130-keV resonance assumes $l_p = 0$ and $\theta^2 = 1$. Wang has pointed out, however, that any one (but only one) of these three *might* proceed as an $l = 0$ resonance. Our choice provides the maximum rate for interesting temperatures.

Resonance energies for the current work were scaled from energies determined for $^{27}\text{Al}(p, \gamma)^{28}\text{Si}$ resonances by (MAA78), as reported in (END78). Unfortunately, their reliability has been brought into question: during this work a single run included two ^{27}Al resonances with reported energies of 504.90 ± 0.07 and 506.38 ± 0.07 keV; while our absolute energy calibration is only good to about 0.5 keV, only the statistics in the leading edges of an excitation function limit our ability to measure a *relative* energy within a single run. We found the two resonances above to have an energy separation of 2.1 ± 0.1 keV, contrasted to the expected 1.48 ± 0.1 keV. A similar discrepancy was observed for the 760- and 767-keV resonances. We therefore list explicitly those $^{26}\text{Al}(p, \gamma)^{27}\text{Si}$ resonance energies which were determined with respect to a single $^{27}\text{Al}(p, \gamma)^{28}\text{Si}$ resonance:

^{26}Al		^{27}Al
196.5	\leftrightarrow	202.8
285.5	\leftrightarrow	292.6
729.1	\leftrightarrow	731.4
770.3	\leftrightarrow	773.6
917.0	\leftrightarrow	923.0
927.6	\leftrightarrow	937.3
929.2	\leftrightarrow	937.3

E_p	$E_x(^{27}\text{Si})$	Observed Energies		(p, γ) resonance strength $\omega\gamma$ (meV)					$\omega\gamma_{(p,p_2)}$ (meV)				
		WAN89 E_x	BUC84 E_p	current E_p	WAN84	BUC84	HPGe	current	QDDD	NaI	adopted	BU84	current
929.2(2)	8359		927(2)	929.2(2)			67(2e)	88(14)			88(14)	900(300)	1834(275)
927.6(2)	8358			927.6(2)				38(e)			38(e)		
917.0(2)	8348			917.0(2)				30(5)			30(5)		22(4)
875.8(4)	8308			875.8(4)				103(1e)			103(1e)		
858.9(4)	8292		856(3)	858.9(4)			41(1e)	55(e)			52(7)		
847(1)	8280			847(1)				3.5(e)			3.5(e)		
792.6(4)	8228		8226(3)	790(2)		792.6(4)	35(1s)	50(e)			46(7)		1.9(5)
770.3(2)	8206		8206(3)			770.3(2)		206(31)			206(31)		12(2)
729.1(2)	8167			727(2)		729.1(2)		16(e)			33(5)		
720.3(4)	8158		8159(3)	719(2)		720.3(4)	51(27)	69(10)			67(9)		
380.5(6)	7831		7832(3)	376(3)		380.5(6)	65(1e)	64(10)		77(12)	69(7)		
286.4(3)	7740		7741(3)	286.6(3)		285.5(6)	3.8(10)	3.0(5)		2.7(4)	2.9(3)		
246.5(10)	7702		7702(3)			246.5(10)	<1.2	<0.5*		0.010(5)	0.010(5)		
235(3)	7690		7690(3)				<0.6	<0.4*		<0.01	<0.01		
195.6(11)	7653		7651(3)			195.6(11)	<0.04	<0.1*		0.055(e)	0.055(e)		
130(3)	7589		7589(3)				<6x10 ⁻³			<2x10 ⁻⁵	<2x10 ⁻⁵		
97(3)	7557		7557(3)				<2x10 ⁻⁷			<2x10 ⁻⁷	<2x10 ⁻⁷		
72(3)	7533		7533(3)				<2x10 ⁻¹⁰			<2x10 ⁻¹⁰	<2x10 ⁻¹⁰		

* assuming a 50% branch through the 2164-keV state in ²⁷Si

Appendix

Software was written to facilitate the determination of branching ratios for each resonance. This computer program requests as input: published branching ratios for bound states (using upper limits cited for weak transitions), the measured photopeak-efficiency curve, and the calculated total-efficiency curve. It then prompts for the cascading from a resonance level and traces each possible cascade sequence along with its probability. If more than five γ rays are emitted in a single cascade, that path is discarded. "Summing out" corrections for all γ rays in a given cascade are included, but "summing in" is only calculated for two-fold coincidences. (Angular distributions are assumed to be isotropic.) The output gives the fractional yield expected for each energy peak in the raw detector spectrum. (No attempt has been made to calculate amounts in escape peaks.) The program has been tested using the known cascade schemes from several $^{27}\text{Al}(p, \gamma)^{28}\text{Si}$ resonances and found reliable to the extent that angular distributions can be ignored and branching ratios are known.

Use of this program, and known decay schemes from contaminant reactions, allowed rapid identification of background lines. (An additional tool was the two-dimensional spectrum of pulse height versus ramp voltage. With appropriate windows integrating the peak and defining the background level, we could quickly check if a particular peak resonated at the right energy, or even what fraction of the observed peak was resonating.)

By calculating the expected spectrum for a 100% branch to each bound state separately, we identified which cascade modes were present in the unknown scheme. Usually each mode had a unique line which was used to normalize it. (Where there were several unique transitions in a given mode, the weighted average was used for normalization.) The expected yields of transitions common to several modes were then summed and compared to observed values. (Angular distributions and/or

obscured transitions frequently prevented a completely self-consistent picture.) We *assumed* the angular distributions of the 2164- and 2910-keV yields were averaged out since they were frequently fed by several paths. Consequently, when their observed yields could not be accounted for, an “unknown” branch directly to that state was indicated in Figure 3.8.

The following figures present the germanium spectra collected at each resonance. Following that are comparisons between the observed yields (corrected for background contaminations when appropriate or possible) and the expected strengths based on the cascade schemes in Figure 3.8. Many of the expected lines are from weak transitions or are sum peaks with yields well below the background level. Upper limits could be established for these transitions but would add little information.

Before discussing the peculiarities of individual resonances, we present evidence for a new state in ^{27}Si at 5549 ± 1 keV. The 286-, 381-, and 720-keV resonance spectra all contained two or three unidentifiable lines (resonant at the appropriate energy), two of which added up to the entrance E_x . The third would then correspond to a transition to the 2910-keV state. In addition, the ratios of these lines were similar for different resonances. In the 381-keV resonance spectrum the 5549-keV peak greatly exceeds the expected yield from $(E_x \rightarrow 4448) + (2164 \rightarrow 0)$ summing together. The $5549 \rightarrow 2910$ -keV peak is clean, and the $E_x \rightarrow 5549$ -keV transition accounts for the missing strength in the $4448 \rightarrow 2164$ -keV line. Similar arguments can be made for the other two resonances.

For the 286-keV resonance Buchmann assigns a 62% branch to the 2164-keV state, contrasted to our 42% branch. Such a large branch is inconsistent with the observed 5578-keV yield. While this might be due to angular distributions, the same argument could be made for other methods of feeding the 2164-keV level. Thus we attribute the excess yield to an unknown transition.

For the 720-keV resonance we find no evidence for a transition directly to the 2164-keV level which should appear at 5993 keV. Although a line appears near 2843 keV which would arise from a branch to the 5316-keV level, it is definitely non-resonant. The line at 5248 keV, corresponding to a transition to the 2910-keV level, is quite apparent. These differences account for the different branching ratios we obtained compared to Buchmann et al. (Their spectrum was contaminated by the $^{26}\text{Mg}(p, \gamma)^{27}\text{Al}$ resonance at 718 keV.)

For the 793-keV resonance, the 6065-keV line corresponding to a transition to the 2164-keV level does not appear. Several other details differ between the current and previous branching ratios. The presence of 1601- and 6628-keV lines indicates a transition through the 6628-keV state, which has only been seen previously in (p, t).

For the 847-keV resonance, the transition to the 2164-keV level is obscured by the 6130-keV line due to $^{19}\text{F}(p, \alpha\gamma)^{16}\text{O}$. However, a window from 5500 \rightarrow 6140-keV does show resonant behavior.

For the 859-keV resonance, the 5382-keV line, corresponding to a transition to the 2910-keV level does not appear. The excess yield observed in the 2910-keV line is attributed to unknown decay paths, or angular distribution effects. There were three lines at 1435, 1559, and 3827 keV which resonated along with the known ^{27}Si lines, but were not identified. Additionally, the lines at 1383 and 1538 keV had excessive yields (about double) for the decay scheme presented.

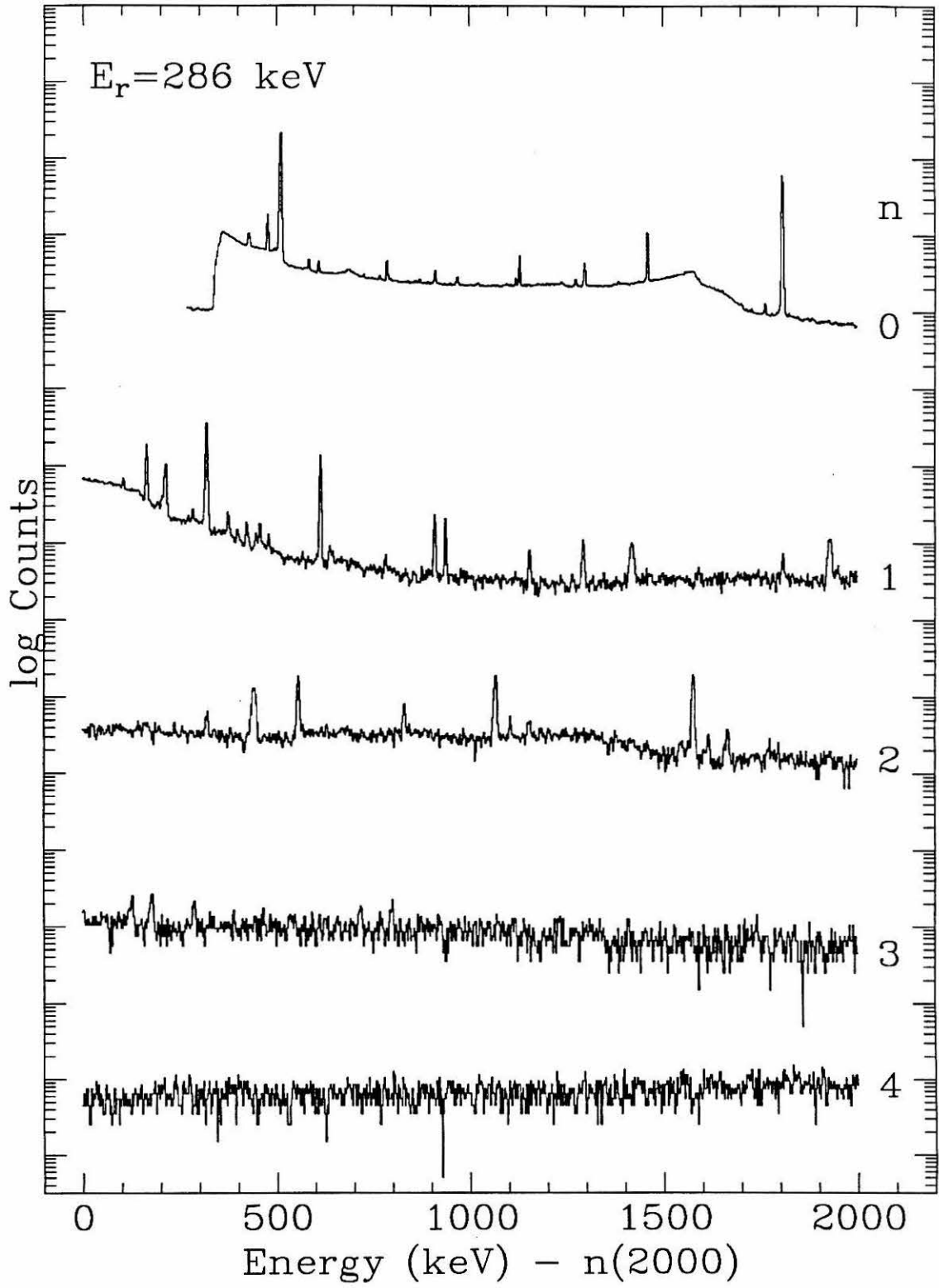
The 876-keV resonance also had weak resonating lines, which remain unidentified, at 2378 and 2808 keV. The yield of the 2164-keV line, if attributed to a direct branch to this state, should provide a visible line at 6145 keV. The lack of this line again leaves an unknown branch.

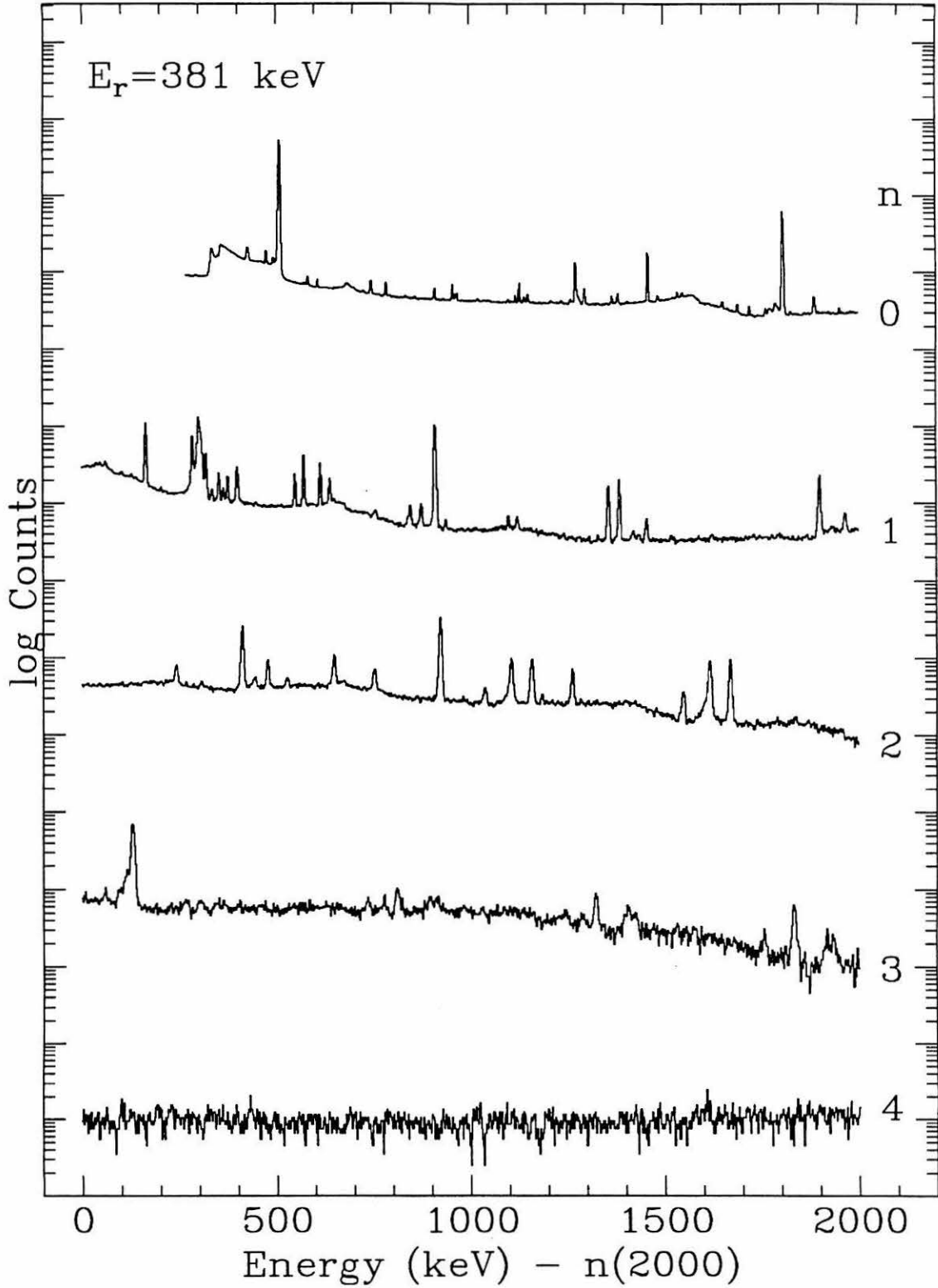
The spectrum of the 927.6-keV resonance was cleanly separated from the 929.2-keV resonance, allowing its branching ratios to be determined without corrections

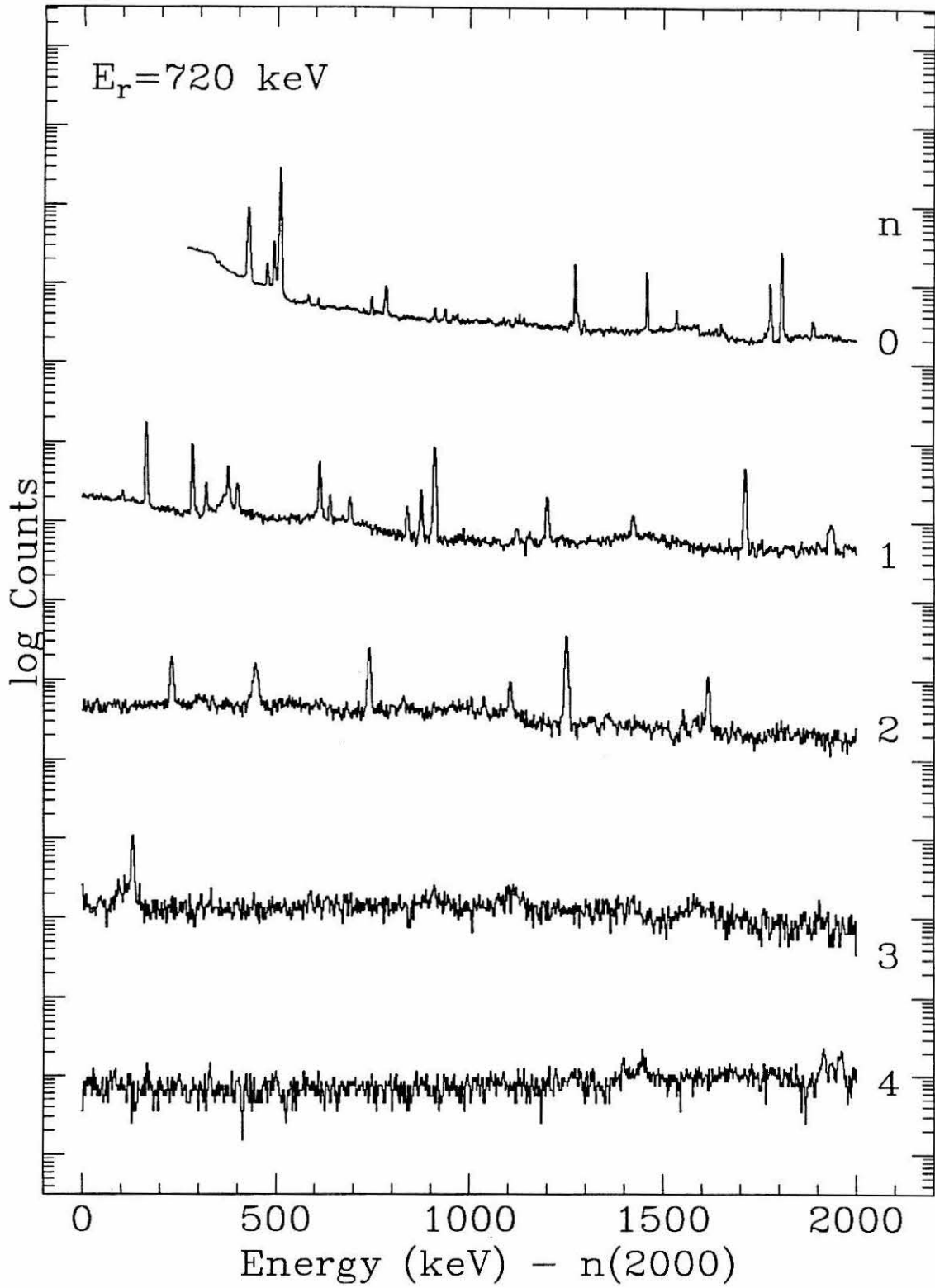
from the higher resonance. Unfortunately, there was no strong, unique γ ray from the 928-keV resonance which could be used to normalize the amount of 928-keV resonance yield present in the 929-keV resonance spectrum. To obtain this information, the double-peaked excitation function of the 2910-keV line was fit using the target profile derived from the strong 417-keV line. The ramp-voltage window used to define the 929-keV resonance spectrum was then indicated on this fit and the fraction of the 2910-keV yield due to the lower resonance determined. This amount was compared to the 2910-keV yield in the 928-keV resonance spectrum, and their ratio used to correct all the other lines.

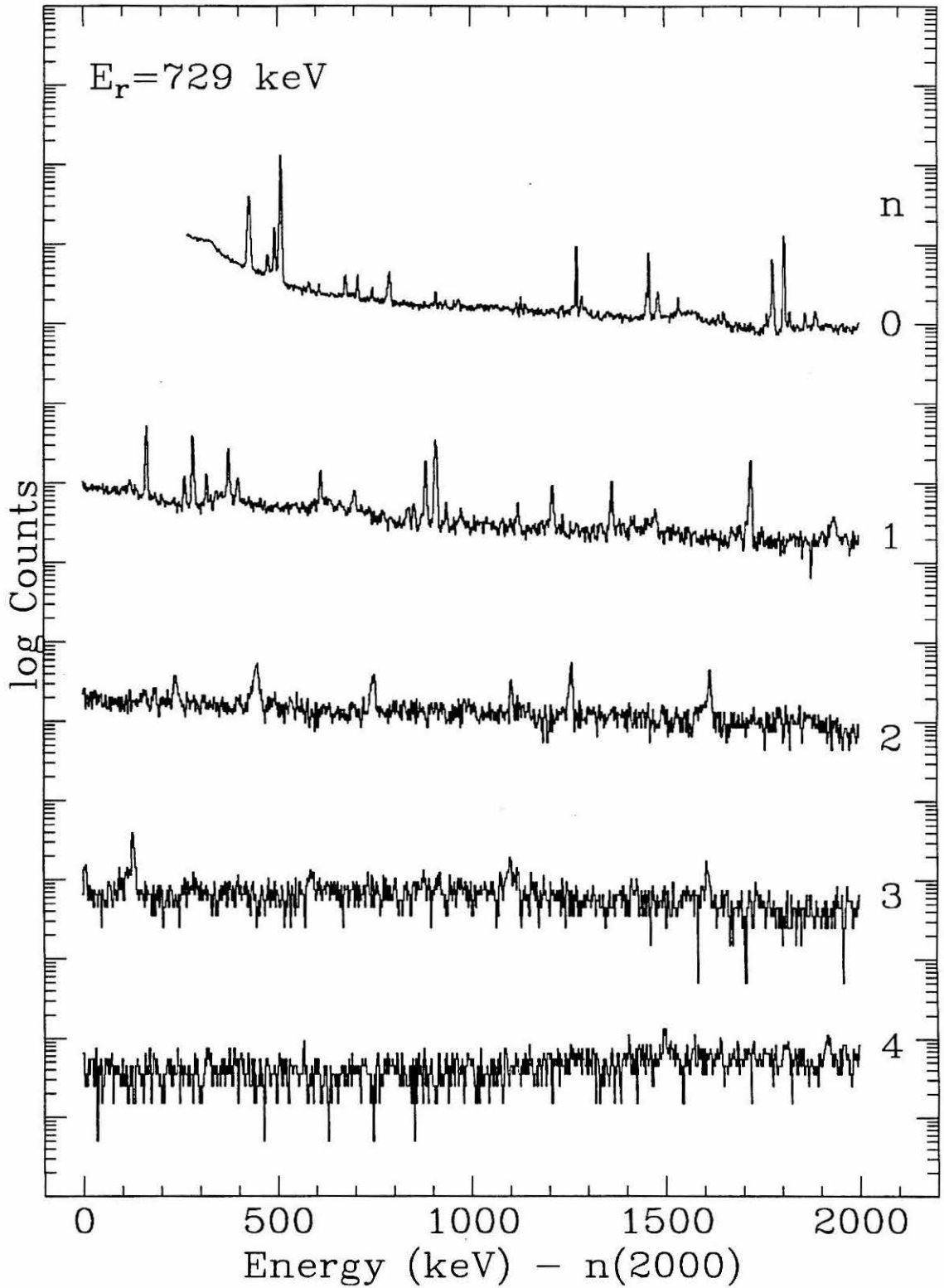
To determine the resonance strength one must observe at least one transition for each decay mode, and know the efficiency for observing it. Most of the decay modes observed are either directly to the ground state, or pass through the 2164- or 2910-keV levels. If there were no exceptions and none of these lines was obscured, then the branching ratios would only be needed to determine summing corrections to the efficiency, again assuming isotropic angular distributions. The uncertainties involved in determining the branching ratios are usually dominated by systematics, rather than statistics. The amount of "unknown" transitions provides a measure of how significant angular distribution effects might be. Due to the large detector solid angle, such effects will not be greater than 50%. Thus, for the weaker branches we assign a 50% uncertainty, while for the stronger ones we distribute a typical "unknown" strength of 20% to each. Since the uncertainties between various cascade modes will tend to cancel when determining the total number of events, the resonance strengths are given a 10% uncertainty from this source.

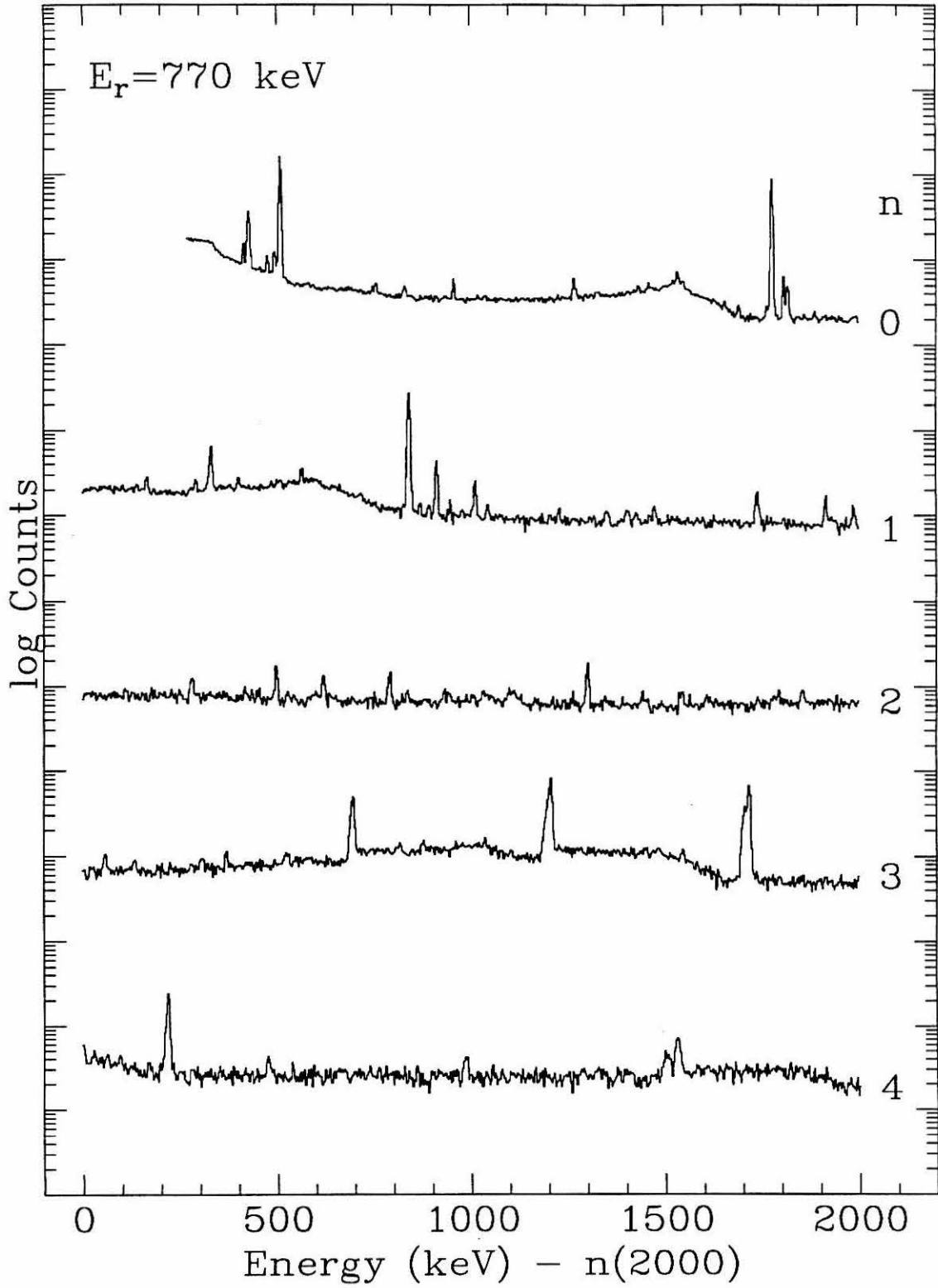
Figure A.1. Pulse-Height Spectra at Each Resonance.

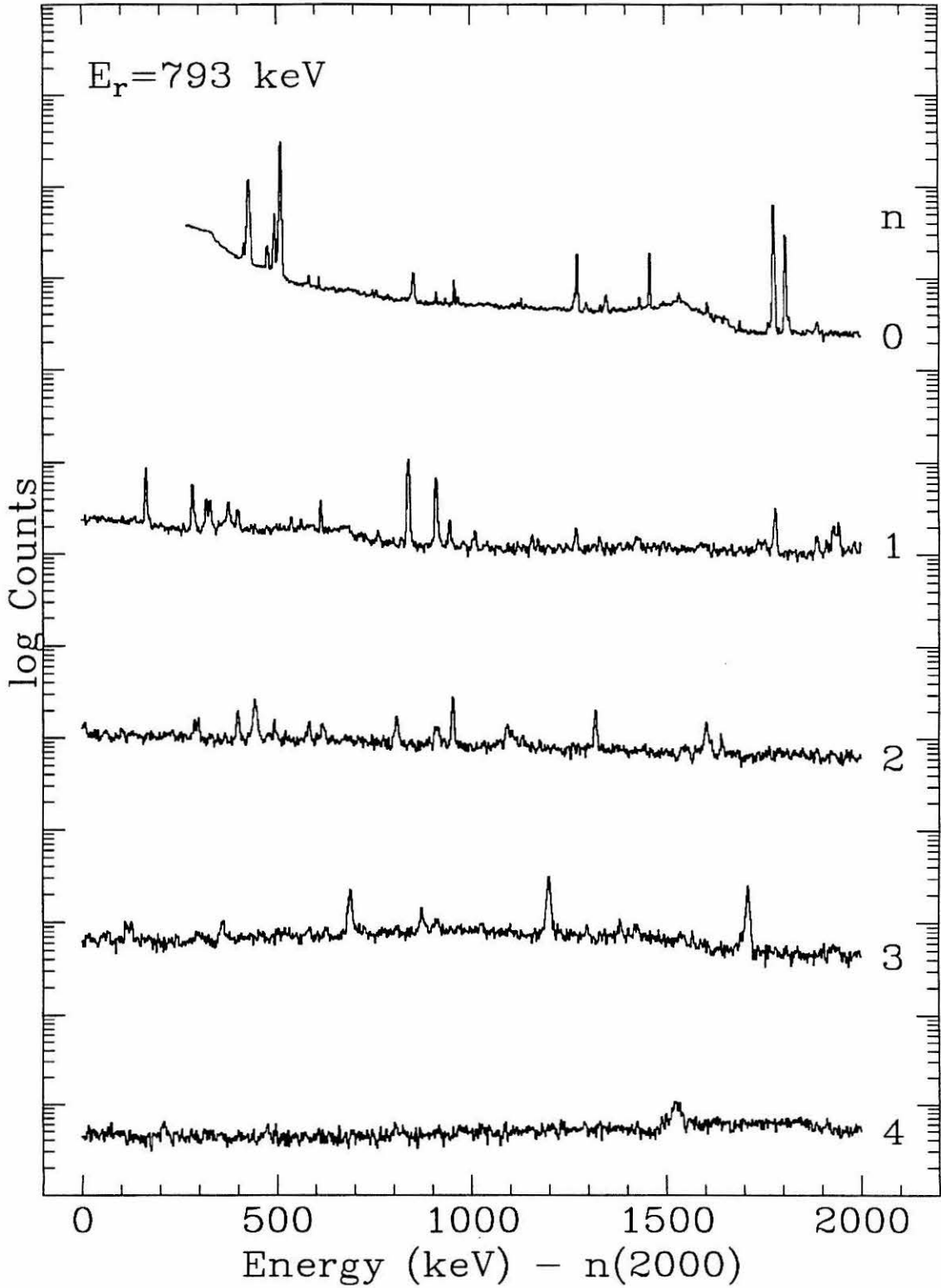


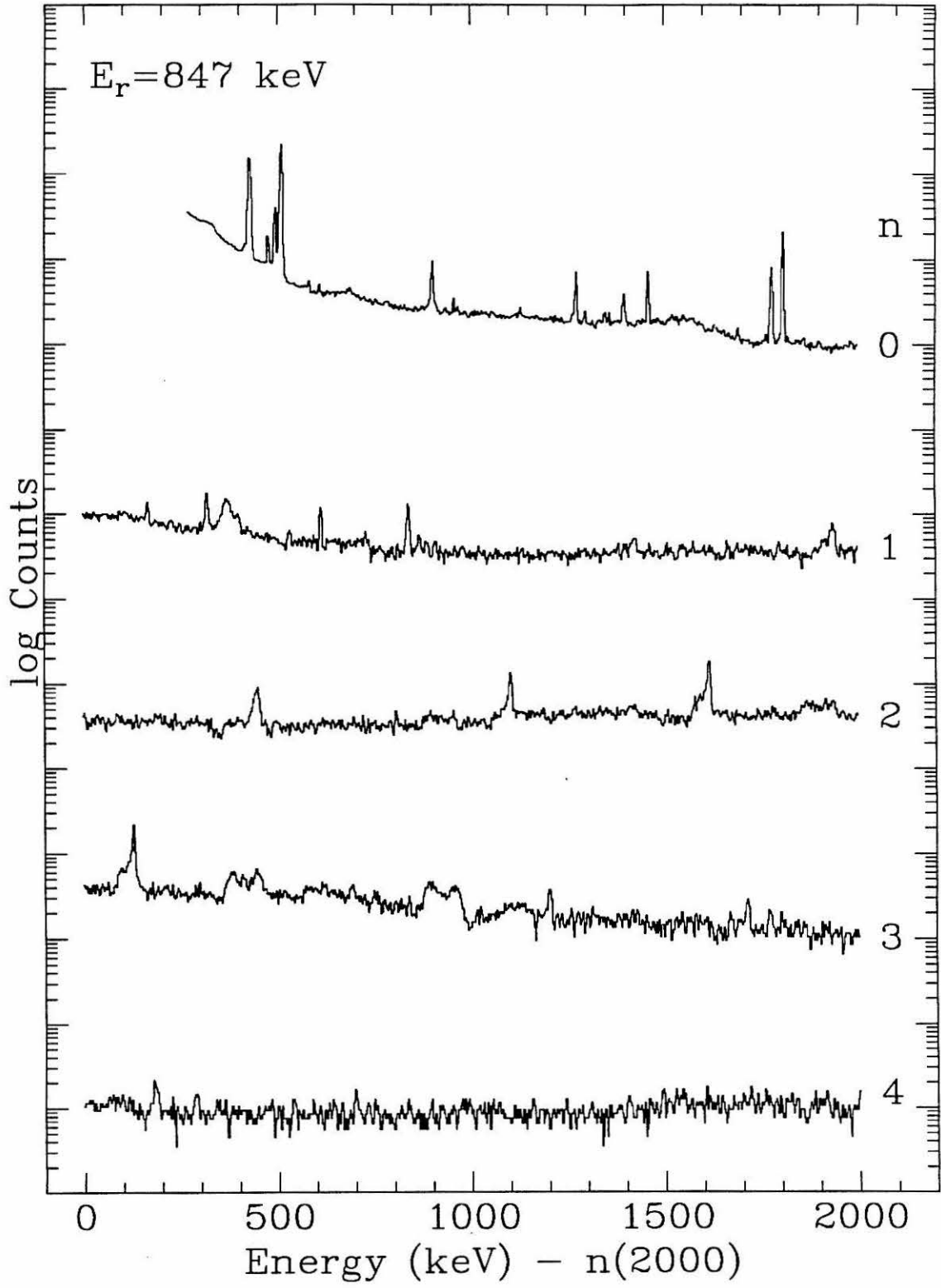


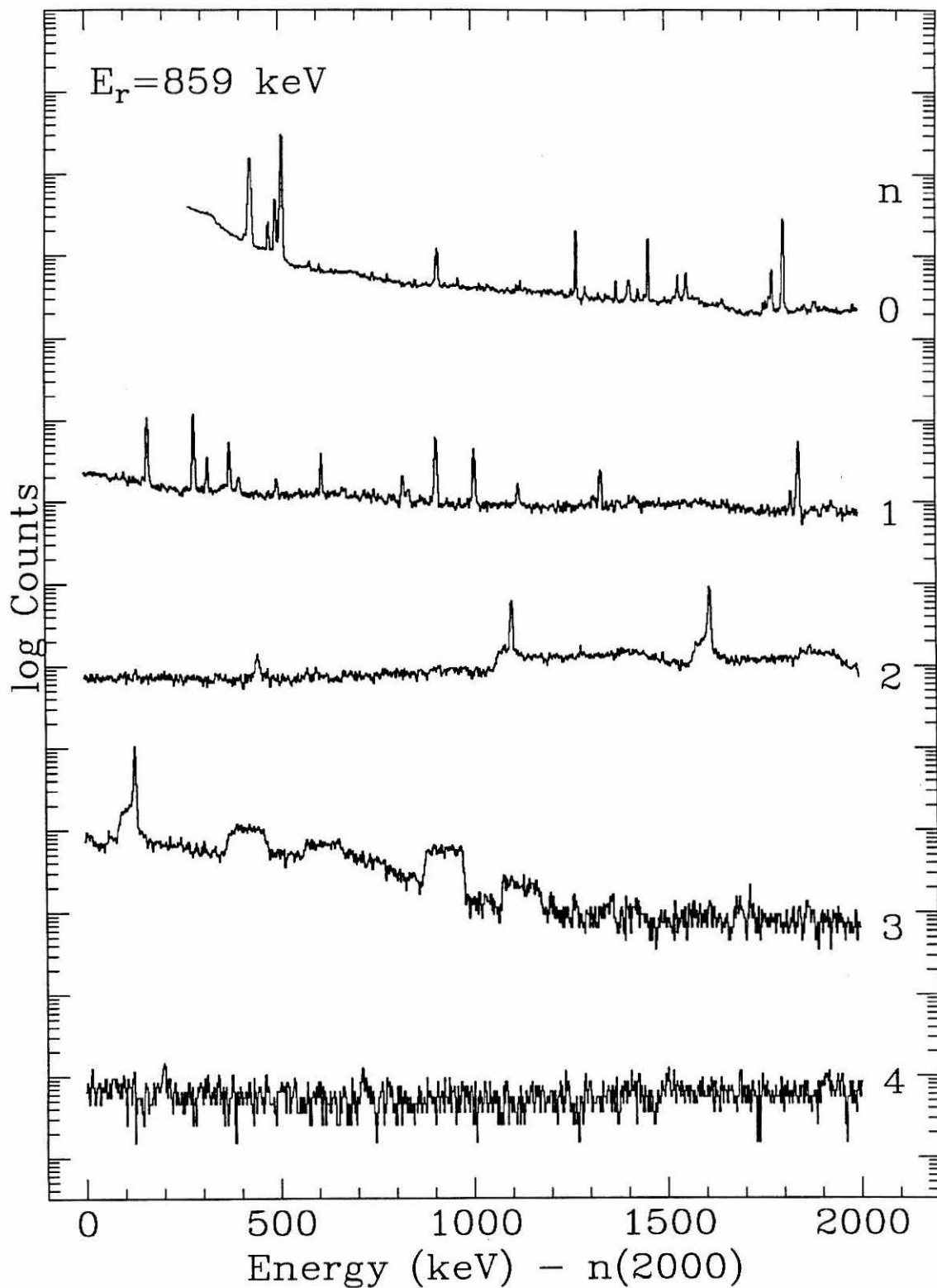


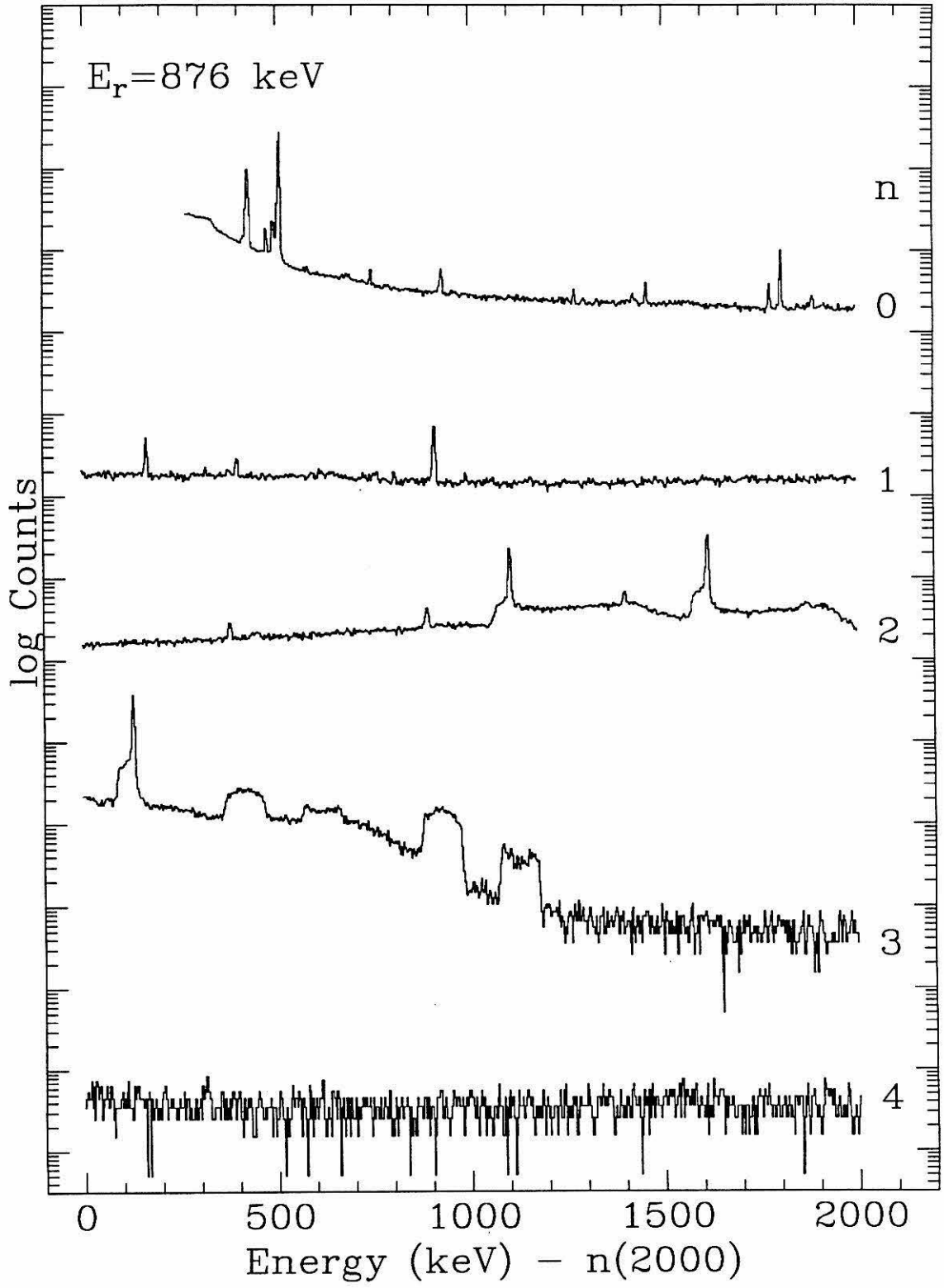


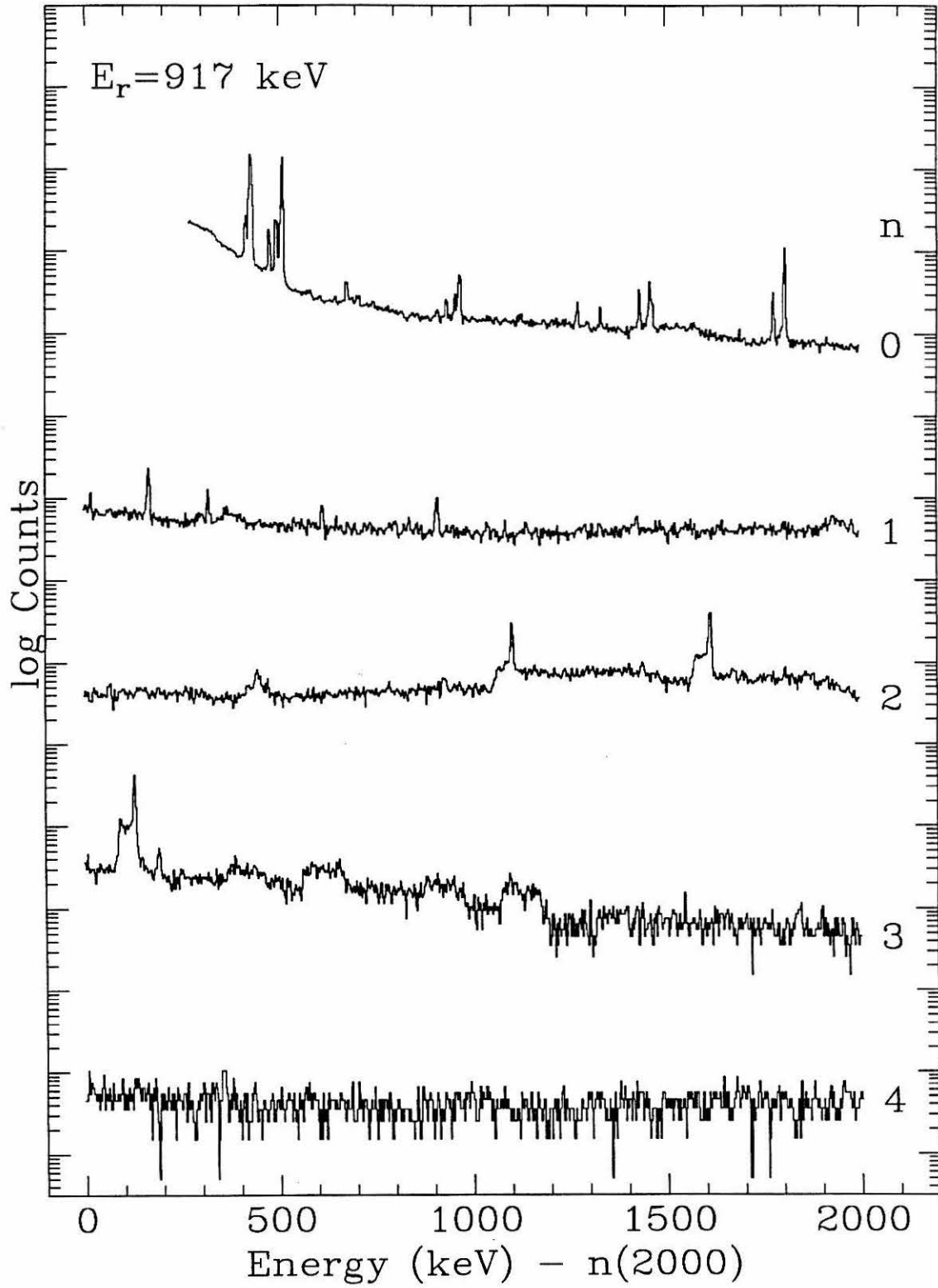


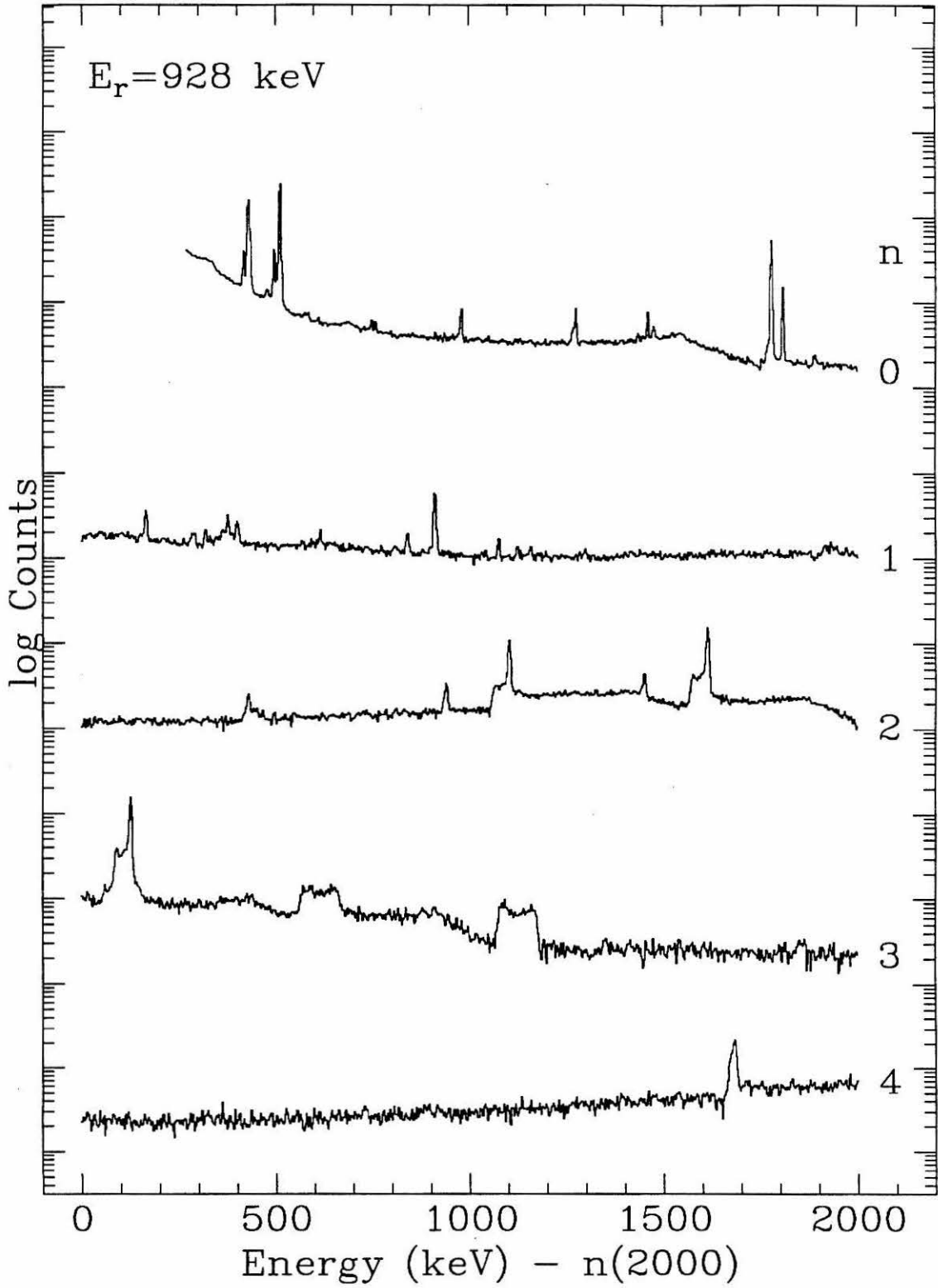












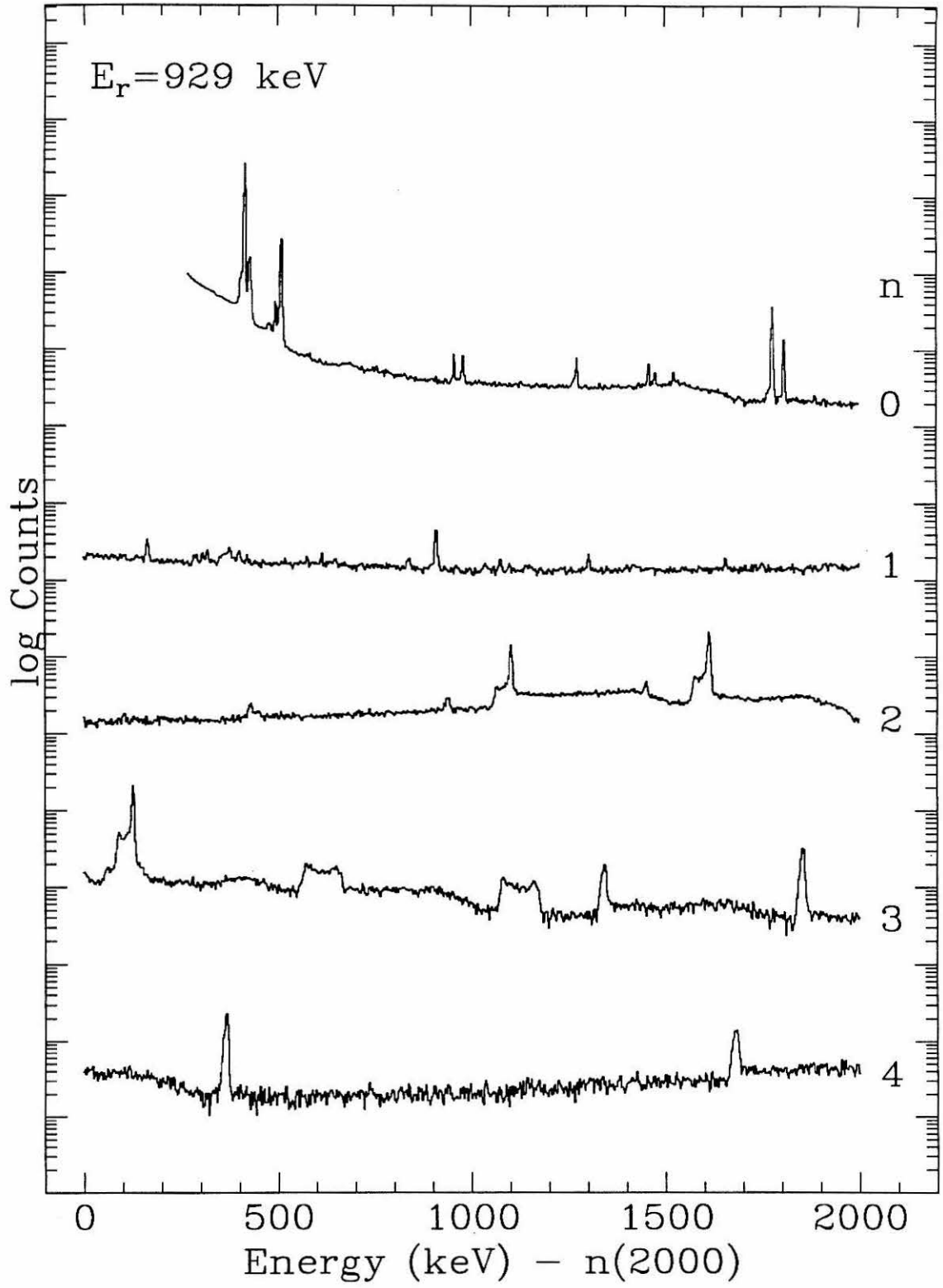
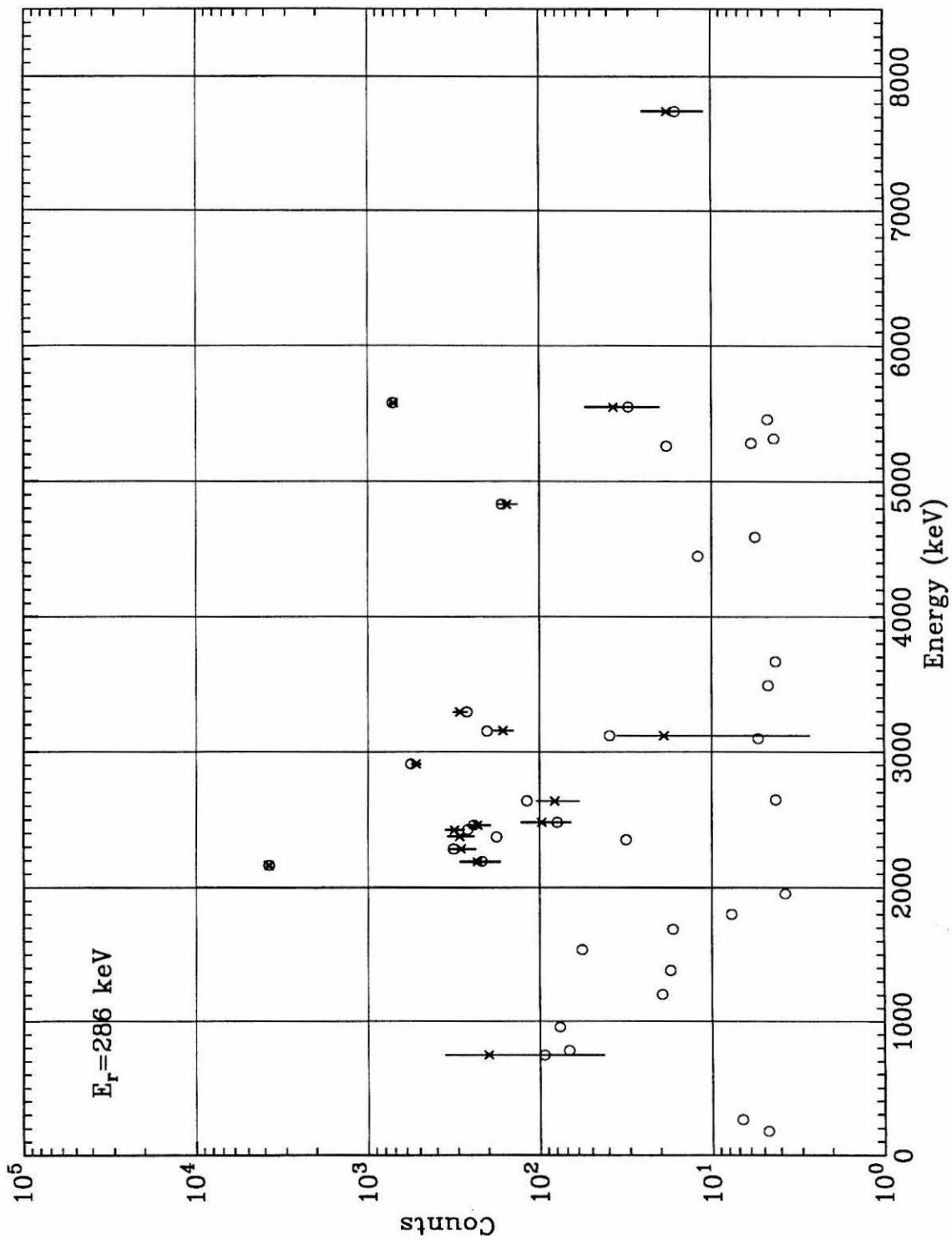
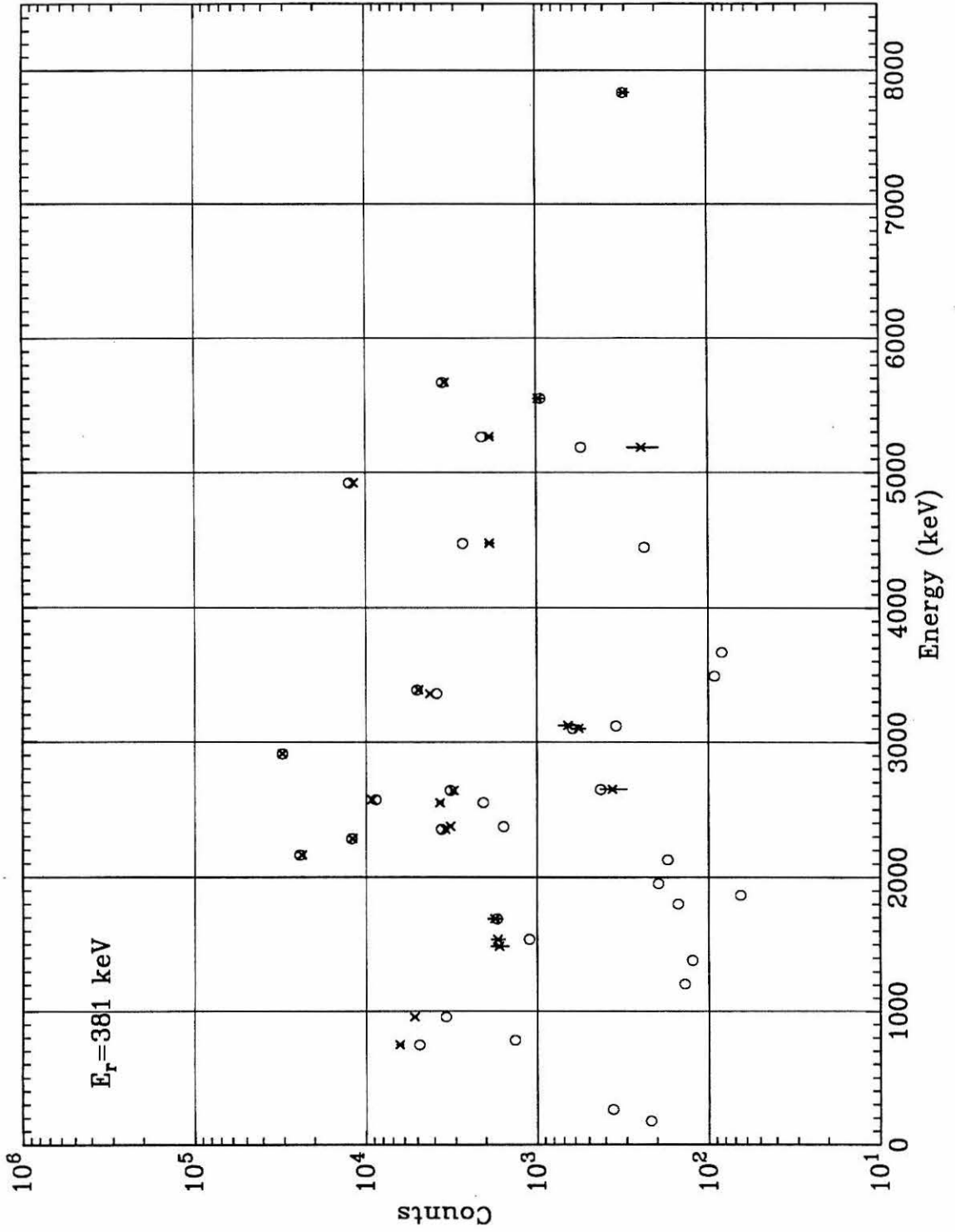
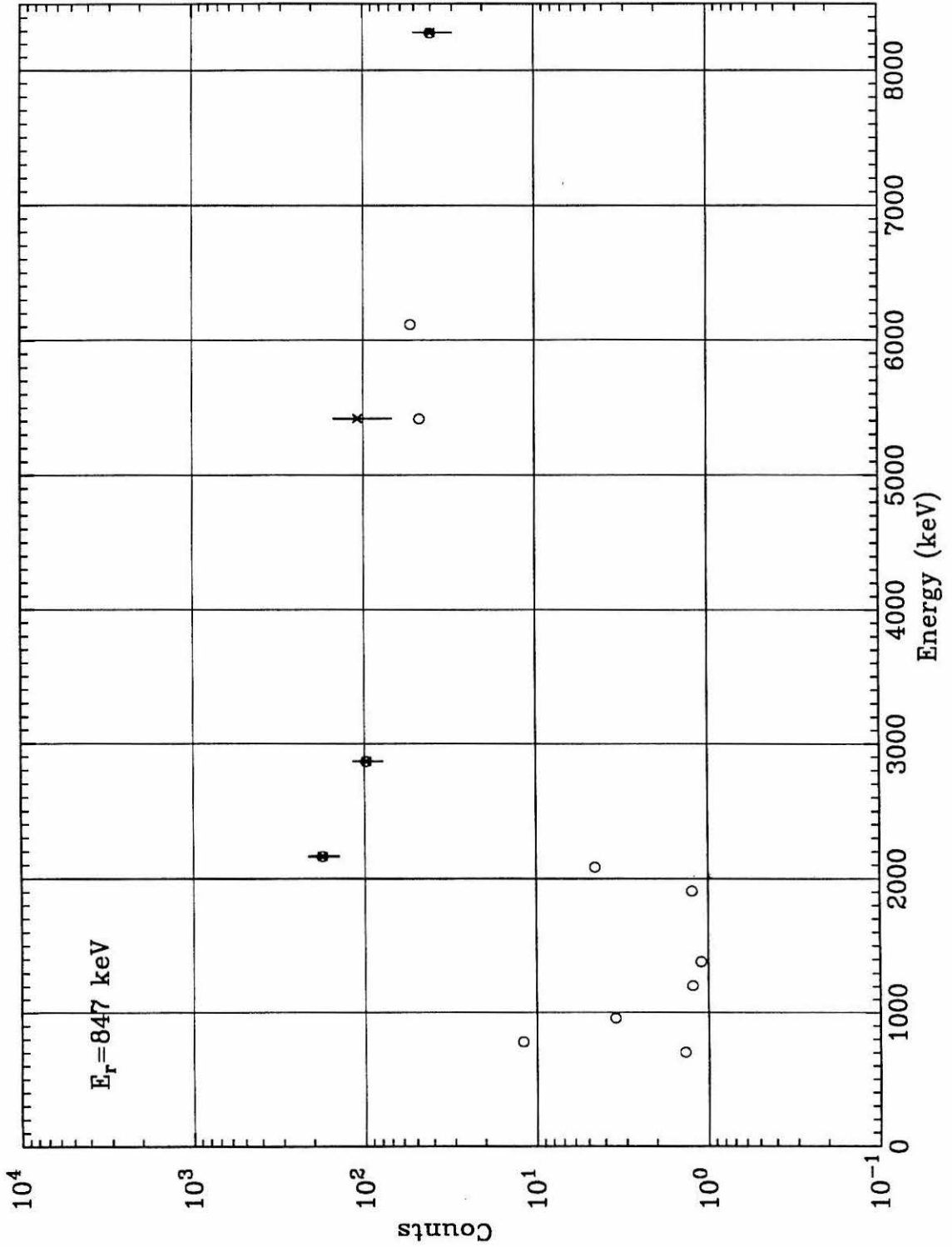


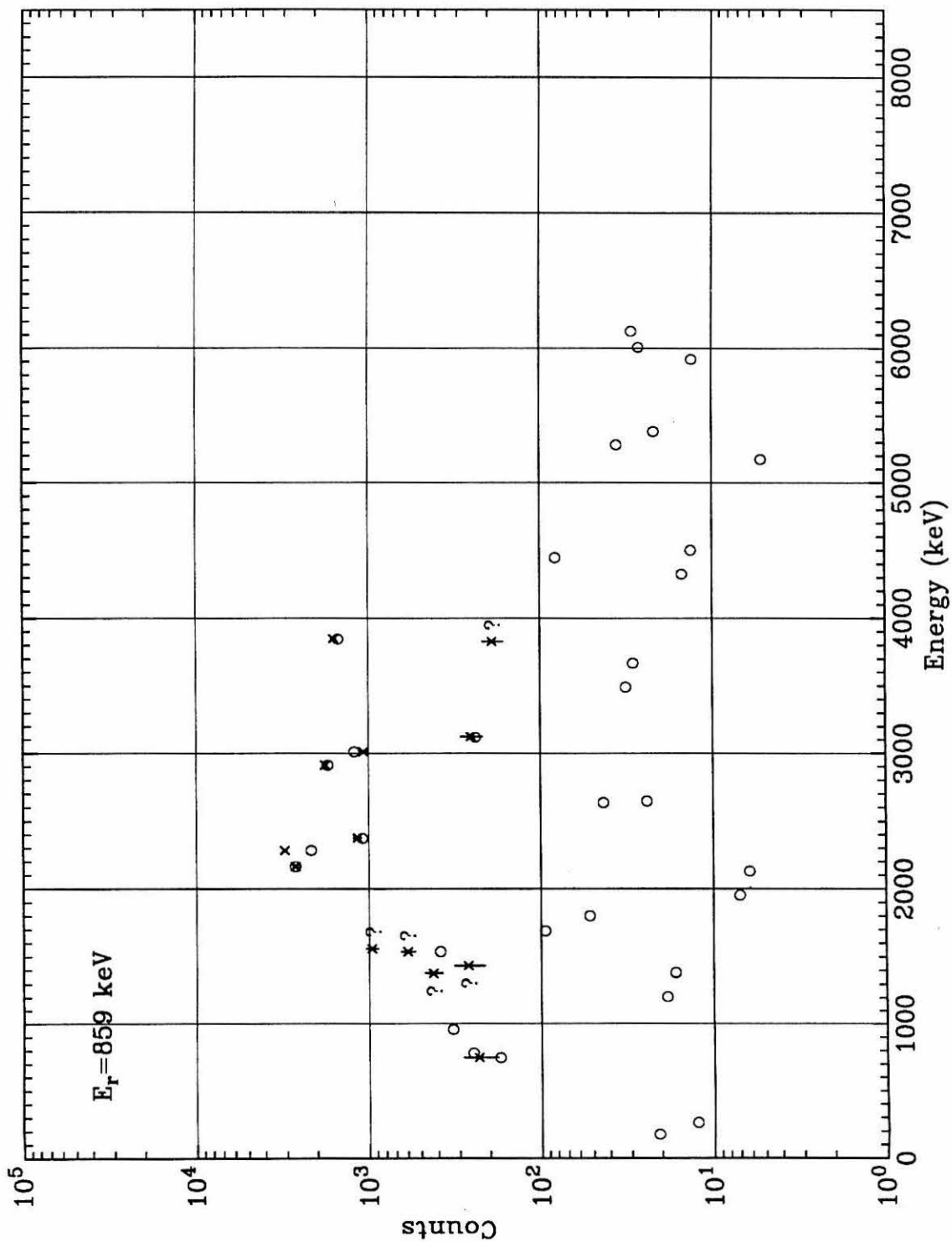
Figure A.2. γ -ray Yields at Each Resonance.

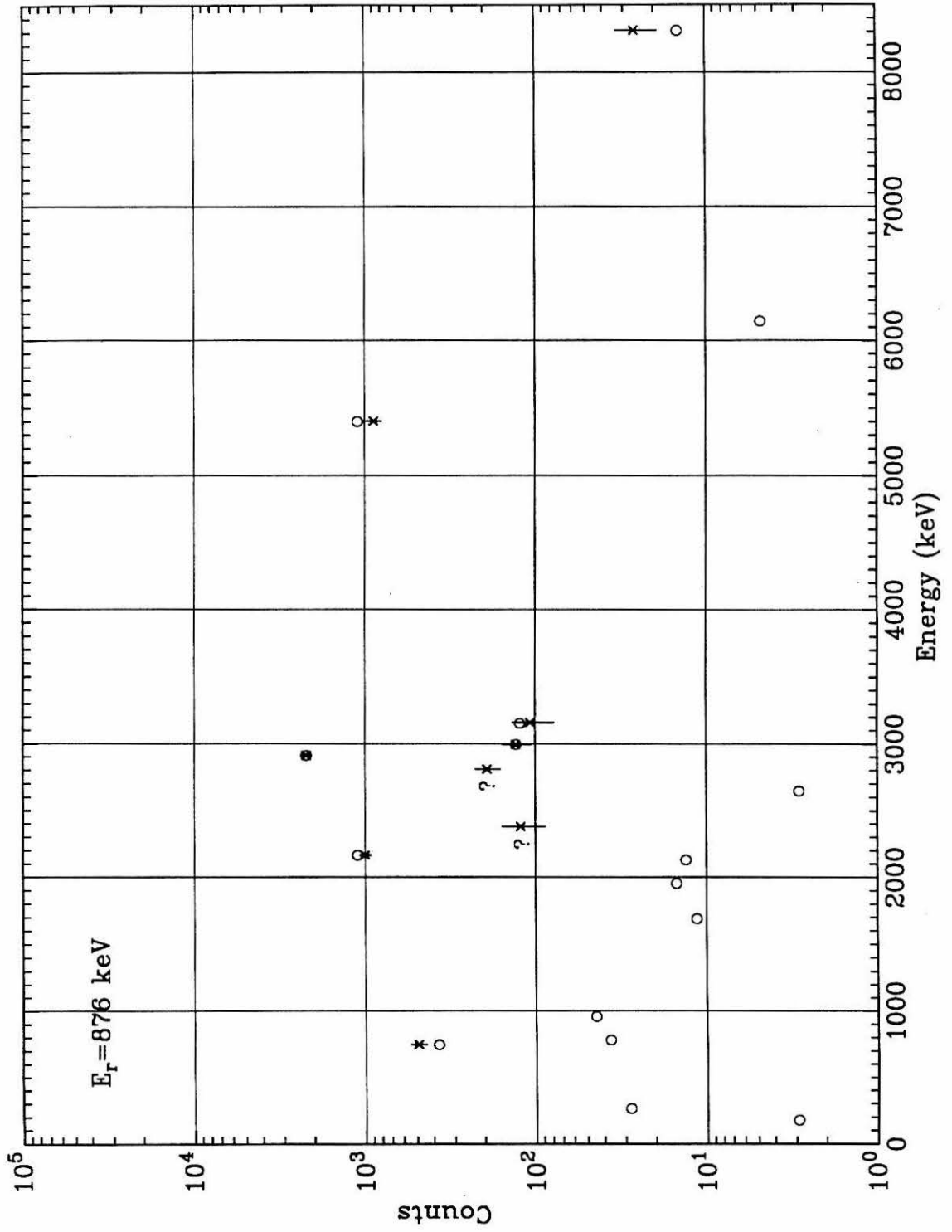
These figures compare the observed yields ("x") of each line with the expected yields ("o") based on the branching ratios given in Figure 3.8. ("Sum" peaks have been included, but not pair peaks.) In some cases where lines were not resolved it was impossible to determine the net yield due to $^{26}\text{Al}(p, \gamma)^{27}\text{Si}$. Where this occurred, the total yield is plotted and marked with a "B." Unidentified lines which resonated at the indicated proton energy are marked with a "?." Many predicted lines were too weak to be detected above the background and we have not indicated upper limits for them.

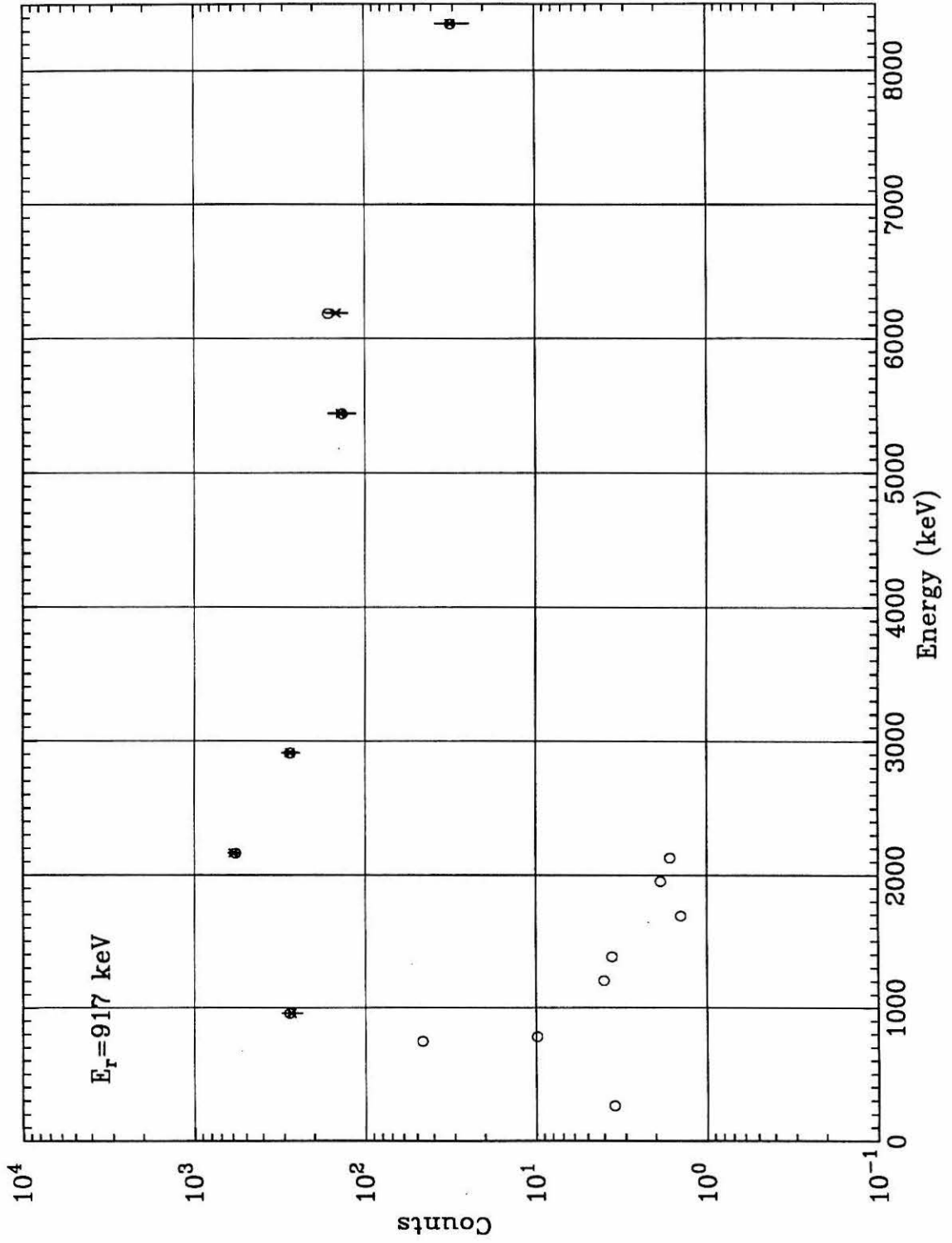


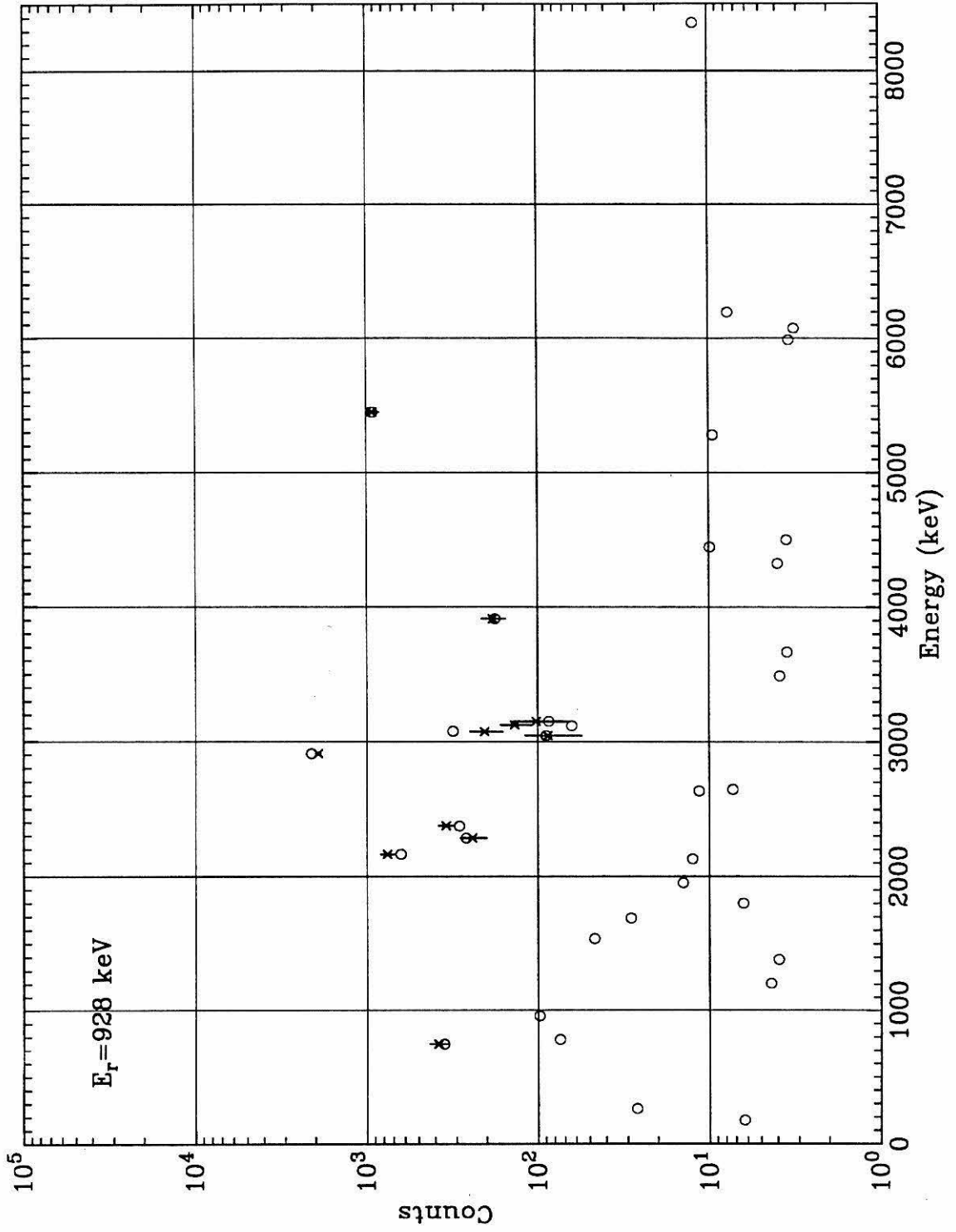












References

- ANT 77 A. Anttila, J. Keinonen, M. Hautala, and I. Forsblom, "Use of the $^{27}\text{Al}(p, \gamma)^{28}\text{Si}$, $E_p = 992\text{keV}$ Resonance as a Gamma-Ray Intensity Standard," *Nuc. Inst. and Meth.* **147** 501 (1977).
- ARN 77 W. D. Arnett, "Supernovae as Phenomena of High-Energy Astrophysics," *Ann. NY Acad. Sci.* **302** 90 (1977).
- ARN 78 W. D. Arnett and J. P. Wefel, " ^{26}Al Production from a Stellar Evolutionary Sequence," *Ap. J. Lett.* **224** L139 (1978).
- ARN 80 M. Arnould, H. Nørgaard, F. K. Thielemann, and W. Hillebrandt, "Synthesis of ^{26}Al in Explosive Hydrogen Burning," *Ap. J.* **237** 931 (1980).
- AUM 74 D. C. Aumann and G. Müllen, "Preparation of Targets of Ca, Ba, Fe, La, Pb, Tl, Bi, Th and U by Electrodeposition from Organic Solutions," *Nucl. Inst. and Meth.* **115** 75 (1974).
- BAL 87 P. von Ballmoos, R. Diehl, and V. Schönfelder, "Map of the Galactic Center Region in the 1.8 MeV ^{26}Al Gamma-Ray Line," *Ap. J.* **318** 654 (1987).
- BEN 77 W. Benenson, D. Mueller, E. Kashy, H. Nann, L. W. Robinson, "Mass of ^{27}P and ^{31}Cl ," *Phys. Rev.* **C15** 1187 (1977).
- BEN 82 G. E. Bentley, "Analysis of ^{26}Al for Stable Impurities," Los Alamos memorandum INC-3 (1982).
- BUC 83 L. Buchmann, "Die Stellaren Raten Der $^{26}\text{Al}(p, \gamma)^{27}\text{Si}$ -Reaktion," thesis, Münster, Germany (1983).
- BUC 84 L. Buchmann, M. Hilgemeier, A. Krauss, A. Redder, C. Rolfs, and H. P. Trautvetter, "The Abundance of ^{26}Al in the MgAl Cycle," *Nucl. Phys.* **A415** 93 (1984).
- BUC 84A L. Buchmann, H. Baumeister, and C. Rolfs, "The Fabrication of ^{26}Al Targets," *Nucl. Inst. and Meth.* **B4** 132 (1984).
- BUR 80 D. T. Burns, A. Townshend, and A. G. Catchpole, in *Inorganic Reaction Chemistry: Systematic Chemical Separation* John Wiley and Sons, New York, 178 (1980).
- CAM 77 A. G. W. Cameron and J. W. Truran, "The Supernova Trigger for Formation of the Solar System," *Icarus* **30** 447 (1977).
- CAU 88 G. R. Caughlan and W. A. Fowler, "Thermonuclear Reaction Rates V," *ADNDT* **40** 283 (1988).
- CHA 83B A. E. Champagne, A. J. Howard, and P. D. Parker, "Threshold States in ^{26}Al (II). Extraction of resonance strengths," *Nucl. Phys.* **A402** 179 (1983).
- CHA 86 A. E. Champagne et al., "Threshold States in ^{26}Al Revisited," *Nucl. Phys.* **A451** 498 (1986).
- CHA 86A A. E. Champagne et al., "Proton Threshold States in ^{28}Si ," *Nucl. Phys.* **A459** 239 (1986).

- CHA 87 A. E. Champagne et al., "Proton-Threshold States in ^{27}Si via the $^{28}\text{Si}(^3\text{He}, \alpha)^{27}\text{Si}$ Reaction," BAPS **32** 1579 (1987).
- CHA 88 A. E. Champagne et al., "Particle Decays in ^{28}Si : The destruction of ^{27}Al in red giants and novae," (submitted to Nuclear Physics)
- CLA 65 D. D. Clayton and W. L. Craddock, "Radioactivity in Supernova Remnants," Ap. J. **142** 189 (1965).
- CLA 69 D. D. Clayton, S. A. Colgate, and G. J. Fishman, "Gamma-Ray Lines from Young Supernova Remnants," Ap. J. **155** 75 (1969).
- CLA 73 D. D. Clayton, "Prospects for Nuclear-Gamma-Ray Astronomy," in *Gamma Ray Astrophysics*, ed. F. W. Stecker, and J. W. Trombka, NASA Special Publication **339** 263 (1973).
- CLA 74 D. D. Clayton and F. Hoyle, "Gamma-Ray Lines from Novae," Ap. J. **187** L101 (1974).
- CLA 75 D. D. Clayton, " ^{22}Na , Ne-E, Extinct Radioactive Anomalies and Unsupported ^{40}Ar ," Nature **257** 36 (1975).
- CLA 84 D. D. Clayton, " ^{26}Al in the Interstellar Medium," Ap. J. **280** 144 (1984).
- CLA 87 D. D. Clayton and M. D. Leising, " ^{26}Al in the Interstellar Medium," Physics Reports **144** 1 (1987).
- DEA 85 D. S. P. Dearborn and J. P. Blake, "On the Source of the ^{26}Al Observed in the Interstellar Medium," Ap. J. Lett. **288** L21 (1985).
- DEA 88 D. S. P. Dearborn, T. Lee, and G. J. Wasserburg, "The Origin of ^{26}Al ," in *XIX Lunar & Planetary Science Conf.* (1988).
- END 78 P. M. Endt and C. Van der Leun, "Energy Levels of A=21-44 Nuclei (VI)" Nucl. Phys. **A310** 1 (1978).
- END 87 P. M. Endt and C. Rolfs, "Astrophysical Aspects of the $^{25}\text{Mg}(p, \gamma)^{26}\text{Al}$ Reaction," Nucl. Phys. **A467** 261 (1987).
- FIC 75 C. E. Fichtel et al., "High-Energy Gamma-Ray Results from the Second Small Astronomy Satellite," Ap. J. **198** 163 (1975).
- FIS 60 R. A. Fish, G. G. Goles, and E. Anders, "The Record in the Meteorites. III. On the development of meteorites in asteroidal bodies," Ap. J. **132** 243 (1960).
- GOV 59 H. E. Gove, "Resonance Reactions, Experimental," in *Nuclear Reactions*, ed. P. M. Endt and M. Demeur, N. Holland Pub. Co., Amsterdam (1959) 259.
- HIG 87 J. C. Higdon and W. A. Fowler, "Gamma-Ray Constraints on ^{22}Na Yields in Nova Explosions," Ap. J. **317** 710 (1987).
- HIG 89 J. C. Higdon and W. A. Fowler, "Angular Distribution of 1.809-MeV Gamma Rays Generated in the Decay of ^{26}Al Produced by Galactic Novae," Ap. J. **339** (in press) (1989).
- HIL 82 W. Hillebrandt and F. -K. Thielemann, "Nucleosynthesis in Novae: A Source of Ne-E and ^{26}Al ?" Ap. J. **255** 617 (1982).

- HOF 86 R. Hoffman and S. E. Woosley, "Explosive Nucleosynthesis of Isotopes Important to Gamma-Line Astronomy," *BAAS* **18** 948 (1986).
- HUM 87 J. Humblet, W. A. Fowler, and B. A. Zimmerman, "Approximate Penetration Factors for Nuclear Reactions of Astrophysical Interest," *Astron. Astrophys.* **177** 317 (1987).
- JAM 86 D. N. Jamieson, "NUFIT: Interactive Graphics and Fitting," *unpublished computer program*
- JOH 72 W. N. Johnson, F. R. Harnden, and R. C. Haymes, "The Spectrum of Low-Energy Gamma Radiation from the Galactic-Center Region," *Ap. J.* **172** L1 (1972).
- KAV 60 R. W. Kavanagh, "Proton Capture in ${}^7\text{Be}$," *Nucl. Phys.* **15** 411 (1960).
- KOU 74 R. T. Kouzes, "A Measurement of the Mass of Helium-8" thesis, Princeton University (1974).
- KUN 69 P. D. Kunz, "DWUCK -distorted wave Born approximation (code)" University of Colorado (1969).
- LEE 77 T. Lee, D. A. Papanastassiou, and G. J. Wasserburg, "Aluminum 26 in the Early Universe: Fossil or Fuel?" *Ap. J.* **211** L107 (1977).
- LEE 79 T. Lee, W. A. Russell, and G. J. Wasserburg, "Calcium Isotopic Anomalies and the Lack of Aluminum-26 in an Unusual Allende Inclusion," *Ap. J.* **228** L93 (1979).
- LEI 85 M. D. Leising and D. D. Clayton, "Angular Distribution of Interstellar ${}^{26}\text{Al}$," *Ap. J.* **294** 591 (1985).
- MAA 78 J. W. Maas et al., "Investigation of ${}^{28}\text{Si}$ Levels with the (α, γ) and (p, γ) Reactions," *Nucl. Phys.* **A301** 213 (1978).
- MAC 60 M. H. MacFarlane and J. B. French, "Stripping Reactions and the Structure of Light and Intermediate Nuclei," *Rev. Mod. Ph.* **32** 567 (1960).
- MAC 87 C. J. MacCallum, A. F. Hutters, P. D. Stang, and M. Leventhal, "A New Constraint on the Galactic Plane ${}^{26}\text{Al}$ Distribution," *Ap. J.* **317** 877 (1987).
- MAH 82 W. A. Mahoney, J. C. Ling, A. S. Jacobson, and R. E. Lingenfelter, "Diffuse Galactic Gamma-Ray Line Emission from Nucleosynthetic ${}^{60}\text{Fe}$, ${}^{26}\text{Al}$, and ${}^{22}\text{Na}$: Preliminary Limits from *HEAO 3*," *Ap. J.* **262** 742 (1982).
- MAH 84 W. A. Mahoney, J. C. Ling, W. A. Wheaton, and A. S. Jacobson, "*HEAO 3* Discovery of ${}^{26}\text{Al}$ in the Interstellar Medium," *Ap. J.* **286** 578 (1984).
- MAH 85 W. A. Mahoney, J. C. Higdon, J. C. Ling, W. A. Wheaton, and A. S. Jacobson, *Proc. 19th Internat. Cosmic Ray Conf.* (La Jolla, CA) **1** 357 (1985).
- MAN 83 F. M. Mann, Hanford Engineering and Development Laboratory Report No. HEDL-TME 7883 (1983). (unpublished)

- MAY 82 H. A. Mayer-Hasselwander et al., "Large-Scale Distribution of Galactic Gamma Radiation Observed by COS-B," *Astr. Ap.* **105** 164 (1982).
- MER 56 P. W. Merrill, "Technetium in N-type Star 19 Piscium," *Publ. Astron. Soc. Pac.* **68** 70 (1956).
- NEL 85 W. R. Nelson, H. Hirayama, and D. O. Rogers, "The EGS4 Code System," SLAC-Report-265, December (1985).
- NOR 80 H. Nørgaard, "²⁶Al from Red Giants," *Ap. J.* **236** 895 (1980).
- PER 76 C. M. Perey and F. G. Perey, "Compilation of Phenomenological Optical-Model Parameters," *ADNDT* **17** 1 (1976).
- PRA 86 N. Prantzos and M. Cassé, "On the Production of ²⁶Al by Wolf-Rayet Stars: Galactic Yield and Gamma-Ray Line Emissivity," *Ap. J.* **307** 324 (1986).
- RAM 77 R. Ramaty and R. E. Lingenfelter, "²⁶Al: A Galactic Source of Gamma-Ray Line Emission," *Ap. J.* **213** L5 (1977).
- ROL 73 C. Rolfs, "Spectroscopic Factors from Radiative Capture Reactions," *Nucl. Phys.* **A217** 29 (1973).
- ROS 53 M. E. Rose, "The Analysis of Angular Correlation and Angular Distribution Data," *Phys. Rev.* **91** 610 (1953).
- SCH 86 P. Schmalbrock et al., "Proton Threshold States in ²⁷Si and Their Implications on Hydrogen Burning of ²⁶Al," *Nucl. Phys.* **A457** 182 (1986).
- SHA 85 G. H. Share et al., "Detection of Galactic ²⁶Al Gamma Radiation by the SMM Spectrometer," *Ap. J.* **292** L61 (1985).
- SKE 87 R. T. Skelton, R. W. Kavanagh, and D. G. Sargood, "²⁶Mg(p, n)²⁶Al and ²³Na(α, n)²⁶Al Reactions," *Phys. Rev.* **C35** 45 (1987).
- STA 86 S. Starrfield, W. M. Sparks, and J. W. Truran, "Hydrodynamic Models for Novae with Ejecta Rich in Oxygen, Neon, and Magnesium," *Ap. J.* **303** L5 (1986).
- THO 83 K. W. Thomas, "Production of Microcurie Amounts of Carrier-Free ²⁶Al," *Radiochimica Acta* **33** 213 (1983).
- TIM 88 R. Timmermann, H. W. Becker, C. Rolfs, U. Schröder, and H. P. Trautvetter, "Search for Low-Energy Resonances in ²⁷Al(p, α)²⁴Mg," *Nucl. Phys.* **A477** 105 (1988).
- TRA 86 H. P. Trautvetter et al., "Destruction of ²⁶Al in Explosive Nucleosynthesis," *Z. Phys. A - Atomic Nuclei* **323** 1 (1986).
- TRU 78 J. W. Truran and A. G. W. Cameron, "²⁶Al Production in Explosive Carbon Burning," *Ap. J.* **219** 226 (1978).
- URE 55 H. C. Urey, "The Cosmic Abundances of K, U, and Th and the Heat Balances of the Earth, the Moon, and Mars," *Proc. Nat. Acad. Sci.* **41** 127 (1955).

- WAL 81 R. K. Wallace and S. E. Woosley, "Explosive Hydrogen Burning," *Ap. J. Supp.* **45** 389 (1981).
- WAN 86 T. F. Wang, "Proton Threshold States in ^{14}O and ^{27}Si ," thesis, Yale University (1986).
- WAN 89 T. F. Wang et al., "Proton Threshold States in ^{27}Si and the Destruction of ^{26}Al at Low Stellar Temperatures," *submitted for publication*
- WAP 85 A. H. Wapstra and G. Audi, "The 1983 Atomic Mass Evaluation," *Nucl. Phys.* **A432** 1 (1985).
- WAR 80 R. A. Ward and W. A. Fowler, "Thermalization of Long-Lived Nuclear Isomeric States Under Stellar Conditions," *Ap. J.* **238** 266 (1980).
- WIE 86 M. Wiescher and K. Langanke, "The Proton Capture Reactions on ^{21}Na and ^{22}Na under Hydrogen Burning Conditions," *Z. Phys.* **A325** 309 (1986).
- WIE 86A M. Wiescher, J. Görres, F. K. Thielemann, H. Ritter, "Explosive Hydrogen Burning in Novae," *Astr. and Astrophysics* **160** 56 (1986).
- WOH 84 C. G. Wohl et al., "Review of Particle Properties," *Rev. of Mod. Phy.* **56** S1 (1984).
- WOO 78 S. E. Woosley, W. A. Fowler, J. A. Holmes, and B. A. Zimmerman, "Semiempirical Thermonuclear Reaction-Rate Data for Intermediate-Mass Nuclei," *ADNDT* **22** 371 (1978).
- WOO 80 S. E. Woosley and T. A. Weaver, "Explosive Neon Burning and ^{26}Al Gamma-Ray Astronomy," *Ap. J.* **238** 1017 (1980).